

*Advanced Wireless Integrated Navy Network - **AWINN***

3rd Quarterly Report

Virginia Tech

July 1, 2005 – September 30, 2005

DISTRIBUTION STATEMENT A
Approved for Public Release
Distribution Unlimited

REPORT DOCUMENTATION PAGE

Form Approved
OMB No. 0704-0188

The public reporting burden for this collection of information is estimated to average 1 hour per response, including the time for reviewing instructions, searching existing data sources, gathering and maintaining the data needed, and completing and reviewing the collection of information. Send comments regarding this burden estimate or any other aspect of this collection of information, including suggestions for reducing the burden, to Department of Defense, Washington Headquarters Services, Directorate for Information Operations and Reports (0704-0188), 1215 Jefferson Davis Highway, Suite 1204, Arlington, VA 22202-4302. Respondents should be aware that notwithstanding any other provision of law, no person shall be subject to any penalty for failing to comply with a collection of information if it does not display a currently valid OMB control number.

PLEASE DO NOT RETURN YOUR FORM TO THE ABOVE ADDRESS.


1. REPORT DATE (DD-MM-YYYY) September 30, 2005		2. REPORT TYPE Quarterly Report		3. DATES COVERED (From - To) 1 Jul. to 30 Sep. 2005	
4. TITLE AND SUBTITLE Advanced Wireless Integrated Navy Network (AWINN)				5a. CONTRACT NUMBER N00014-05-1-0179	
				5b. GRANT NUMBER N00014-05-1-0179	
				5c. PROGRAM ELEMENT NUMBER	
6. AUTHOR(S) Warren Stutzman and Rick Habayeb				5d. PROJECT NUMBER	
				5e. TASK NUMBER	
				5f. WORK UNIT NUMBER	
7. PERFORMING ORGANIZATION NAME(S) AND ADDRESS(ES) Virginia Polytechnic Institute and State University Electrical and Computer Engineering Department 302 Whittemore Hall (0111) Blacksburg, VA 24061				8. PERFORMING ORGANIZATION REPORT NUMBER 3	
9. SPONSORING/MONITORING AGENCY NAME(S) AND ADDRESS(ES) Office of Naval Research ONR 313 875 N. Randolph St. Arlington, VA 22203-1995				10. SPONSOR/MONITOR'S ACRONYM(S)	
				11. SPONSOR/MONITOR'S REPORT NUMBER(S)	
12. DISTRIBUTION/AVAILABILITY STATEMENT Approved for public release; distribution unlimited.					
13. SUPPLEMENTARY NOTES The views, opinions and/or findings contained in this report are those of the author(s) and should not be constructed as an official Department of the Navy position, policy or decision, unless so designated by other documentation.					
14. ABSTRACT Quarterly progress report No. 3 on AWINN hardware and software configurations of smart, wideband, multi-function antennas, secure configurable platform, close-in command and control for Sea Basing visualization of wireless technologies, Ad Hoc networks, network protocols, real-time resource allocation, Ultra Wideband (UWB) communications network and ranging sensors, cross layer optimization and network interoperability.					
15. SUBJECT TERMS					
16. SECURITY CLASSIFICATION OF:			17. LIMITATION OF ABSTRACT UL	18. NUMBER OF PAGES	19a. NAME OF RESPONSIBLE PERSON Rick Habayeb 
a. REPORT U	b. ABSTRACT U	c. THIS PAGE U			19b. TELEPHONE NUMBER (Include area code) 540-231-4353

TABLE OF CONTENTS

Executive Summary	1
1. TASK 1 Advanced Wireless Technologies	2
1.1 Task 1.1 Advanced Antennas.....	2
1.2 Task 1.2 Advanced Software Radio	23
1.3 Task 1.3 Collaborative and Secure Wireless Communications.....	53
2. TASK 2 Secure and Robust Networks	64
2.1 Task 2.1 Ad Hoc Networks	64
2.2 Task 2.2 Real-Time Resource Management, Communications, and Middleware	71
2.3 Task 2.3 Network Interoperability and Quality of Service	76
2.4 Task 2.4 Cross-Layer Optimization	77
3. TASK 3 Visualization of Wireless Technology and Ad Hoc Networks	101
3.1 Overview	101
3.2 Task Activities for the period.....	101
3.3 Importance/Relevance	104
3.4 Productivity	104
4. TASK 4 Testing and Demonstrations.....	106
4.1 TIP#1 Distributed MIMO UWB sensor networks incorporating software radio	106
4.2 TIP#2 Close-in UWB wireless application to Sea Basing	117
4.3 TIP #3: Secure Ad Hoc Networks.....	121
4.4 TIP #4: Integration of Close-in UWB wireless with ESM crane for Sea Basing applications.....	124
5. FINANCIAL REPORT.....	126

Executive Summary

This third quarterly report provides summaries on the activities and productivity of the AWINN team at Virginia Tech. The report covers the following thrust areas:

- Advanced Wireless Technology
- Secure and Robust Networks
- Visualization of Wireless Technology and Ad Hoc Networks
- Technology Integration Projects

The Advanced Antennas Group has completed a comprehensive investigation of Wideband and Ultra Wideband (UWB) antennas for the AWINN projects. The investigation concluded that Tapered Slot / Vivaldi, Impulse Radiating Antennas (IRA), and TEM Horn antennas are good candidates for Wideband and UWB applications. During this reporting period the SDR team focused on the development of prototype transceivers and algorithms to support UWB, MIMO communications, position location and ranging. The SDR algorithms development group investigated a narrow band interference (NBI) mitigation approach for the UWB signals using multiple receive antennas. The result shows that doubling the number of antennas will give a 3dB performance improvement under Rayleigh fading condition. Tests conducted by the group confirm that time-interleaved sampling of UWB pulses using off-the-shelf components is feasible. The Collaborative and Secure Communications team is developing protocols for inter- and intra-communications between network nodes. They are investigating methods for improving the communication link performance between a mobile base station and distributed mobile sensor network. The effort of the Cross-Layer Optimization group is focused on cross-layer design of UWB for position location networks PoLoNet and collaborative radio networks. The Networking Group is investigating various protocols for QoS, security, mobile routing, and cross-layer optimization. The Real-Time team is concentrating on the standard for the Distributed Real-Time Specification of Java (DRTSJ) and the time utility function. The Visualization of Wireless Technology team is completing an investigation of UWB contact-less sensors for close-in operations. The Technology Integration Projects (TIP) are examining various approaches to integrate and demonstrate the AWINN technologies.

1. TASK 1 Advanced Wireless Technologies

1.1 Task 1.1 Advanced Antennas

1.1.1 Overview

Task Goal: This task investigates new antenna technologies that are applicable to Navy missions and provide hardware for AWINN integration projects.

Organization: This task is managed by Director of Virginia Tech Antenna Group (VTAG) using the following personnel:

Bill Davis, Director
Warren Stutzman, Faculty
Randall Nealy, Engineer
Taeyoung Yang, GRA
Scott Bates, GRA
John Kim, GRA

Summary: Progress continued this quarter in the development of small antennas for other AWINN tasks. Identification of specific requirements for antennas to support the AWINN demonstrations is now complete.

1.1.2 Task Activities for the Period

Task objective: Investigate new antenna technologies applicable to Navy missions and provide hardware for AWINN integration projects.

Accomplishments during reporting period: Additional progress on compact planar UWB antennas and determination of the requirements for antennas in other AWINN tasks.

Links to other tasks: Tasks 1.2, 1.3, 3, and 4

Subtask 1.1a Investigation of compact antennas for handheld and mobile terminals

Task objective: Design compact planar UWB antennas for various applications and systems.

Accomplishments during reporting period:

No specific activity this quarter. See related subtasks.

Links to other tasks: This task supports Tasks 1.2 and task 4

Schedule: This continues through the December 2005.

Personnel: Taeyoung Yang, GRA

Subtask 1.1b Antenna Characterization – transient & wideband

Task objective: Provide antenna characterization methods in both frequency and time domains.

Accomplishments during reporting period:

Normal-Mode, Logarithmic, Tape Helix

Many ultra-wideband antennas have square planar shapes. However, for some applications, the width of antenna is more critical than the height. Thus, the ultra-wideband antenna with a

cylindrical structure would be useful. In the literature, a couple of antenna structures were recently investigated. The bi-arm rolled monopole [1.1b-1] showed better performance, comparing with rectangular fat monopole. However, this structure has performance similar to the discone antenna and still requires similar dimensions. The monopole with twist [1.1b] has a ratio of height –to-diameter of about 2, but requires wrapping with try-and-error to match the impedance.

During this quarter, efforts were focused on examining a new class of antenna, the normal-mode logarithmic tape helix antenna, which has an equal-angular width and provides ultra-wideband characteristics.

Antenna Structure

The antenna structure is shown in Fig. 1.1-1 and the parameters are listed in Table 1.1-1. The pertinent design equations are:

$$z_{L_1} = \alpha r_0 e^{b\phi} \quad (1.1b-1)$$

$$z_{L_2} = \alpha r_0 e^{b(\phi-\delta)} \quad (1.1b-2)$$

where α is linear scaling factor, r_0 is radius, b is wrapping rate, and δ is angular width.

Table 1.1-1 Summary of the test antenna geometrical parameter values

	A	r_0	B	δ	H_{ANT}	H_{CUT}	H_{FEED}
Tape Helix	2.7475	150 mil	0.2	0.291 radian	965 mil	100 mil	25 mil
Fat Monopole	×	150 mil	×	×	940 mil	×	50 mil

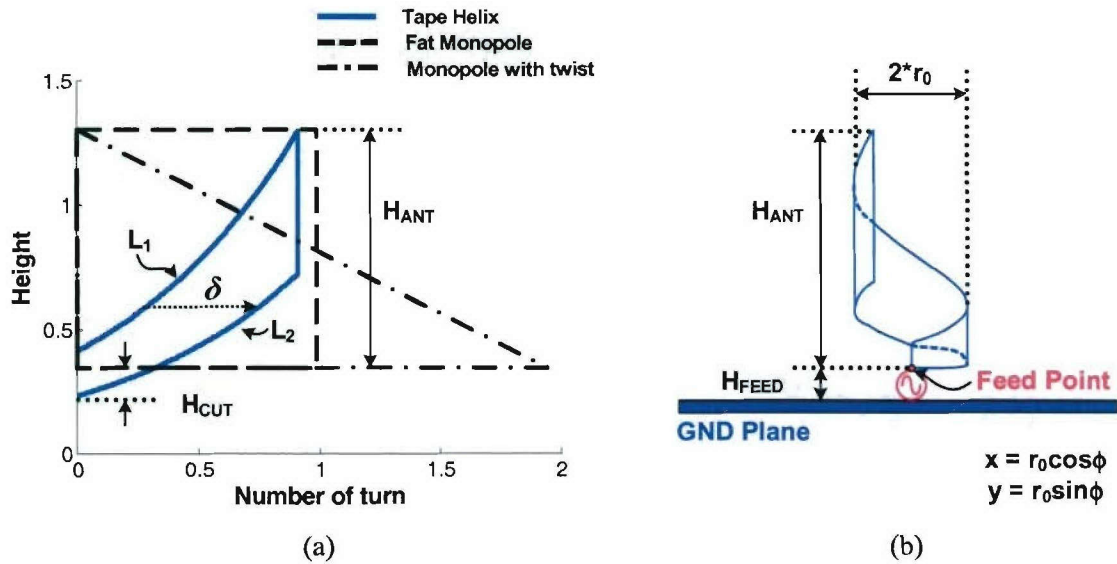


Figure 1.1-1 Geometry of the tape helix and the associated parameters

Results

The test results for the tape helix antenna and comparison fat monopole of Fig. 1.1-2, in both the time and frequency domains are shown in Fig. 1.1-3 and 4.

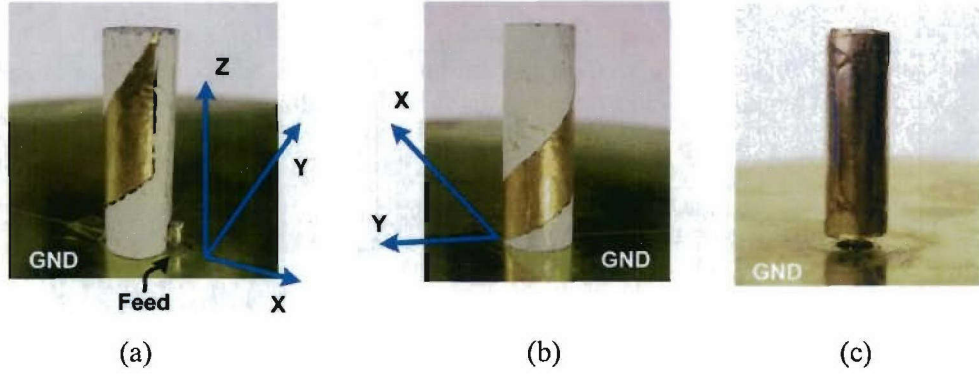


Figure 1.1-2 Photo of tape helix and fat monopole test articles.

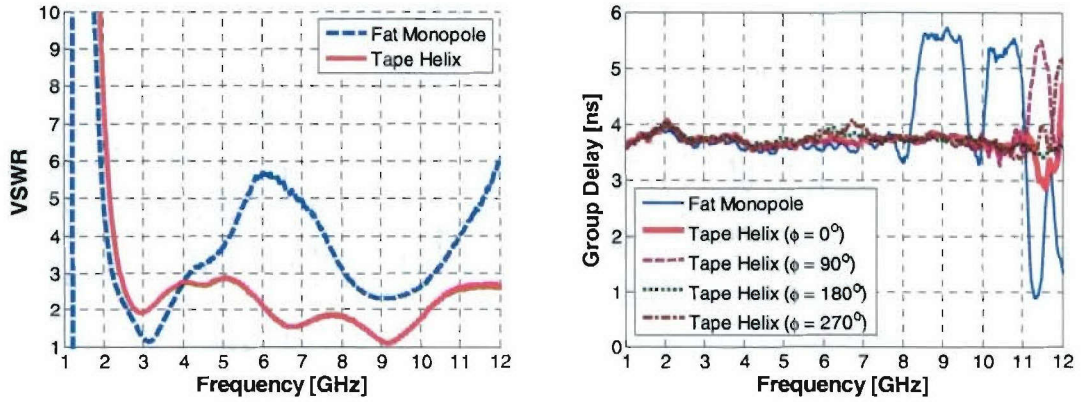


Figure 1.1-3 Comparison of return loss and group delay for the fat monopole and the tape helix antennas.

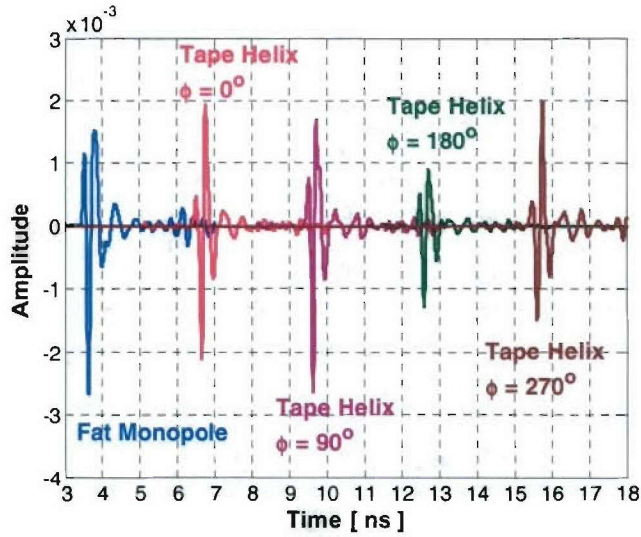


Figure 1.1-4 Comparison of measured transient responses for the tape helix and fat monopole. (Note: A time shift of 3 ns is added to each transient response in order to distinguish each pulse shape easily).

The measured radiation patterns for the tape helix antenna are plotted in Figs. 1.1-5, 6, and 7. The realized gain and axial ratio computed from simulations are plotted in Fig. 1.1-8. Frequency dependence of

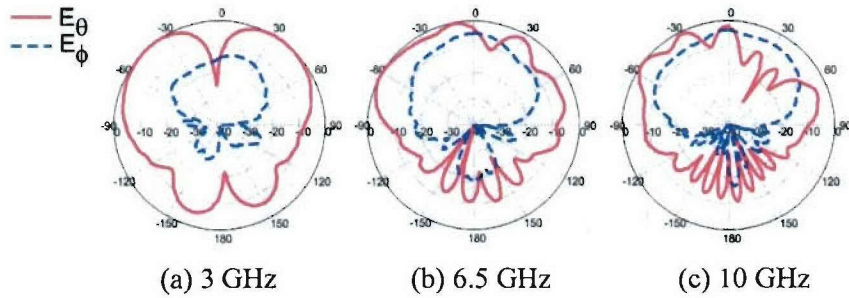


Figure 1.1-5 Measured elevation radiation patterns for the tape helix antenna at Phi = 0 degree

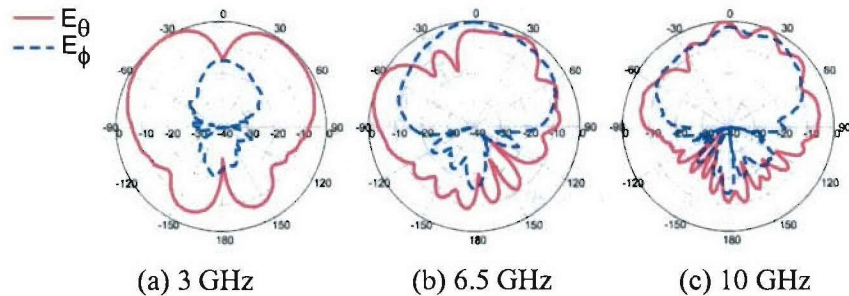


Figure 1.1-6 Measured elevation radiation patterns for the tape helix antenna Phi = 90 degree

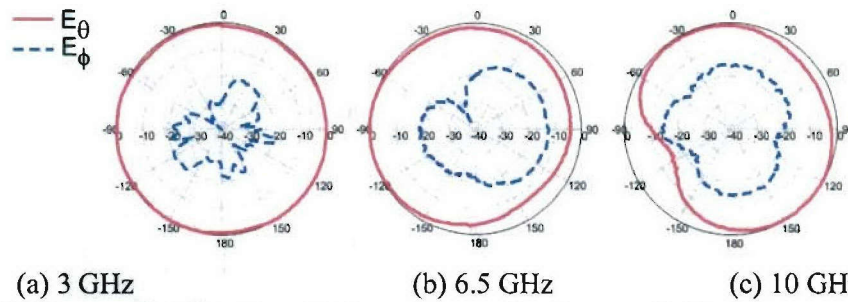


Figure 1.1-7 Measured azimuth radiation patterns for the tape helix antenna at Theta = 90 degree

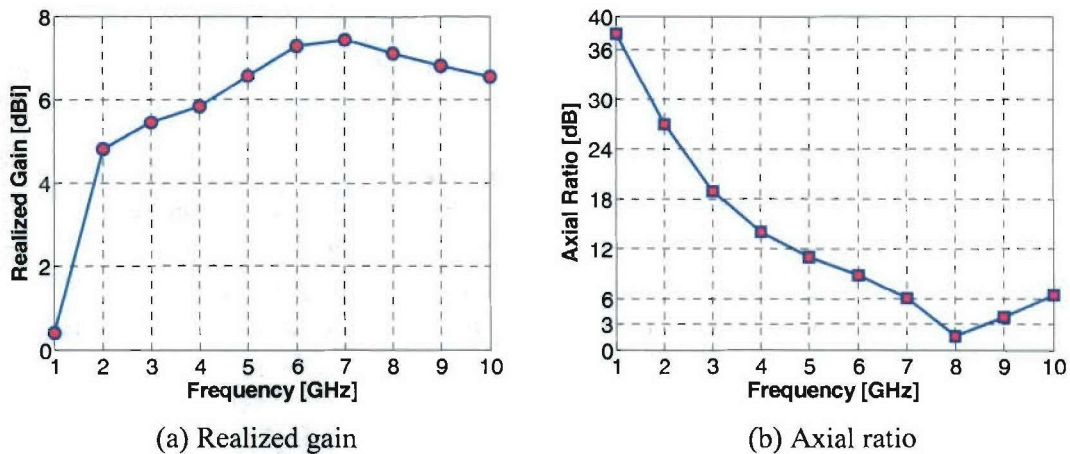


Figure 1.1-8 Simulated realized gain and axial ratio.

Conclusions

The new class of antenna, the tape helix, was introduced. Even though the test antenna was not optimized, it still showed good frequency and time domain performance. The ratio of height-to-diameter is about 3. So, the tape helix can be used for low frequency applications. In addition, the antenna structure can be printed on the thin film, allowing for easy mass production. It has very small weight.

References

- [1.1b-1] Zhi Ning Chen, "Novel bi-arm rolled monopole for UWB applications," *IEEE Transactions on Antennas and Propagation*, vol. 53, pp. 672-677, Feb. 1995.
- [1.1b-2] T. Warnagiris, "A Monopole With A Twist Revisited," *Microwave Journal*, pp. 54-74, July 2005.

Links to other tasks: This task supports the Tasks 1.1a, b, c, and e.

Schedule: Continues through the first year.

Personnel: Taeyoung Yang, GRA

Subtask 1.1c UWB antenna design (support of AWINN demonstrations)

Task objective: Design various UWB and other antennas needed for AWINN demonstrations

Accomplishments during reporting period: Below are summaries of antennas developed for AWINN applications.

Directional Antenna for SDR Receiver

An antenna is needed for a directional SDR receiver. The specifications for the antenna are listed in Table 1.1-2.

Table 1.1-2 Antenna specifications for SDR receiver

Size	Not a major constraint but an antenna dimension fitting inside a 6" x 6" x 6" is desired
Transmitted Pulse Width	Given a 500 ps pulse input, the transmitted pulse width should be 1000-1500ps, with minimal pulse dispersion or ringing
Gain	Not a major constraint
Weight	Not a concern
Absolute Frequency Range	Any range that is required to achieve the pulse width needed

Some of the possible antenna candidates follow.

Tapered Slot Antenna

Tapered slot antennas (TSA's) belong to a class of endfire traveling-wave antennas that demonstrated multioctave bandwidth, moderately high gain (7-10 dB), and symmetrical E- and H-plane beam patterns [1.1c-1]. The geometry of a TSA is shown in Fig. 1.1-9. There are many different types of TSA's available: Linearly Tapered Slot Antenna (LTSA), Vivaldi Antenna, which has exponential taper, and Constant Width Slot Antenna (CWSA) to name a few [1.1c-5]. Usually the bandwidth is limited due to the feed transition from microstrip or coaxial line to antenna slot [1.1c-2]. Many different **feeding** arrangements have been investigated in order to reduce the reflection loss between the feed transition.

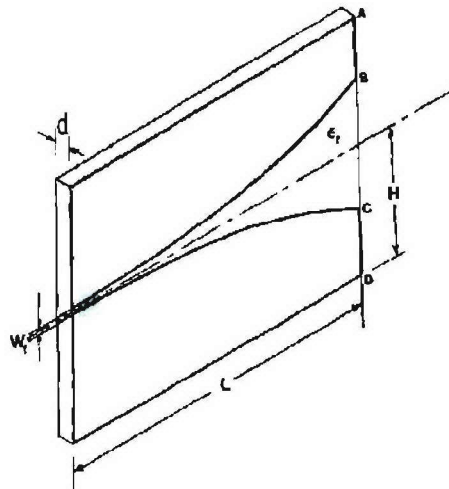


Figure 1.1-9 Geometry of tapered slot antenna [1.1c-3].

In order to reduce the loss in the feed transition, an antipodal geometry was introduced by Gazit [1.1c-4]. An example of an antipodal Vivaldi antenna is shown in Fig. 1.1-10. This antipodal geometry overcomes many limitations present in the conventional Vivaldi antenna so that it can function as an ultra-wideband antenna.

Another band limiting factor is the shape and the size of the antenna. The length of the antenna affects the beamwidth and the shape of the end of the antenna controls the side lobes and the back lobes [1.1c-4]. So, proper dimensions are necessary to achieve the bandwidth needed.

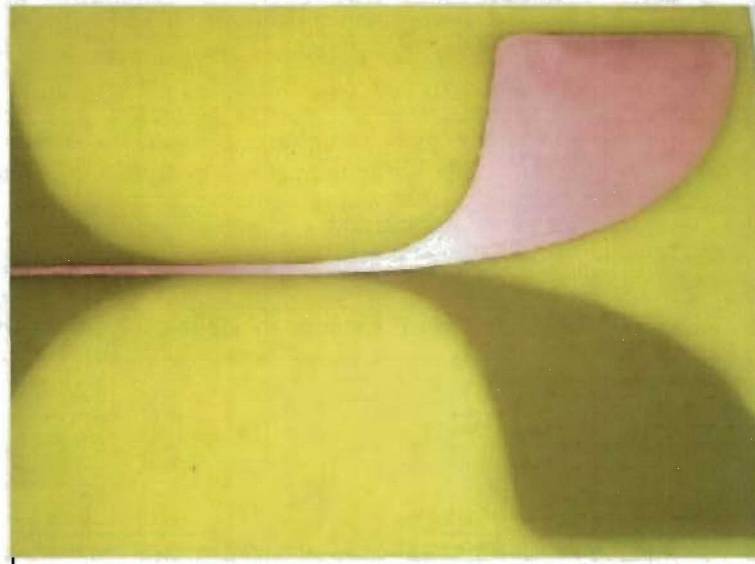


Figure 1.1-10 An antipodal Vivaldi antenna [1.1c-6]

TEM Horn

Transverse electromagnetic horn (TEM horn) antenna is a very popular wideband antenna. Its structure is also very simple. Typically a TEM horn consists of two triangular metal plates and a feeding structure and the horn is described completely with just three parameters: α , β , and s [1.1c-7]. Fig. 1.1-11 shows the geometry of a basic TEM horn antenna with the three parameters.

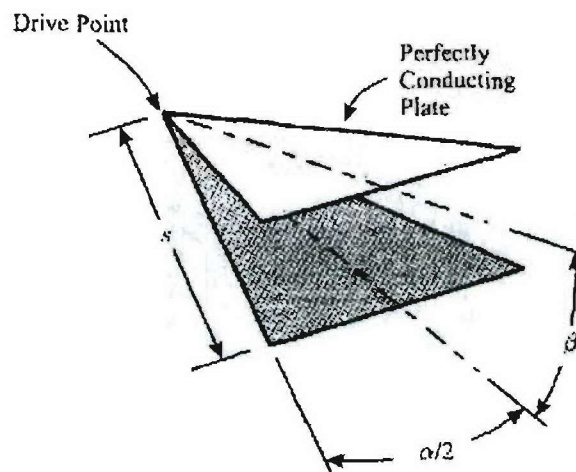


Figure 1.1-11 The geometry of a TEM horn antenna [1.1c-7].

Because a TEM horn is a balanced antenna, it requires a balun if an unbalanced feeding structure such as coaxial line or microstrip line is used [1.1c-8]. If a balun is required, the balun performance may limit the bandwidth of the TEM horn antenna. One way to use a TEM horn

without a balun is to use ground plane with one-half of the TEM horn plate [1.1c-6]. Also, the flaring and the length of the TEM horn antenna controls the bandwidth. When the separation between two plates approaches a half wavelength, it behaves as an efficient radiator [1.1c-9]. So, the separation height at the end of the TEM horn determines the low cutoff frequency of the horn.

The abrupt truncation of the TEM horn causes reflections at the end and back scattered fields diffracted from the horn edges. In order to reduce the reflections, resistive sheet or card is placed at the end of the TEM horn; it was shown that when the TEM horn is resistive loaded, the reflection was reduced [1.1c-10].

Impulse Radiating Antenna (IRA)

An IRA was developed for sending out a broadband pulse and some of its application includes target discrimination in a cluttered environment, aircraft identification, and target location through foliage [1.1c-11]. The reflector IRA is shown in Fig. 1.1-12 consists of a conical TEM feed and a reflector. When compared to a TEM horn of comparable size, reflector IRA performed better at higher frequency yielding narrower pulse response than a TEM horn [1.1c-11]. Later, a lens IRA was developed that did not require use of a reflector [1.1c-12].

One drawback of the reflector IRA is low efficiency. The reflector IRA uses resistive loading at the connection point between the TEM feed arm and the reflector in order to reduce reflection mismatch. It was shown that a reflector IRA has only 25% aperture efficiency [1.1c-13].

Helical Antenna

Helical antennas operate in two modes: normal or axial. A helical antenna and its dimensions are shown in Fig. 1.1-13. When the circumference (C) of the helix is on the order of a wavelength, the axial mode results, and when the diameter (D) and the length (L) shown in Fig. 1.1-13 are small compared to wavelength, the normal mode results [1.1c-14]. The axial mode helix bandwidth is 1.78:1 [1.1c-14]. The normal mode helix is potentially wideband, but it has an omnidirectional pattern, which is unsuitable for this task.

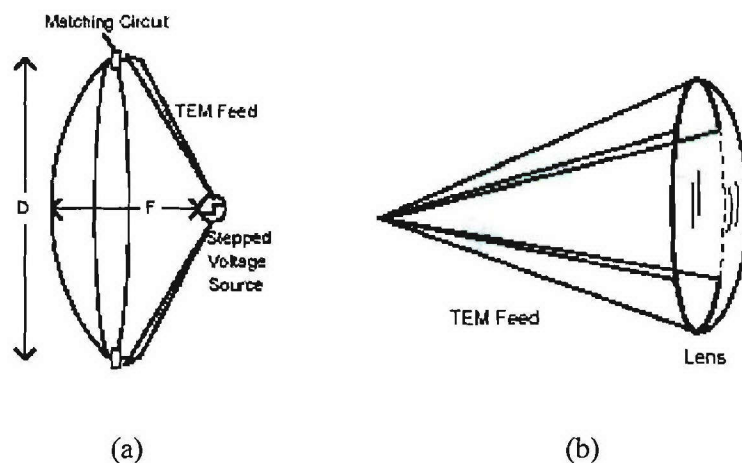


Figure 1.1-12 IRA Antennas: (a) reflector IRA and (b) lens IRA. [1.1c-12]

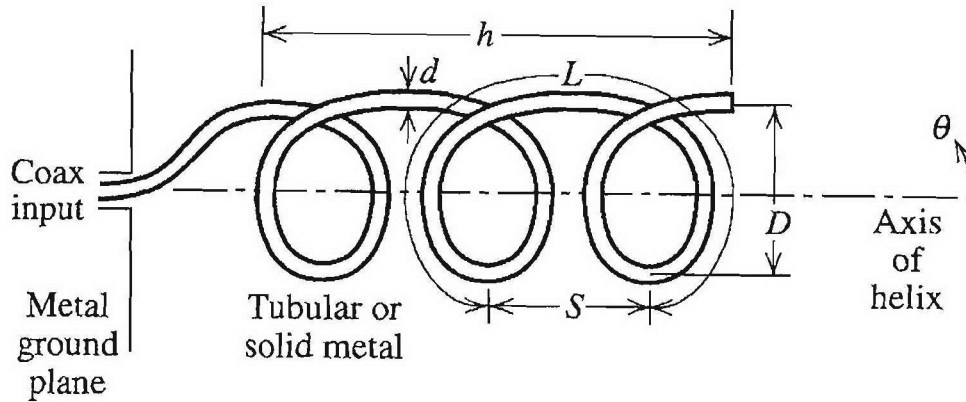


Figure 1.1-13 Geometry and dimensions of a helical antenna. [1.1c-14]

Spiral Antennas

Spiral antennas are a class of frequency independent antennas capable of bandwidths up to 40:1. A couple of examples of spiral antennas are shown in Fig. 1.1-14. Both of the spiral antennas are bidirectional antennas. In situations where a unidirectional antenna is needed, a ground plane or metal cavity behind the spiral is used to form a unidirectional beam pattern. Another approach is to form a unidirectional beam to use a nonplanar form. An example of conical equiangular spiral antenna is shown in Fig. 1.1-15. This antenna forms a single main beam directed off the tip of the cone in the $-z$ direction. Although the spiral antennas show wideband characteristics, there is severe dispersion, making it unsuitable for pulse transmission. The impulse response of a cavity backed Archimedean spiral antenna in Fig. 1.1-16 shows that chirp is present in the impulse response, rendering it unsuitable for pulse transmission.

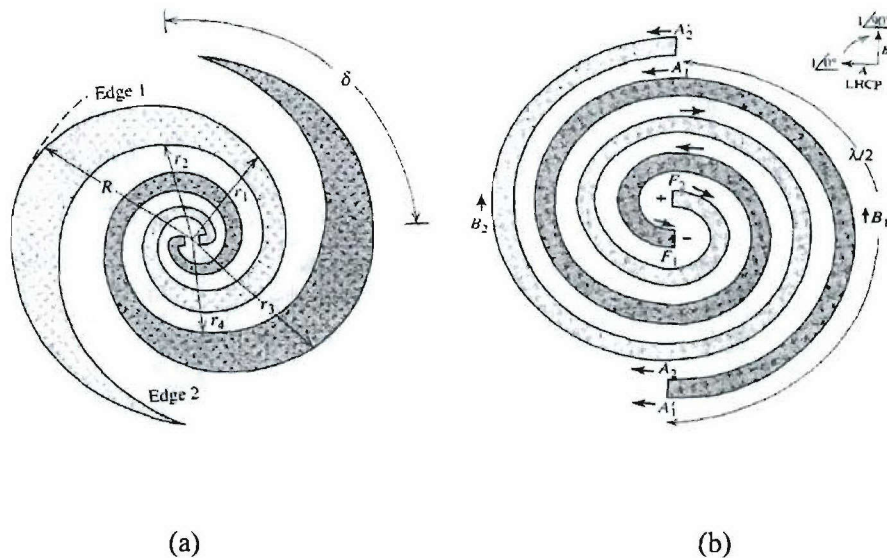


Figure 1.1-14 Spiral antennas: (a) Geometry of an equiangular spiral antenna, and (b) Geometry of an Archimedean spiral antenna. [1.1c-14]

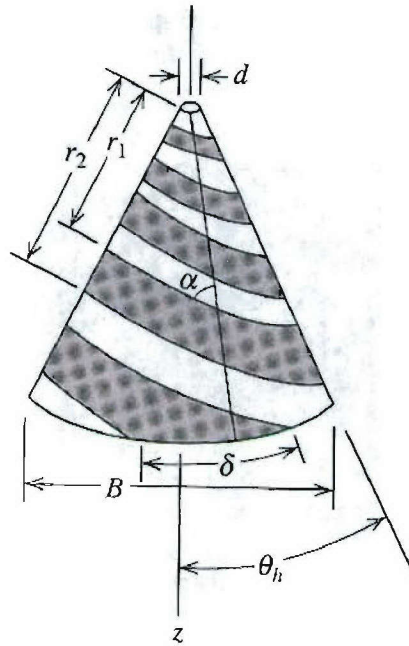


Figure 1.1-15 Geometry of a conical equiangular spiral antenna. [1.1c-14]

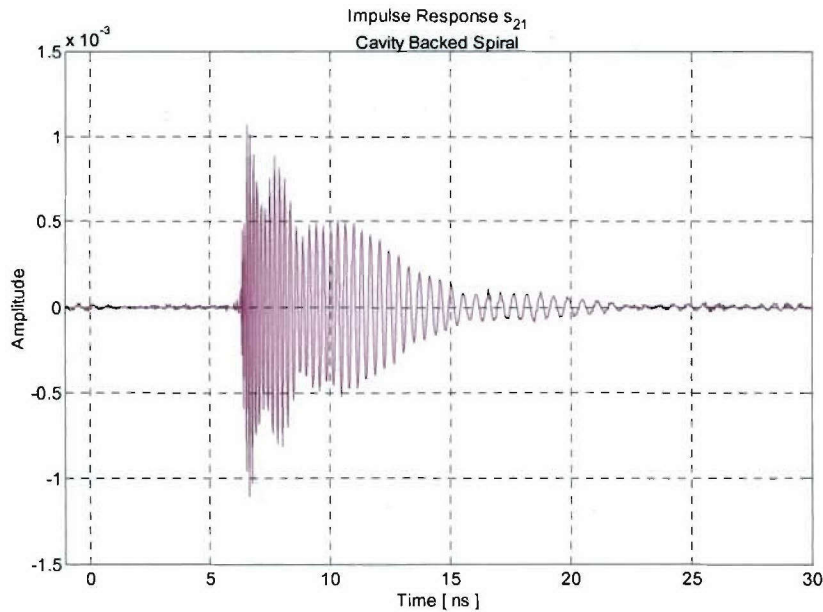


Figure 1.1-16 Measured impulse response of a cavity backed Archimedean spiral antenna [1.1c-6]

Log-Periodic Antennas

A log-periodic antenna is an antenna having a structural geometry such that its impedance and radiation characteristics repeat periodically as the logarithm of frequency [1.1c-14]. An example of a log periodic antenna, the log-periodic toothed trapezoid antenna, is shown in Fig. 1.1-17. Just like spiral antennas, log-periodic antennas are considered frequency independent and are able to

achieve a bandwidth of 10:1. But just like spiral antennas, its shape causes radiation of different frequencies at different times leading to severe dispersion, rendering it unsuitable for pulse transmission. The impulse response of a log toothed trapezoid antenna is shown in Fig. 1.1-18.

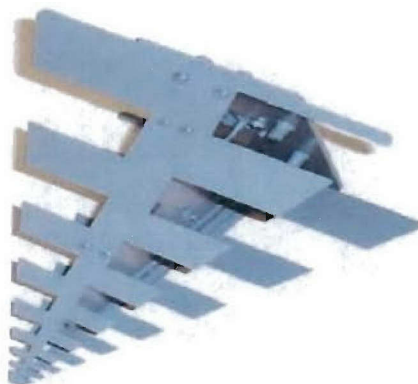


Figure 1.1-17 Log-periodic toothed trapezoid antenna. [1.1c-6]

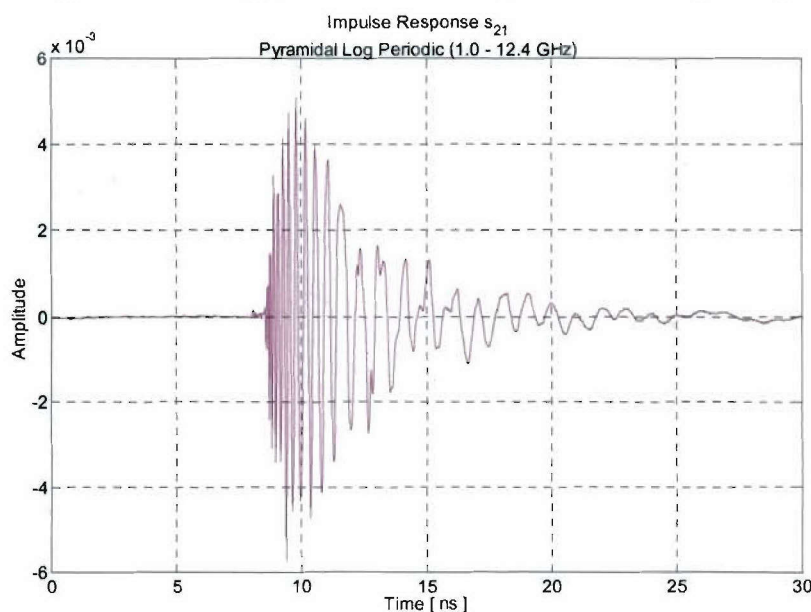


Figure 1.1-18 Measured impulse response of log-periodic toothed trapezoid antenna of Fig. 1.1-17. [1.1c-6]

Conclusions

Some wideband antennas and ultra-wideband antennas have been investigated. Tapered slot antenna, TEM horn and IRA seem to be good candidate for the task outlined in the introduction. They offer wide bandwidth along with little dispersion, which is critical for pulse transmission and reception.

Some other wideband antennas have been also investigated. The helical antenna, possibly a good candidate had omnidirectional beam pattern which is not suitable for this task. The frequency independent antennas, spiral and log-periodic antennas, showed the bandwidth needed for pulse transmission. However, both types had severe dispersion associated with them. The dispersion

causes chirp in the transmitted pulse and the ringing lasts for a long time. The dispersion is what causes these two types of antenna to be unsuitable for pulse transmission.

References

- [1.1c-1] K. F. Lee, and W. Chen. Ed. *Advances in Microstrip and Printed Antennas*. New York: John Wiley & Sons, Inc., 1997.
- [1.1c-2] J. D. S. Langley, P. S. Hall, and P. Newham. "Novel Ultrawide-bandwidth Vivaldi Antenna with Low Crosspolarisation", *Electronic Letters*, Vol. 29, Issue 23, pp. 2004-2005, November 11, 1993.
- [1.1c-3] R. Janaswamy, and D. Schaubert. "Analysis of the Tapered Slot Antenna" *IEEE Transactions Antennas and Propagation*, Vol. 35, Issue 9, pp. 1058 – 1065, September 1987.
- [1.1c-4] E. Gazit. "Improved Design of the Vivaldi Antenna" *IEE Proceedings*, Pt. H, Vol. 135 Issue 2, pp. 89-92, April 1988.
- [1.1c-5] K. S. Yngvesson, D. H. Schaubert, T. L. Korzeniowski, E. L. Kollberg, T. Thungren, and J. F. Hohansson. "Endfire Tapered Slot Antennas on Dielectric Substrates" *IEEE Transactions Antennas and Propagation*, Vol 33, Issue 12, pp. 1392 – 1400, December 1985.
- [1.1c-6] S. Lucil. "Ultra-Wideband Antenna Characterization and Measurements," *Ph. D. Dissertation*, Virginia Polytechnic Institute and State University, USA, 2004.
- [1.1c-7] R.T. Lee, and G. S. Smith. "A Design Study for the Basic TEM Horn Antenna" *IEEE Antennas and Propagation Magazine*, Vol. 46, Issue 1, pp. 86-92, February 2004.
- [1.1c-8] M. Manteghi, and Y. Rahmat-Samii. "A Novel UWB Feeding Mechanism for the TEM Horn Antenna, Reflector IRA, and the Vivaldi Antenna" *IEEE Antennas and Propagation Magazine*, Vol. 46, Issue 5, pp. 81-87, October 2004.
- [1.1c-9] D. A. Kolokotronis, Y. Huang, and J. T. Zhang. "Design of TEM Horn Antennas for Impulse Radar" *High Frequency Postgraduate Student Colloquium*, pp. 120-126, September 17, 1999.
- [1.1c-10] K. L. Shlager, G. S. Smith, and J. G. Maloney. "Accurate Analysis of TEM Horn Antennas for Pulse Radiation" *IEEE Transactions Electromagnetic Compatibility*, Vol. 38, Issue 3, pp. 414-423, August, 1996.
- [1.1c-11] H. L. Bertoni, L. Carin, and L. B. Felsen. Ed. *Ultra-wideband, Short-Pulse Electromagnetics*, Plenum Press, New York, 1993.
- [1.1c-12] L. Carin, and L. B. Felsen. Ed. *Ultra-wideband, Short-Pulse Electromagnetics*, Plenum Press, New York, 1995.
- [1.1c-13] C. J. Buchenauer, J. S. Tyo, and J. S. H. Schoenberg. "Aperature Efficiencies of Impulse Radiating Antennas" *IEEE Conference Proceedings Ultra-Wideband Short-Pulse Electromagnetics 4*, pp. 91-108, June 14-19, 1998.
- [1.1c-14] W. L. Stuzman, and G. A. Thiele. *Antenna Theory and Design 2nd Edition*, John Wiley & Sons, New York, 1998.

Links to other tasks: This task supports Tasks 1.2 and 4

Schedule: Initial design and fabrication will be completed and then performance improvement and optimization continues up to end of the year. The UWB system support antennas are to be completed by November 2005. Antennas in support of the robotic tasks will be developed in parallel with the UWB system support design.

Personnel: John Kim (GRA), Randall Nealy (Engineer), and W. Davis (PI)

Subtask 1.1d Antennas providing polarization, spatial, and pattern diversity – Evaluation of antennas in a MIMO environment

Task objective: Base station/access point antennas providing polarization, spatial and pattern diversity useful in supporting MIMO and space-time coding processing. Evaluation of antennas in a MIMO environment.

Accomplishments during reporting period: None to date

Links to other tasks: This topic may impact on the frequency selection and interaction of the measurements used for the Sea-Based cargo systems being considered in Task 3.

Schedule: The majority of the work on this task will follow the development of the antennas and is projected for Spring 2006.

Personnel: Garauv Joshi

Subtask 1.1e Support physics/engineering-based models for Digital Ships

Task objective: Support of Task 3 to develop physics/engineering-based templates for Digital Ships for radar simulation, including EW techniques.

Accomplishments during reporting period: None to date

Links to other tasks: In support of Task 3 on Digital Ships

Schedule: As requested by the personnel of Task 3 – Expected during Fall 2005

Personnel:

Subtask 1.1f Wideband balanced antenna/array feed networks

Task objective: Development of array feed networks for wideband balanced antenna systems such as the Fourpoint antenna investigated in the NAVCIITI program

Accomplishments during reporting period: The major activity this period has been a thorough review of baluns and as discussed below.

Introduction

Problems can arise with a balanced antenna if it is driven in such a way as to cause an imbalanced current. The imbalance can cause the radiation pattern to change, in the worst case causing a drastic and undesirable change in the pattern. One possible definition of “balance,” or the lack of is given by Weeks [1.1f-1]:

“In circuit technology, an unbalanced system is defined as one in which the two conductors are at different potentials with respect to ground (perhaps one of the conductors is at ground potential). The capacitance with respect to ground of the individual conductors is then different, and consequently the current in the two conductors may be different. In contrast, a balanced system is one in which the two conductors are respectively above and below ground potential by the same amount.”

So a general indication of a balanced condition of a system is its symmetry, both electrical and spatial.

There are many ways that an otherwise balanced antenna can become unbalanced. The type of antenna feed as well as the orientation of system components can have an effect on the balance of an antenna system. Driving a balanced antenna with an unbalanced feed will produce an unbalanced system. Positioning an otherwise balanced system (feed and antenna balanced) above a ground plane in a certain orientation can cause the antenna itself to become unbalanced. Orienting a feed line, balanced or otherwise, asymmetrically with respect to a balanced antenna can cause an imbalance.

A balanced antenna excited using an inherently unbalanced feed will introduce an imbalance. The classic example of this is a coaxial line fed dipole. See Fig. 1.1-19 [1.1f-2]. One arm of the dipole is generally connected to the outer conductor of the coaxial line with the other arm connected to the inner conductor of the coax. This abrupt change allows some of the current from the inside of the outer conductor of the coaxial line to flow down the outside of the outer conductor. Because this current is open to the outside and is not shielded it will radiate. The unwanted radiation pattern of the feed line will then adversely affect the desired pattern of the dipole. See Fig. 1.1-20 [1.1f-3].

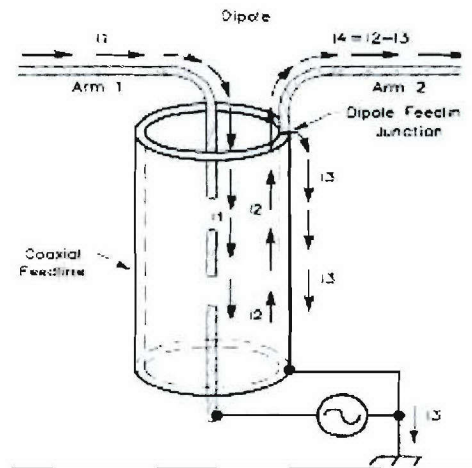


Fig. 1.1-19 Currents in a coax feeding a dipole antenna. [1.1f-2]

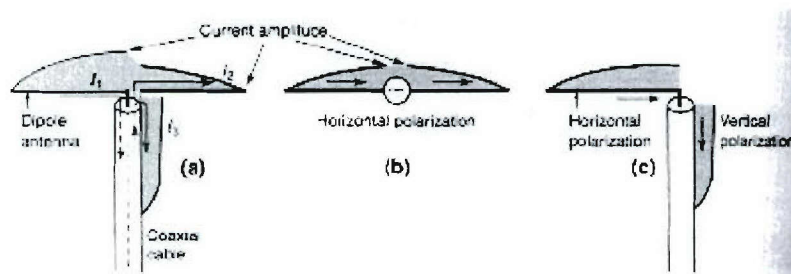


Fig. 1.1-20 Currents on dipole. [1.1f-3]

It is interesting to note that, though a system might be unbalanced, the overall effect on the antenna pattern might not be significant enough to warrant a remedy. Balanced directional antennas may be more sensitive to an imbalance, specifically because of the directional nature of the pattern [1.1f-4].

Antenna orientation with respect to ground can produce an unbalanced antenna. Imagine a dipole horizontally situated over a ground plane. Each arm of the dipole is equidistant from the ground plane so each arm is capacitively coupled to the ground plane by the same amount. This arrangement is thus balanced, assuming a balanced feed. Rotating the antenna by 90 degrees such that it is vertically aligned over the ground plane will cause an imbalance. This new geometry is unbalanced because the two arms are now located at different distances from the ground plane and thus have different values for coupling capacitance. See Fig. 1.1-21 [1.1f-5].

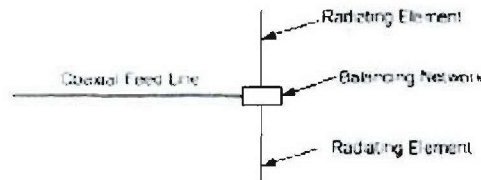


Fig. 1.1-21 Vertical orientation of a balanced antenna with respect to ground.

Feed line orientation with respect to the antenna can also produce an imbalance. An example of this is in the Fig. 1.1-22 [1.1f-6]. The feed line is oriented at a 45 degree angle to one arm of the dipole. This produces an uneven coupling between the antenna and the outside of the coaxial feed line, which can produce an unwanted current on the outside conductor.

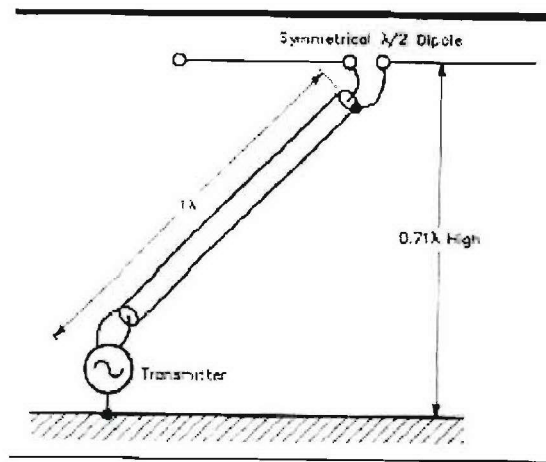


Fig. 1.1-22 A balanced antenna with an asymmetric feed orientation.

Class 1 Baluns

One of the two classes of baluns is shown in Fig. 1.1-23. [1.1f-7], [1.1f-8].

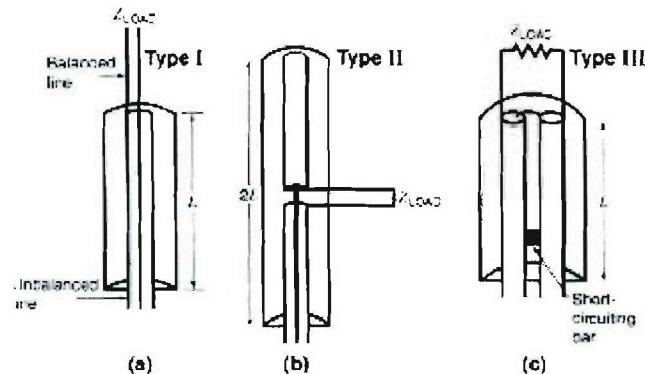


Fig. 1.1-23 Types 1,2, and 3 baluns.

The Type 1 balun works by presenting infinite impedance looking from the load back towards the feed line. This arrangement is usually narrowband. L is generally a quarter wavelength long. The Type 2 balun is comprised of two Type 1 baluns in series. This arrangement can provide a bit more bandwidth than Type 1. The Type 3 balun is a folded variation on the Type 2 balun. Again, this presents infinite impedance when looking from the load towards the feed line [1.1f-8].

One alternative form for the Type 3 baluns is shown in Fig. 1.1-23 [1.1f-9]

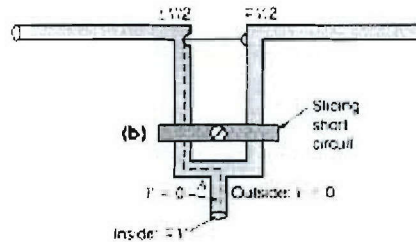


Fig. 1.1-24 Alternative form of Type 3 balun. [1.1f-9]

Figures 1.1-25 [1.1f-10] and 1.1-26 [1.1f-11] are printed circuit versions of Type 3 and Type 2 baluns, respectively.

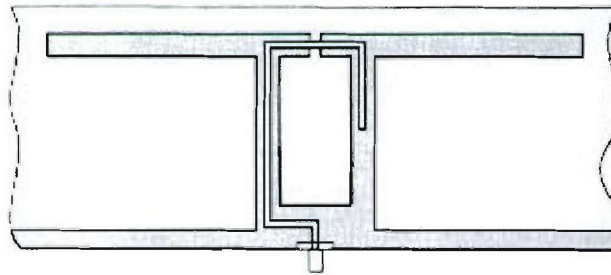


Fig. 1.1-25 Printed form of Type 3 balun. [1.1f-10]

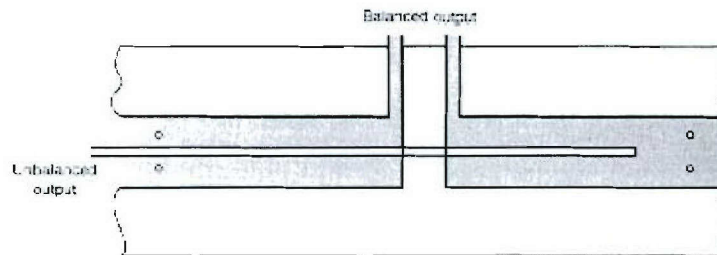


Fig. 1.1-26 Printed form of Type 2 balun. [1.1f-11]

Another type of balun is the half wave bypass balun, pictured in Fig. 1.1-27 [1.1f-12]. This type of balun can also provide impedance matching.

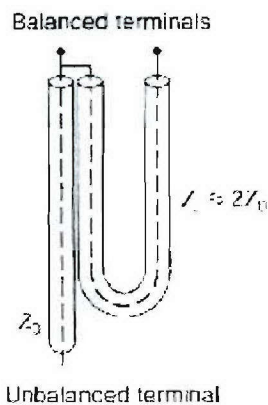


Fig. 1.1-27 The half-wave bypass balun. [1.1f-12]

Another implementation of a balun is the natural balun, which can be considered as an antenna with a built-in balun. Some antennas, for example a folded dipole, exhibit a current null in the center of the antenna on the continuous metal side. This is a good location for a coaxial cable feed connection. (This antenna would work well in the case that the imbalance is caused solely by an unbalanced feed line, but might not work if the imbalance is due to antenna orientation with respect to ground or feed line). See the Fig. 1.1-28 [1.1f-13].

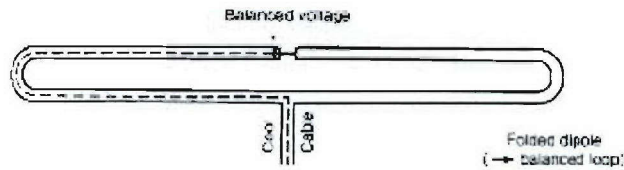


Fig. 1.1-28 A natural balun antenna.

Cutaway baluns can theoretically provide upwards of 100:1 bandwidth ratios. The major drawback is that they must be fairly long to achieve this ratio. See Fig. 1.1-29 [1.1f-14].

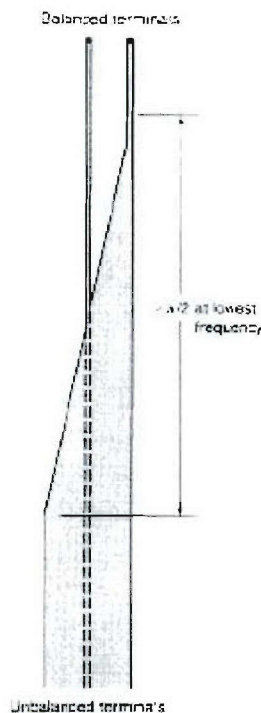


Fig. 1.1-29 A cutaway balun.

It is not uncommon to combine several particular balun designs to arrive at a hybrid. The balun in the Fig. 1.1-30 is a combination of a cutaway balun and a Type 3 balun.

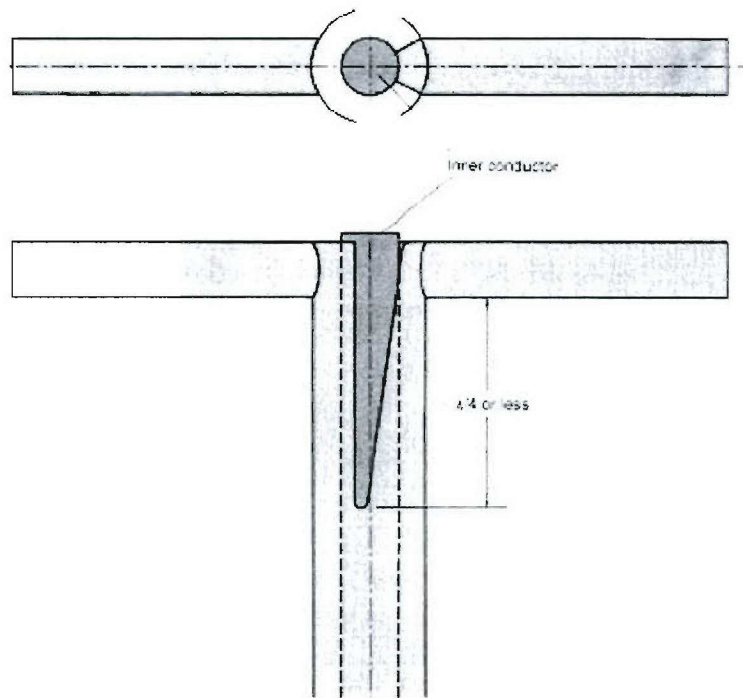


Fig. 1.1-30 A balun that combines the cutaway and Type 3 baluns.

Several other types of balun are presented below. Fig. 1.1-31 [1.1f-16] is a coiled coax choke type balun. Currents on the outside of the coax are choked off by the inductance of the coax loops while the signals inside the coax are unaffected.



Fig. 1.1-31 Coiled coax cable balun.

Figures 1.1-32 and 33 are more examples of choke type baluns. One has copper windings around a ferrite core [1.1f-17] and the other is a length of coax that is surrounded by small ferrite donuts [1.1f-18].

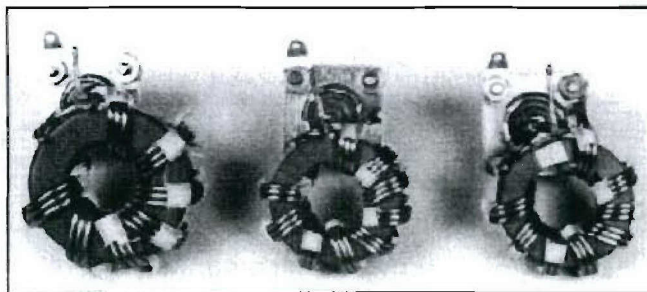


Fig. 1.1-32 Coiled ferrite balun. [1.1f-17]

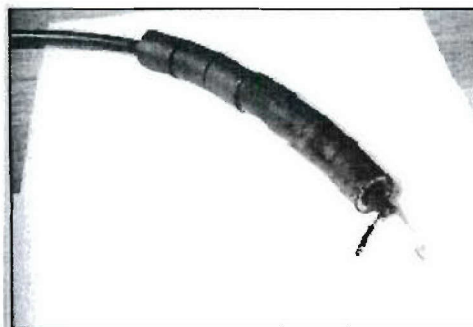


Fig. 1.1-33 Bead choke balun. [1.1f-18]

Class 2 baluns

In [1.1f-19], balun classification is made differently. The three classes used are: current balun, voltage balun, and 180 degree power divider. The current balun attempts to balance currents while the voltage balun attempts to balance a voltage with respect to some reference. Finally, as the name suggests, the 180 degree power divider attempts to split the power between two ports such that the current and voltage at each port are equal but opposite. It is shown in [1.1f-19] that all three balun types can be derived from a 180 degree 4-port hybrid by suitably terminating one of the hybrid ports. It is suggested that balun Types 1, 2, and 3 fall under the heading of current balun using this classification scheme.

Each balun type is suited for a particular imbalance caused by the system configuration. In particular, imbalance caused by asymmetrically situating a balanced dipole over a ground plane is best handled using a current balun.

Tapered line baluns are mentioned in various papers as being able to provide broadband performance. A potentially compact version is discussed in [1.1f-20]. Randall Nealy has suggested that either the branch line quadrature hybrid or the 180 degree tapered coupled line hybrid might provide a broadband balun solution.

Bibliography

- [1.1f-1] W. L. Weeks, *Antenna Engineering*. McGraw-Hill, 1968 p. 167
- [1.1f-2] R. Dean Straw, Editor, *ARRL Antenna Book*, 20th edition CT: The ARRL, Inc, 2003-2004, p. 26-17
- [1.1f-3] J. D. Kraus, R. J. Marhefka, *Antennas for All Applications*. Third edition. McGraw-Hill, 2002, p. 804.
- [1.1f-4] R. Dean Straw, Editor, *ARRL Antenna Book*, 20th edition CT: The ARRL, Inc, 2003-2004, p. 26-20.

- [1.1f-5] James S. McLean, "Balancing Networks for Symmetric Antennas –I Classification and Fundamental Operation," *IEEE Trans. Electromagn. Compat.*, vol. 44, p. 504, Nov. 2002.
- [1.1f-6] R. Dean Straw, Editor, *ARRL Antenna Book*, 20th edition CT: The ARRL, Inc, 2003-2004, p. 26-19.
- [1.1f-7] Herbert J. Reich, *Very High-Frequency Techniques*. McGraw-Hill Book Company, 1947, pp. 86-88.
- [1.1f-8] J. D. Kraus, R. J. Marhefka, *Antennas for All Applications*. Third edition. McGraw-Hill, 2002, p. 804.
- [1.1f-9] J. D. Kraus, R. J. Marhefka, *Antennas for All Applications*. Third edition. McGraw-Hill, 2002, p. 805.
- [1.1f-10] J. D. Kraus, R. J. Marhefka, *Antennas for All Applications*. Third edition. McGraw-Hill, 2002, p. 812.
- [1.1f-11] J. D. Kraus, R. J. Marhefka, *Antennas for All Applications*. Third edition. McGraw-Hill, 2002, p. 812.
- [1.1f-12] J. D. Kraus, R. J. Marhefka, *Antennas for All Applications*. Third edition. McGraw-Hill, 2002, p. 812.
- [1.1f-13] J. D. Kraus, R. J. Marhefka, *Antennas for All Applications*. Third edition. McGraw-Hill, 2002, p. 820.
- [1.1f-14] J. D. Kraus, R. J. Marhefka, *Antennas for All Applications*. Third edition. McGraw-Hill, 2002, p. 818.
- [1.1f-15] J. D. Kraus, R. J. Marhefka, *Antennas for All Applications*. Third edition. McGraw-Hill, 2002, p. 819.
- [1.1f-16] R. Dean Straw, Editor, *ARRL Antenna Book*, 20th edition CT: The ARRL, Inc, 2003-2004, p. 26-22.
- [1.1f-17] Jerry Sevick, *Transmission Line Transformers.*, Fourth edition Noble Publishing Corporation, 2001, p. 6-9.
- [1.1f-18] R. Dean Straw, Editor, *ARRL Antenna Book*, 20th edition CT: The ARRL, Inc, 2003-2004, p. 26-25.
- [1.1f-19] James S. McLean, "Balancing Networks for Symmetric Antennas –I Classification and Fundamental Operation," *IEEE Trans. Electromagn. Compat.*, vol. 44, pp. 507-511, Nov. 2002.
- [1.1f-20] Dean A. Hofer, Victor K. Tripp, "A Low-Profile, Broadband Balun Feed," *IEEE AP-S Symposium Digest*, pp. 458-461, 1993

Links to other tasks: This is related to potential directional antenna needs of other tasks, but has no direct link at present

Schedule: Begin Fall 2005

Personnel: Scott Bates, GRA

1.1.3 Importance/Relevance

The designed compact planar UWB antennas can accommodate the current needs for the handheld and mobile terminals. The designed frequency notch UWB antennas might provide a solution to reduce the inference to the existing other narrow band applications.

Specific requirements have been identified to set the antenna specifications for the software defined radio and sea-based tasks. This has been described in the task summary for this quarter.

A review of both wideband antennas and baluns has been performed to provide a focus of effort toward the antenna needs of the project.

Contact: The information of desktop antenna and propagation prediction is an item of critical interest in the design of topside platform configurations. This work is currently being done by the J-50, EMC team at the Naval Systems Warfare Center – Dahlgren Division. William Davis coordinating contact with Mike Hatfield of that section.

1.1.4 Productivity

Conference publications

1. W. A. Davis, “Development of New Antennas and Applications: Applications of UWB Antenna Modeling,” Institute for Defense and Government Advancement: Military Antenna Systems, 20-21 Sep 2005, Arlington, VA - Presented.

Books and Book Chapters

Honors and Recognitions

1. W. A. Davis, MC of the Institute for Defense and Government Advancement: Military Antenna Systems, 20-21 Sep 2005, Arlington, VA

Students supported

Taeyoung Yang, Scott Bates, John Kim Aug 15, 2005 – July 15, 2005

Faculty supported

Dr. William A. Davis, VTAG Director, Jan. 15, 2005 – present
Dr. Warren L. Stutzman, Faculty, Jan. 15, 2005 – present

Staff and other personnel supported

Mr. Randall Nealy, VTAG Engineer, Jan. 15, 2005 - present

1.2 Task 1.2 Advanced Software Radio

1.2.1 Overview

Task Goal: This task investigates an advanced Software Defined Radio (SDR) which can take advantage of the unique properties of Ultra Wideband communication—such as precision position location, ranging, and low probability of intercept—for Navy applications.

Organization: This task is managed by the Deputy Director of the Mobile and Portable Radio Research Group (MPRG) using the following personnel:

Jeffrey H. Reed, director
R. Michael Buehrer, faculty
William H. Tranter, faculty
Chris R. Anderson, GRA
Swaroop Venkatesh, GRA
Jihad Ibrahim, GRA
Maruf Mohammad, GRA

Summary: This quarter we focused on evaluating the prototype SDR receiver. The first phase of development of the advanced ultra wideband software defined radio (SDR) testbed involved constructing a prototype receiver. The receiver was a scaled-down version of the proposed final design, utilizing two ADCs in a Time-Interleaved sampling array, along with a Xilinx XC2VP30 FPGA. The goal in creating this prototype receiver was to test the underlying approach being used to develop the advanced SDR receiver. Specifically, we wanted to investigate the operation of components on the PCB at high clock frequencies (1 GHz for the ADCs, and up to 250 MHz for the FPGA). Additionally, it was important to verify that off-the-shelf components could be used to precisely control the ADC clock distribution network without significantly degrading the SNR or dynamic range of the receiver. The test results presented in this report outline the methodology used to evaluate the prototype receiver board and confirm that Time-Interleaved sampling of UWB pulses via off-the-shelf components is feasible.

SDR algorithm development during the past quarter has focused on a narrow band interference (NBI) mitigation scheme for ultra-wide bandwidth (UWB) signals using multiple receive antennas. The low spatial fading of UWB signals relative to NBI signals is exploited to provide “interference selection diversity”. Whereas classical selection diversity is designed to maximize the desired received signal power, the aim of interference selection diversity is to minimize the effective NBI power. Expressions for the probability of error of the selection diversity scheme are derived for both Rayleigh and Ricean NBI fading scenarios. The improvement in received signal-to-interference ratio is also mathematically investigated. It is shown that doubling the number of antennas results in a 3-dB performance improvement for the Rayleigh fading case. Less substantial gains are observed under Ricean fading.

Channel modeling this quarter focused on using discrete channel models for simulating error traces produced by wireless channels. Most of the time, these channels have memory and we use discrete time Markov chains, hidden or semi-hidden Markov models to simulate them. The primary advantage of using these models is easy, rapid experimentation and prototyping.

Investigation of distributed MIMO communication systems this quarter concentrated on evaluating the performance of a two-hop multiple relay based communication system with different combinations SSTC, AF and DF.

For ranging and position location, initial algorithms have been developed and tested in a simple proof-of-concept laboratory environment. The results indicate that ranging accuracy should be within a few inches, and that position location via evaluation of the multipath delay profile is possible. These algorithms are currently being updated to provide full 3-D ranging and positioning information, as well as incorporate the use of the SDR receiver.

1.2.2 Task Activities for the Period

Subtask 1.2a Develop flexible software radio platforms that include cross-layer optimization with capabilities for UWB and ad hoc networking

Task objective: The overall goal of this subtask is to design an advanced software-defined/reconfigurable radio which is optimized for ultra wideband communication, and then implement the system using off-the-shelf components. The software-defined radio implementation provides tremendous flexibility compared to a single hardware implementation—for example, providing the capability to utilize one of several different popular UWB modulation or multiple access schemes, to operate in one of several modes (communication, ranging, or data capture), as well as to utilize more traditional broadband communication schemes.

Accomplishments during reporting period: The first phase of development of the advanced ultra wideband software defined radio (SDR) testbed involved constructing a prototype receiver. The receiver was a scaled-down version of the proposed final design, utilizing two ADCs in a Time-Interleaved sampling array, along with a Xilinx XC2VP30 FPGA. The goal in creating this prototype receiver was to test the underlying approach being used to develop the advanced SDR receiver. Specifically, we wanted to investigate the operation of components on the PCB at high clock frequencies (1 GHz for the ADCs, and up to 250 MHz for the FPGA). Additionally, it was important to verify that off-the-shelf components could be used to precisely control the ADC clock distribution network, without significantly degrading the SNR or dynamic range of the receiver. The test results presented in this report outline the methodology used to evaluate the prototype receiver board and confirm that Time-Interleaved sampling of UWB pulses via off-the-shelf components is feasible.

Initial FPGA Configuration

To verify that the JTAG interface was connected properly to the FPGA, a simple FPGA bitstream was created and downloaded via iMPACT™. This initial testing phase was set up to verify that the FPGA could be programmed successfully, and that the FPGA operated as intended.

JTAG Configuration

Early in the design process, it was decided that FPGA configuration would be performed using the JTAG interface, which is connected to J10 on the receiver PCB. iMPACT™ and a Parallel IV cable were used to scan the JTAG chain (which consisted of only the FPGA), and it successfully recognized the on-board Xilinx FPGA. At this point, the bitstream was downloaded to the FPGA. LED D10, which is connected to the FPGA DONE signal, turned off when the configuration was complete, and served as a simple mechanism during the remainder of the testing process to verify that the FPGA configurations were properly downloaded.

FPGA Operation

The downloaded bitstream used a single-ended LVCMOS clock signal from the extra Global Clock pins located on J14 as an input to one of the FPGA's Digital Clock Managers (DCMs). The clock was driven by an external off-board oscillator first at a frequency of 25 MHz, and then at 100 MHz. The downloaded bitstream divided down the clock signal and flashed eight of the LEDs in a specific pattern. A reset signal from the Trigger pushbutton switch (S2) was used to reset the DCM as well as the flashing light pattern. Observation of the blinking LEDs (shown in Figure 1.2-1) verified that the following components were operating properly:

JTAG based FPGA configuration was successful and the FPGA operated as designed.

The correct power supply voltages were connected to the correct FPGA pins.

The FPGA Digital Clock Manager (DCM) was able to lock onto the input Global Clock signal.

Pressing the Trigger pushbutton was able to trigger the user global reset for the FPGA.

No solder joint failures on the FPGA pins connected to power, ground, or signals used by the bitstream.

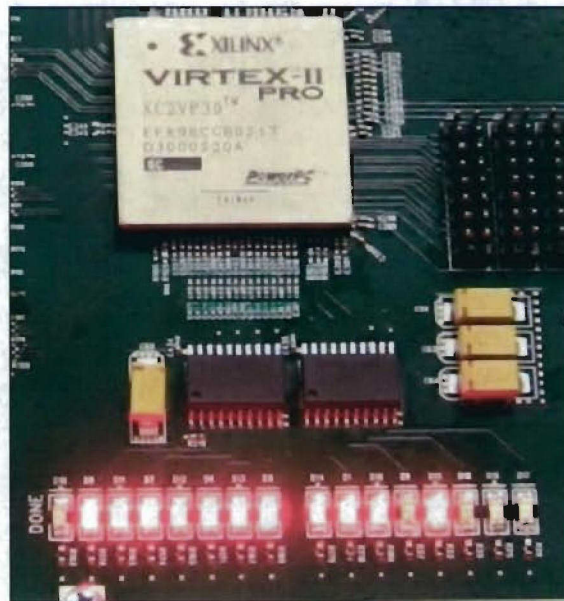


Figure 1.2-1 LEDs blinking in a programmed pattern verified that the FPGA had been properly configured.

As a secondary test of the DCMs, the blinking lights bitstream was regenerated to run off the ADC DREADY output signal (which is used as a differential clock input to the FPGA). The ADC input clock was slowly ramped up to a maximum of 1 GHz (which was the target operating frequency for the ADCs on the prototype receiver). Testing the DCMs at the maximum frequency was a critically important stage, as a higher potential for signal integrity problems exists for higher clock frequencies. In addition to the blinking lights, the DCM's lock signals were driven to external LEDs. The DCMs were able to lock onto the ADC's DREADY signal, meaning that the DREADY signal met all of the minimum timing and signal integrity requirements of the DCMs. Passing this test was extremely important, as the DREADY signals are used as the primary clock source in the FPGA.

Verify Power Distribution System Operation

The primary function of the Power Distribution System (PDS) is to meet all the static and transient current demands of all the IC's on the PCB. Large transient current demands are generated when multiple outputs in a given IC switch logic states simultaneously (known as Simultaneous Switching Outputs, or SSOs). The large transient current demands caused by SSOs—if not compensated for by the PDS—can cause temporary drops in voltage levels, leading to logic errors. On the prototype receiver, three PDSs contained a significant number of potential SSOs: the 1.5V FPGA core PDS, the 2.5V FPGA I/O PDS, and the 3.3V ADC output PDS. Each of these PDS's had a special connector so that a spectrum analyzer could observe the frequency response of the PDS. Large spikes in the spectrum indicate an unmet current demand at that particular frequency. The PDS's were tested with a 1 GHz square wave input to the ADCs (which maximized the number of SSOs on the ADC outputs), and the ADC clock inputs to the FPGA running at 500 MHz, along with an external Global Clock signal of 100 MHz.

1.5V PDS

The frequency spectrum for the 1.5V PDS is given in Figure 1.2-2. The figure shows a number of prominent spikes in the frequency range of 20 MHz – 300 MHz with a few isolated spikes with lower amplitudes, the largest of which is at 600 MHz (which happens to be a harmonic of both the 100 MHz Global Clock input and the 300 MHz PowerPC clock). The amplitude of the spikes ranges from about -80 dBm to a maximum of -50 dBm at 100 MHz. The spike at -50 dBm represents a transient voltage drop of approximately 1 mV, which is less than 1% of the FPGA core voltage.

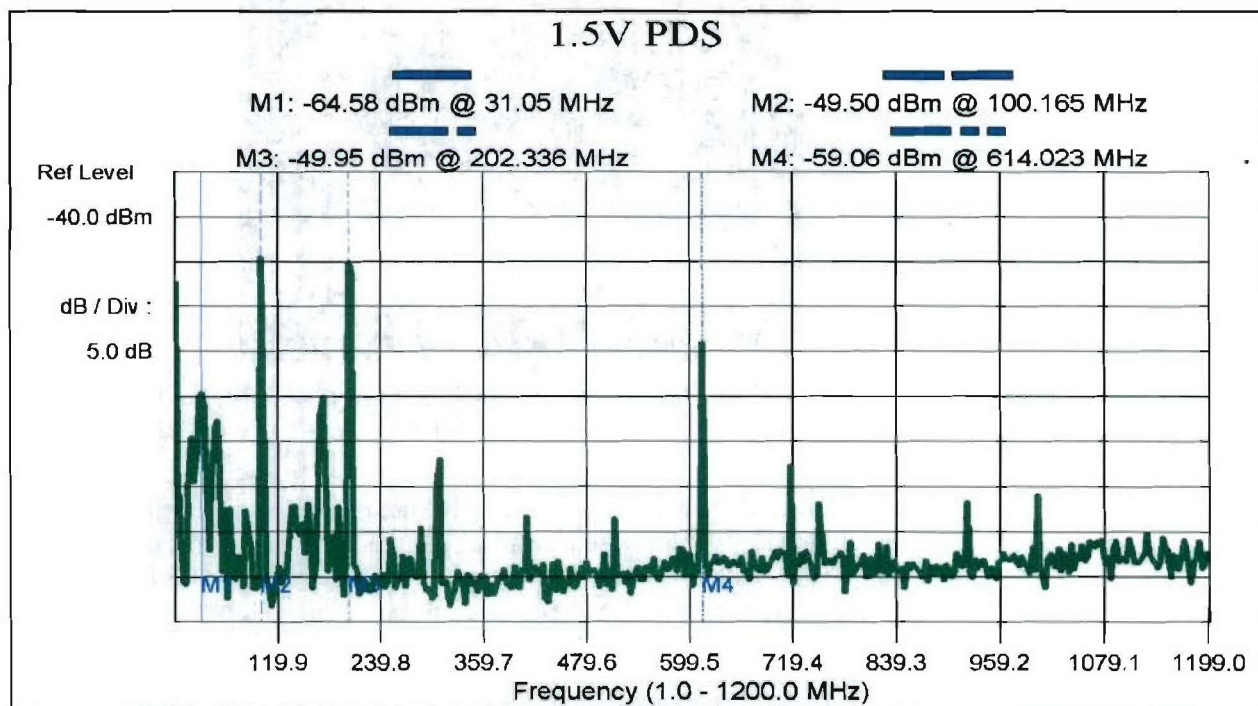


Figure 1.2-2 Frequency spectrum of the 1.5V Power Distribution System.

2.5V PDS

The frequency spectrum for the 2.5V PDS shown in Figure 1.2-3 has several discrete spikes between 100 MHz and 415 MHz, along with an isolated spike at 1 GHz. Amplitudes range from -80 dBm to a maximum of -58 dBm at 1 GHz. As with the 1.5V PDS, these represent transient voltage drops of less than 1 mV, which is well within tolerable limits.

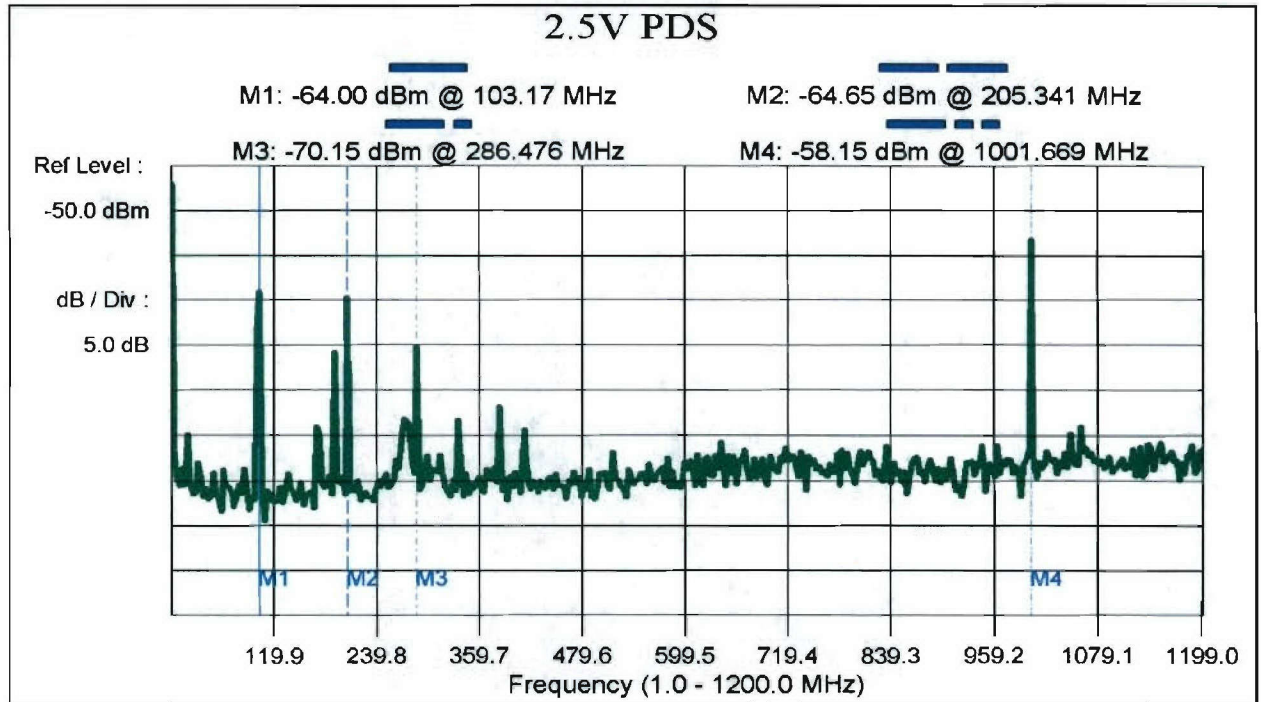


Figure 1.2-3 Frequency spectrum of the 2.5V Power Distribution System.

3.3V PDS

The frequency spectrum for the 3.3V PDS shown in Figure 1.2-4 has a discrete spike at 100 MHz, a group of spikes from 250 MHz – 330 MHz, and a single spike at 1 GHz. Amplitudes range from -77 dBm to a maximum of -55 dBm at 1 GHz. As with the other PDS's, these levels represent transient voltage drops of less than 1 mV.

The 1 GHz spike that occurs in both the 3.3V and 2.5V PDS, while not strong enough to cause signal integrity problems in the prototype receiver, does indicate a potential deficiency in the PDS design at higher frequencies, which should be taken care of for the final design.

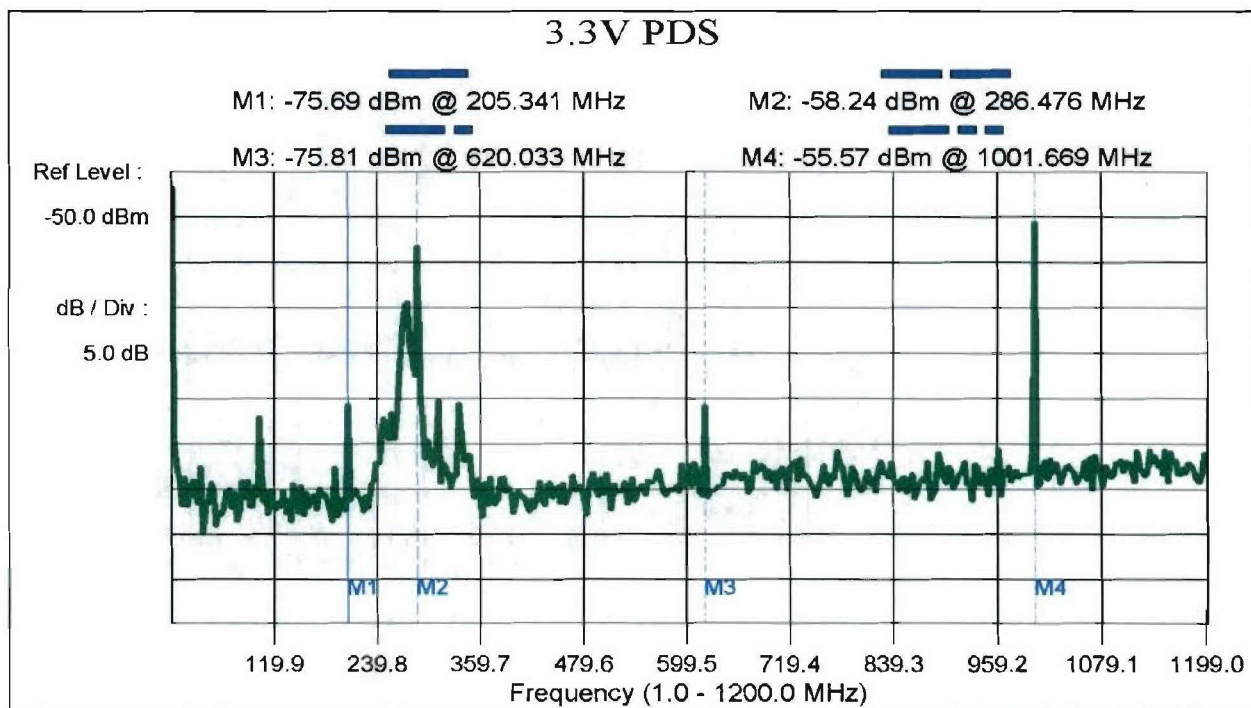


Figure 1.2-4 Frequency spectrum of the 3.3V Power Distribution System.

RS-232 Interface

The RS-232 interface is used primarily as a debugging and verification interface, as well as an alternative to the USB interface. To test the RS-232 interface, a null-modem cable was used to connect the RS-232 interface on the prototype board (J13) to a serial port on the host PC. A simple FPGA design was implemented that used the embedded PowerPC processor to perform a simple memory test and transmit the results to the host PC via a UART soft core. The UART core used is a proprietary Xilinx core which incorporates features described in National Semiconductor PC16650D device. A Maxim MAX3388 was used to translate the LVCMOS FPGA outputs into RS-232 compatible signaling levels. The data stream was captured using the Minicom terminal program running on a PC and determined to be error free, as shown in Figure 1.2-5.

```

Welcome to minicom 2.1

OPTIONS: History Buffer, F-key Macros, Search History Buffer, I18n
Compiled on Mar 29 2005, 09:39:09.

Press CTRL-A Z for help on special keys

-- Entering main() --
Starting MemoryTest for plb_bram_if_cntlr_1:
  Running 32-bit test...PASSED!
  Running 16-bit test...PASSED!
  Running 8-bit test...PASSED!
Starting MemoryTest for plb_bram_if_cntlr_2:
  Running 32-bit test...PASSED!
  Running 16-bit test...PASSED!
  Running 8-bit test...PASSED!
Starting MemoryTest for plb_bram_if_cntlr_3:
  Running 32-bit test...PASSED!
  Running 16-bit test...PASSED!
  Running 8-bit test...PASSED!
Starting MemoryTest for plb_bram_if_cntlr_4:
  Running 32-bit test...PASSED!
  Running 16-bit test...PASSED!
  Running 8-bit test...PASSED!
Starting MemoryTest for plb_bram_if_cntlr_5:
  Running 32-bit test...PASSED!
  Running 16-bit test...PASSED!
  Running 8-bit test...PASSED!
Starting MemoryTest for plb_bram_if_cntlr_6:
  Running 32-bit test...PASSED!
  Running 16-bit test...PASSED!
  Running 8-bit test...PASSED!
Starting MemoryTest for plb_bram_if_cntlr_7:
  Running 32-bit test...PASSED!
  Running 16-bit test...PASSED!
  Running 8-bit test...PASSED!
Starting MemoryTest for plb_bram_if_cntlr_8:
  Running 32-bit test...PASSED!
  Running 16-bit test...PASSED!
  Running 8-bit test...PASSED!
-- Exiting main() --

```

Figure 1.2-5 Output from Minicom which verified that the FPGA was able to communicate to a host PC using the RS-232 interface.

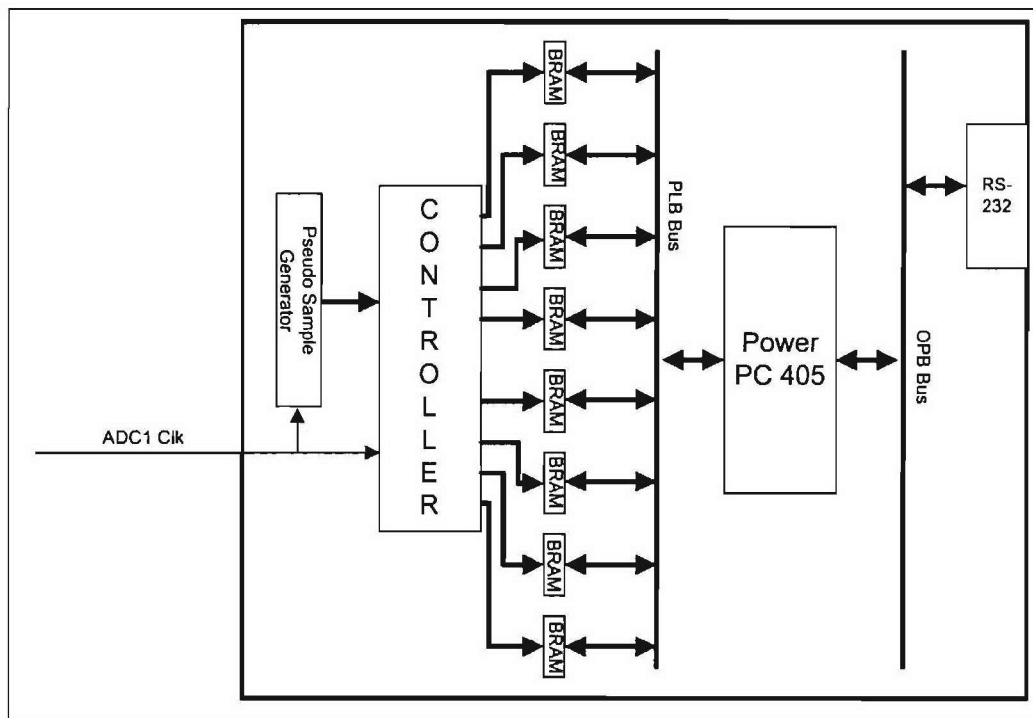


Figure 1.2-6 Block diagram of FPGA data capture infrastructure tested using a pseudo-sample generator.

Figure 1.2-6 is a block diagram for the ADC data capture. The ADC sample values are read into the FPGA's internal Block RAM (BRAM) memory. The BRAMs have two access ports, Port A is running off the ADC DREADY signal, and Port B runs off the Processor Local Bus (PLB) clock. The dual-port architecture allows the FPGA to use independent clocks for data read and write operations: ADC DREADY for the write operation and the PLB clock for the read operation. Once the BRAMs are full, the embedded PowerPC processor extracts the data from the BRAMS and streams it to the host PC over the RS-232 interface. For initial testing purposes, a pseudo-sample sequence was generated inside the FPGA and fed to the BRAMs in place of the ADC samples. Test results shown in Figure 1.2-7 indicate that all operations pertinent to data capture happened successfully.

```

Welcome to minicom 2.1

OPTIONS: History Buffer, F-key Macros, Search History Buffer, I18n
Compiled on Mar 29 2005, 09:39:09.

Press CTRL-A Z for help on special keys

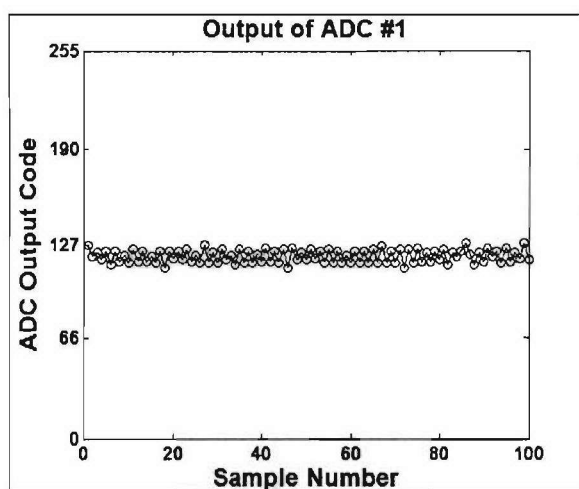
-- Entering main() --
Starting MemoryTest for plb_bram_if_cntlr_1:
1 = 00000000 D[00018000]=7d777972
1 = 00000001 D[00018004]=7a7a777f
1 = 00000002 D[00018008]=7b727a7a
1 = 00000003 D[0001800c]=747e747c
1 = 00000004 D[00018010]=767d7280
Starting MemoryTest for plb_bram_if_cntlr_2:
1 = 00000000 D[00010000]=a5a55a5a
1 = 00000001 D[00010004]=69699696
1 = 00000002 D[00010008]=a5a55a5a
1 = 00000003 D[0001000c]=69699696
1 = 00000004 D[00010010]=a5a55a5a
Starting MemoryTest for plb_bram_if_cntlr_3:
1 = 00000000 D[00004000]=74728073
1 = 00000001 D[00004004]=84757774
1 = 00000002 D[00004008]=76747472
1 = 00000003 D[0000400c]=70747277
1 = 00000004 D[00004010]=76777076
Starting MemoryTest for plb_bram_if_cntlr_4:
1 = 00000000 D[0001c000]=77000077
1 = 00000001 D[0001c004]=77737080
1 = 00000002 D[0001c008]=76007580
1 = 00000003 D[0001c00c]=74777373
1 = 00000004 D[0001c010]=77000075
Starting MemoryTest for plb_bram_if_cntlr_5:
1 = 00000000 D[00008000]=c104107d
1 = 00000001 D[00008004]=797f777a
1 = 00000002 D[00008008]=c17c88c4
1 = 00000003 D[0000800c]=89f17838
1 = 00000004 D[00008010]=07e1027d
Starting MemoryTest for plb_bram_if_cntlr_6:
1 = 00000000 D[0000c000]=7c783f72
1 = 00000001 D[0000c004]=817b7a80
1 = 00000002 D[0000c008]=8076027d
1 = 00000003 D[0000c00c]=75807481
1 = 00000004 D[0000c010]=7b7d3782
Starting MemoryTest for plb_bram_if_cntlr_7:

```

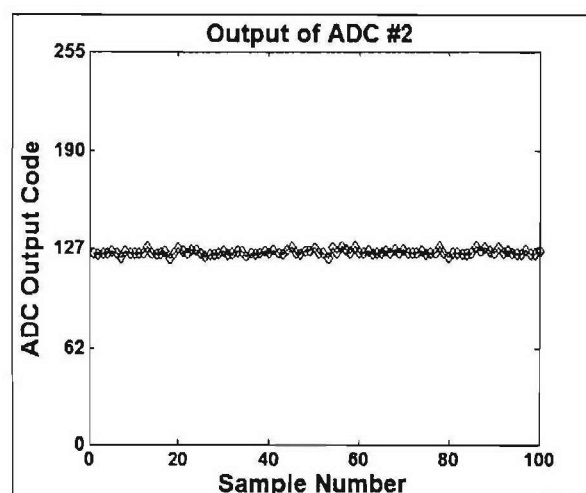
Figure 1.2-7 Output from Minicom which verified that all FPGA data capture infrastructure was fully operational. Infrastructure was tested by inputting a pseudo-sample sequence which is seen in the data stream above.

Data Capture with True ADC Inputs

The next step in verifying the data capture infrastructure was to determine if the FPGA could successfully latch in data from the ADC outputs. A new bitstream was generated which connected the FPGA pins to the BRAM Port A controller. Data capture was initiated by pressing the Trigger pushbutton switch. Once the BRAMs are full, the PowerPC outputs the data to the host PC using the RS-232 interface. For initial testing purposes, a 50Ω dummy load was connected to the UWB In input (J6) connector, to prevent accidentally overdriving the ADC analog input. The captured data was output to the host PC and saved to a file. Test results in Figure 1.2-8 show noisy data centered on the midrange of the ADC's output (output code 127).



(a)



(b)

Figure 1.2-8 Output of the ADCs when a 50- Ω dummy load is connected to the UWB In input (Note the slight gain and offset mismatch). (a) Output of ADC#1, and (b) Output of ADC#2.

DC Input Data Capture

DC voltages were connected to the prototype receiver PCB signal input (J6) to test the following:

- ADC full-scale analog input range.
- Solder joint failures (leading to outputs that are stuck high or low).
- ADC DC Offset Calibration

ADC Analog Range

The ADC input was connected to a DC voltage which was set equal to either the maximum or minimum allowed analog input voltage (+250 mV for the maximum, -250 mV for the minimum). The resulting output should have been either an all “1’s” code or an all “0’s” code for their respective cases. During testing, it was observed that the ADC overrange output was being asserted, meaning that the analog input was being overdriven. The overrange bit remained high until the input voltage was reduced to ± 63 mV, which was not the expected behavior for the ADC. After consulting with MAX104 datasheets and Maxim application engineers, it was discovered that in the prototype receiver’s design, the ADC’s internal bandgap reference pin, REFIN, was inadvertently left floating. Not connecting the REFIN pin resulted in minimization of the ADC analog input range, however, the functionality of the ADC remained essentially unchanged.

Solder Joint Failure

To test for solder joint failures, the ADC inputs were connected to a variable DC power supply, and DC voltages were varied over the ADC's input range (± 63 mV). During this test, it was observed that on Board #002, ADC #2's output code always showed noisy data and did not track the changing input. Further investigation revealed that the analog input of ADC#2 was inoperative. On Board #001, several outputs on the primary bus of ADC #002 were unresponsive to the changing DC input voltage. Close inspection of the PCB revealed cold solder joints in the resistive voltage divider network adjacent to the ADC. The solder joints were repaired and the ADC outputs were observed to behave as expected.

ADC DC Offset Calibration

The MAX104 ADC's provide a mechanism for matching the ADC offsets in a Time-Interleaved Sampling array. On the prototype receiver, a variable resistor (R27 for ADC#1 and R39 for ADC#2) are used to adjust the DC offset on the analog side of the ADC. The MAX104 has an adjustment range of ± 5.5 Least Significant Bits (LSBs). Calibration involved inputting a fixed DC voltage and matching the ADC output codes by adjusting the variable resistors.

Data Capture with Sinusoidal Input

Waveform Reconstruction from Individual ADCs

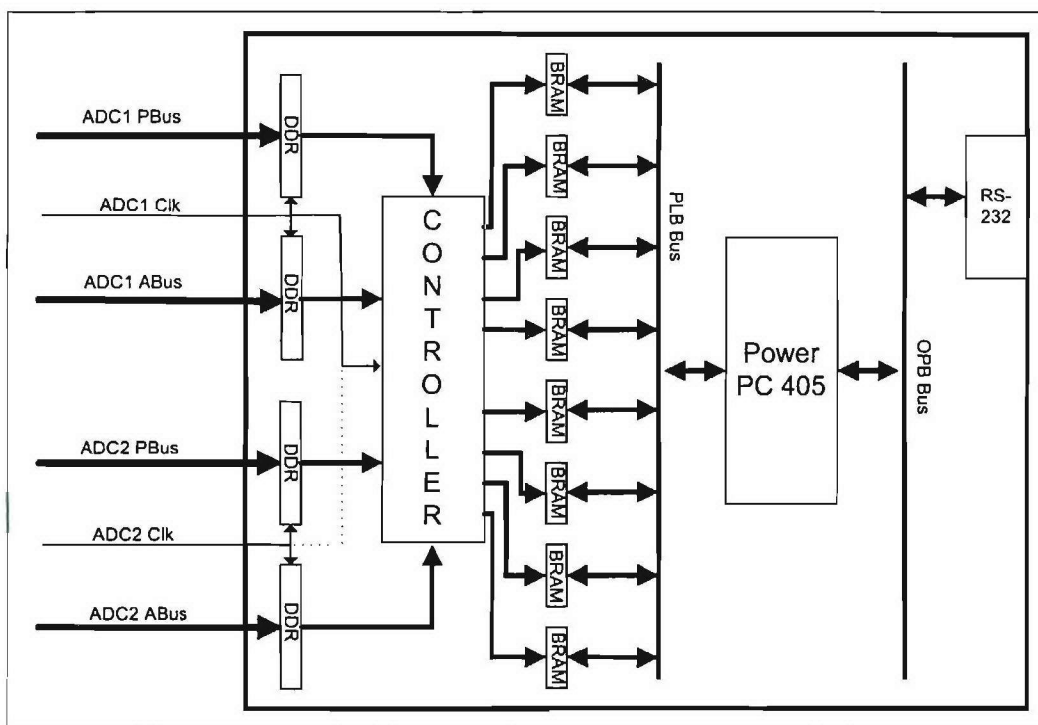


Figure 1.2-9 Block diagram of FPGA data capture from the individual ADCs.

Each of the ADCs output data that is synchronous with their respective clock signals. In the Time Interleaved Sampling architecture, the clock signals are intentionally out of phase, hence each ADC output must be latched into the FPGA using its respective clock signal. Inside the FPGA, the single BRAM controller can be driven by either of the ADC clock signals. To test the individual ADC data capture, two different bitstreams were generated: one to read in data only

from ADC#1 (as illustrated in Figure 1.2-9), and a second to read in data only from ADC#2 (Represented by the dotted line in Figure 1.2-9). Using separate bistreams for each ADC avoided metastability issues that would have occurred if the controller, running off ADC#1's clock, attempted to latch in data from ADC#2, or vice-versa. The individual ADC sampling clocks were set to a frequency of 500 MHz, and a 12 MHz signal was input to the receiver's UWB In input. The captured data was transmitted to the host PC and saved to a file. The waveforms and their spectrums were reconstructed using a MATLAB routine, and are shown in Figures 1.2-10 and 1.2-11.

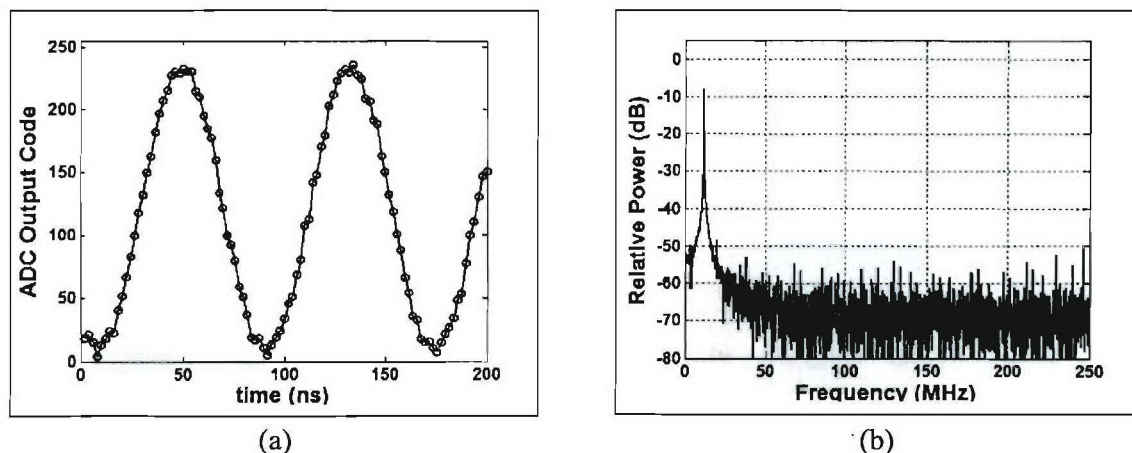


Figure 1.2-10 Captured output from ADC #1 for a 12 MHz CW input at a sampling frequency of 500 MHz. (a) Time domain output, and (b) Frequency spectrum of the captured output.

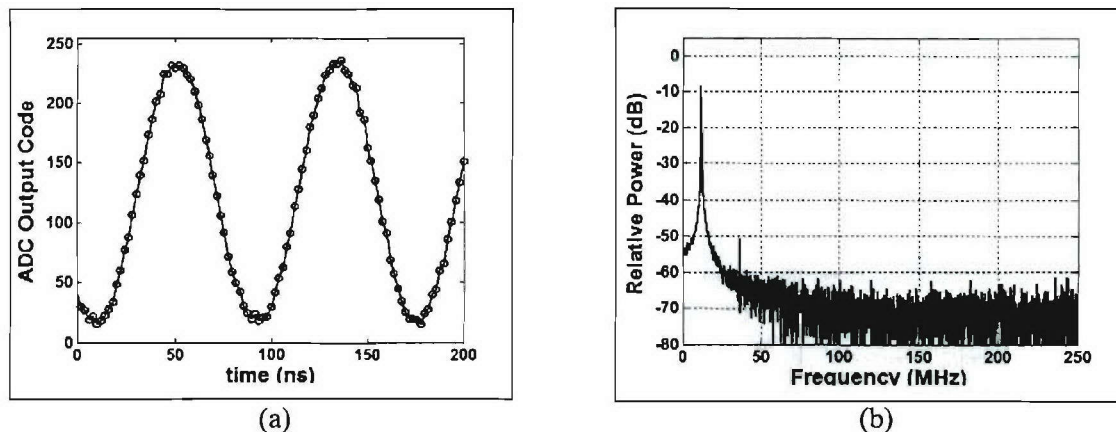


Figure 1.2-11 Captured output from ADC #2 for a 12 MHz CW input at a sampling frequency of 500 MHz. (a) Time domain output, and (b) Frequency spectrum of the captured output.

Waveform Reconstruction from Time Interleaved ADCs

As discussed above, metastability issues arise when the controller tries to read in ADC#1's output data when running on ADC#2's clock. To avoid metastability, a synchronizer is used to move data safely across clock domains, as illustrated in Figure 1.2-12.

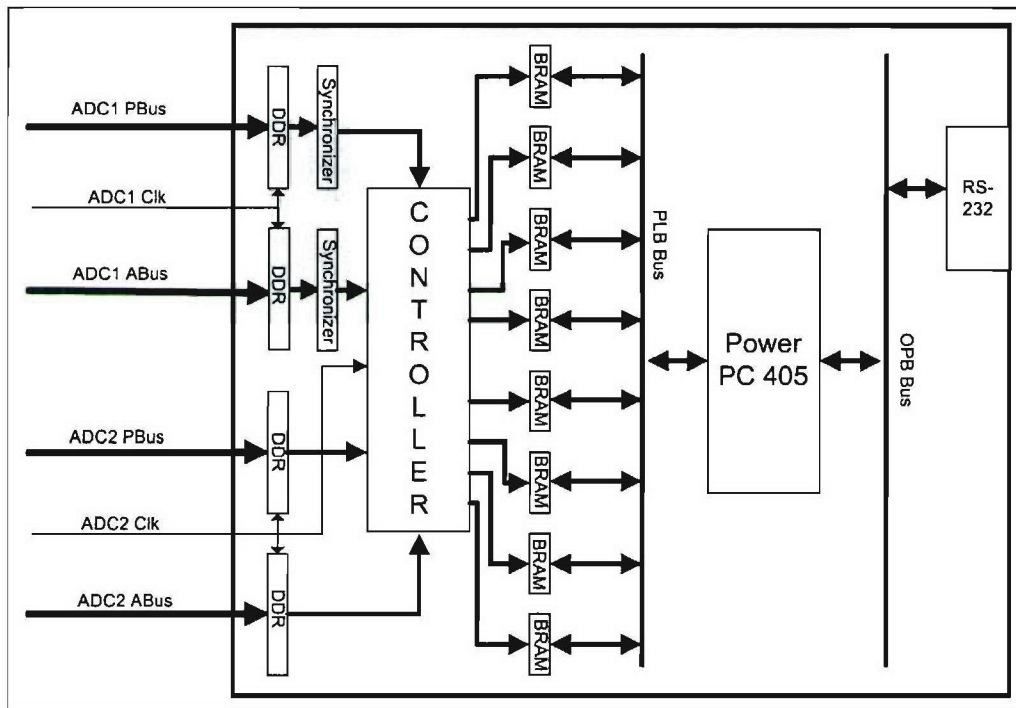
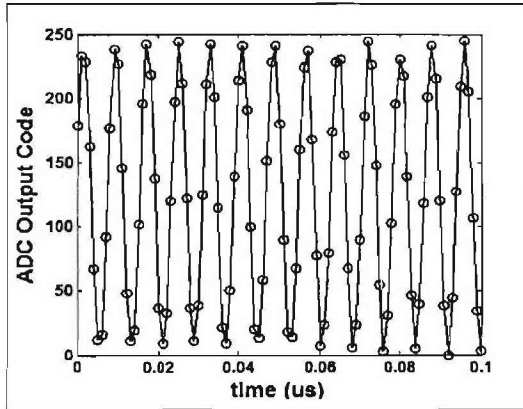
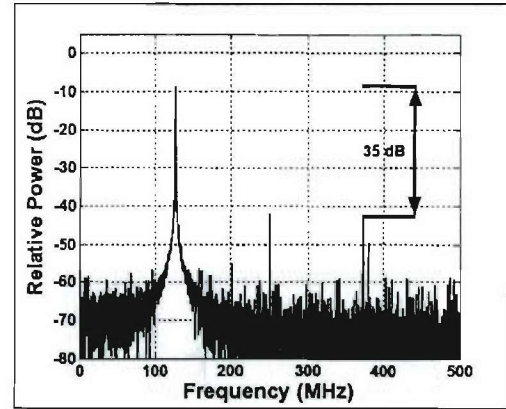


Figure 1.2-12 Block diagram of FPGA data capture with ADC sample de-interleaving.

A C routine written for the embedded PowerPC processor de-interleaves the data while reading it from the BRAMs. To test the operation of the de-interleaving routine, several CW tones were input to the UWB In input of the receiver. For the first round of testing, the individual ADC clocks were driven from an Agilent ESG-D3000A signal generator at a frequency of 500 MHz. The programmable clock delay chips for the ADCs were adjusted to provide an effective sampling frequency of 1 GHz. The waveforms and their spectrums were reconstructed with a MATLAB routine, and one example is plotted below in Figure 1.2-13. In the figures, note that several spurious signals are present, the strongest of which occur at 250 MHz and at $f_c - f_{in}$ (where f_c is the ADC clock signal and f_{in} is the frequency of the input signal). These spurs are caused by slightly mismatched delays, as well as clock jitter present on the output of the Agilent signal generator. Nevertheless, the dynamic range of the receiver is approximately 35 dB.



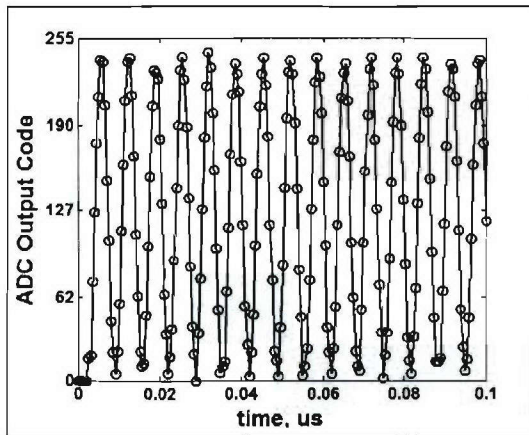
(a)



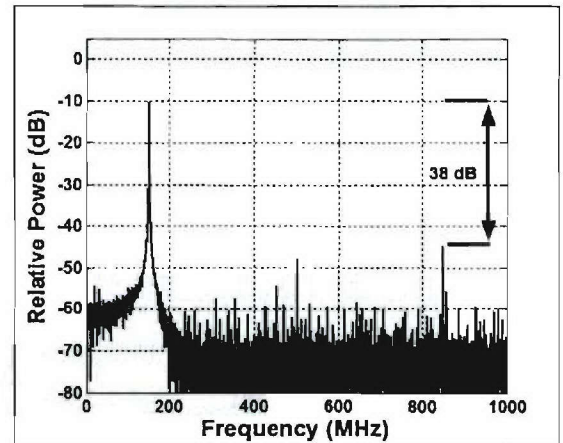
(b)

Figure 1.2-13 Time-Interleaved output of the prototype receiver PCB for a 127 MHz CW input at an effective sampling frequency of 1 GHz. (a) De-interleaved time domain output, and (b) Frequency spectrum of the de-interleaved output.

For the second round of testing, the individual ADC clocks were set to a frequency of 1 GHz, yielding an effective sampling frequency for the receiver of 2 GHz. As above, several CW signals were input to the receiver, and one example of the resulting reconstructed waveform and its spectrum is shown below in Figure 1.2-14. Note that the dynamic range is approximately 38 dB, whereas the ideal dynamic range (if a single 2 GHz 8-bit ADC was used on the receiver) is 48 dB. The reduction in dynamic range is primarily due to timing jitter (since the Agilent oscillator is somewhat noisy), but is also due to minor gain and offset mismatches between the two ADCs.



(a)



(b)

Figure 1.2-14 Time-Interleaved output of the prototype receiver PCB for a 151 MHz CW input at an effective sampling frequency of 2 GHz. (a) De-interleaved time domain output, and (b) Frequency spectrum of the de-interleaved output.

Data Capture with a UWB Pulse Input

The final test of the prototype receiver board was to successfully capture and reconstruct a UWB pulse generated by a simple MSSI pulser available in the MPRG lab. To prevent overdriving the

ADCs, the pulser output was attenuated before connecting it to the UWB In input of the prototype receiver. The individual ADC clocks were set to a frequency of 1 GHz, yielding 2 GHz effective sampling frequency for the receiver. Captured data was output to the host PC and post-processed in Matlab as with the CW signals. For comparison purposes, the same UWB pulse was also digitized using a Tektronix TDS580D at a 2 GHz sampling frequency. The voltage recorded by the oscilloscope was converted into an equivalent ADC output code level, based on the measured analog input range of the ADCs of ± 63 mV. Both signals are plotted together in Figure 1.2-15. Note that the two pulses are nearly identical in both shape and time duration.

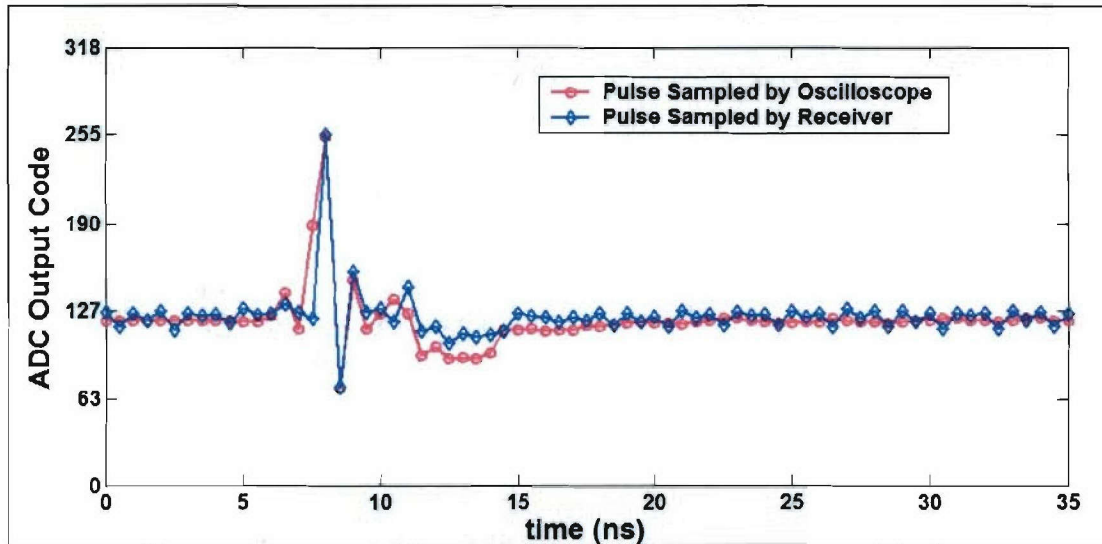


Figure 1.2-15 Comparison of a UWB pulse sampled by a Tektronix oscilloscope and the same UWB pulse sampled by the prototype receiver.

Conclusions: The tests performed for this report have successfully demonstrated that all of the critical hardware components on the prototype UWB software radio receiver are fully functional. Data capture of both CW and UWB pulses was used to demonstrate that Time-Interleaved sampling at such high frequencies and using off-the-shelf components is feasible. Additionally, it was demonstrated that data paths inside the FPGA could operate at clock frequencies of 250 MHz, which is critically important when the individual ADC sampling clocks are set to 1 GHz. The next stage is to construct the FPGA firmware for UWB signal acquisition, synchronization, and data transmission.

Schedule:

- January – July 2005
 - Develop 2-ADC Prototype Receiver
- August-September 2005
 - Fabricate Receiver
 - Evaluate Prototype Receiver Hardware and FPGA Code
- October-December 2005
 - Develop 8-ADC Full Receiver
 - Begin Integration of Receiver with Other AWINN Activities
- 1st Quarter 2006
 - Fabricate 8-ADC Full Receiver
 - Update Transmitter Design

- Fabricate DC Power Board
- Verify Operation of Receiver Hardware and FPGA Code
- 2nd Quarter 2006
 - Demonstrate Transceiver Operation
 - Integrate Transceiver with Other AWINN Activities

Personnel:

Chris R. Anderson – Transmitter and Receiver Hardware Development
 Deepak Agarwal – Receiver FPGA Code Development

Subtask 1.2b Software radio research applied to UWB, including design parameter space exploration

Task objective: The objective of this task is to investigate innovative SDR architectures and algorithms for both traditional broadband and UWB communications. These algorithms will be implemented on the advanced SDR receiver developed in Subtask 1.2a.

Rayleigh and Ricean NBI Interference Mitigation based on Multiple Antennas

In this part of our research, a narrow band interference (NBI) mitigation scheme for ultra-wide bandwidth (UWB) signals using multiple receive antennas is examined. The low spatial fading of UWB signals relative to NBI signals is exploited to provide “interference selection diversity”. Whereas classical selection diversity is designed to maximize the desired received signal power, the aim of interference selection diversity is to minimize the effective NBI power. Expressions for the probability of error of the selection diversity scheme are derived for both Rayleigh and Ricean NBI fading scenarios. The improvement in received signal-to-interference ratio is also mathematically investigated. It is shown that doubling the number of antennas results in a 3- dB performance improvement for the Rayleigh fading case. Less substantial gains are observed under Ricean fading.

More specifically, the expression for probability of error for NBI Rayleigh fading is found to be:

$$P_e = Q\left(\frac{E_p M d^2}{2P_I(a^2 + b^2)\sigma^2}\right),$$

where M is the number of antennas, $d \approx 1$ is the UWB component in the decision statistic, σ^2 is related to the NBI fading distribution, P_I is the NBI power, and a and b are constants related to the cross-correlation between the receiver template and the NBI tone. Notice that we get a 3-dB gain when the number of antennas is doubled.

For Ricean fading, the probability of error is found to be:

$$P_e = \frac{M}{\pi\sigma^2} \int_{\frac{E_p d}{A}}^{\infty} \left(\sin^{-1}\left(-\frac{\sqrt{E_p d}}{Ax}\right) + \frac{\pi}{2} \right) x Q_1^{M-1}\left(\frac{s}{\sigma}, \frac{x}{\sigma}\right) e^{\frac{s^2+x^2}{2\sigma^2}} I_0\left(x \frac{s}{\sigma^2}\right) dx,$$

where $A = \sqrt{2P_I(a^2 + b^2)}$, s is the Ricean parameter, $Q_1()$ is the generalized Marcum Q function, and $I_0()$ is a modified Bessel function of the first kind. Simulation results will show that gains are less substantial for Ricean fading when the number of antennas is increased.

A simulation using UWB biphas modulation was carried out with 1, 2, 4 and 8 receive antennas to gauge the performance of the system. NBI is modeled by a 6.3 GHz tone, and is assumed to undergo independent (Rayleigh or Ricean) fading over the different receive antennas. In order to model the UWB channel, we employ impulse responses from indoor NLOS channel measurements taken at MPRG. UWB biphas modulation is used. It is assumed that the correlator template is matched to the received UWB pulse shape (i.e. perfect channel knowledge is assumed for the UWB signal).

The probability of error of the SD scheme under Rayleigh fading is displayed in Figure 1.2-16. First, note that the simulated results match the theoretical expression in (18). Second, notice that performance improves by 3 dB when the number of antennas is doubled. Performance for Ricean fading ($K = 5$, where K is the ratio of LOS power to NLOS power) is displayed in Figure 1.2-17. Notice that the simulation results match the theoretical expression. Moreover, for a specific number of antennas M , Ricean fading yields a higher probability of error compared to Rayleigh fading. Less diversity gains are observed when increasing the number of antennas (less than 1 dB when doubling M). The effect of increasing the power in the Ricean LOS component is illustrated in Figure 1.2-18. Performance degrades with increasing K at low SIR. At high SIR, the dominant LOS component becomes negligible compared to the UWB power, and Ricean fading outperforms Rayleigh fading ($K = 0$).

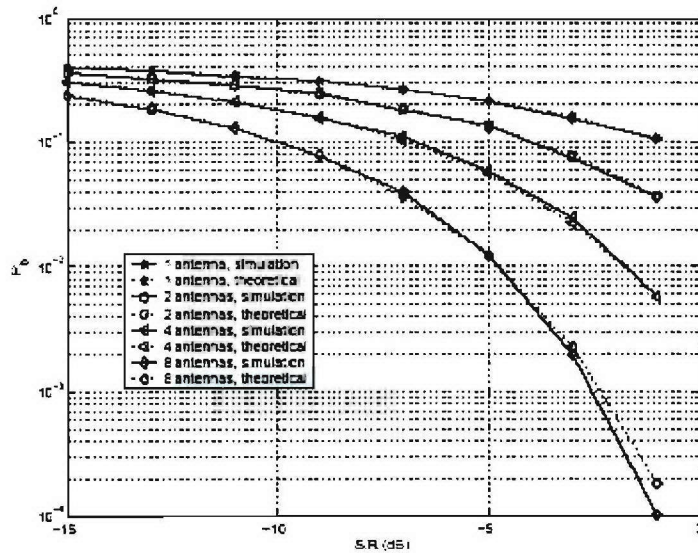


Figure 1.2-16 SD performance under NBI Rayleigh Fading.

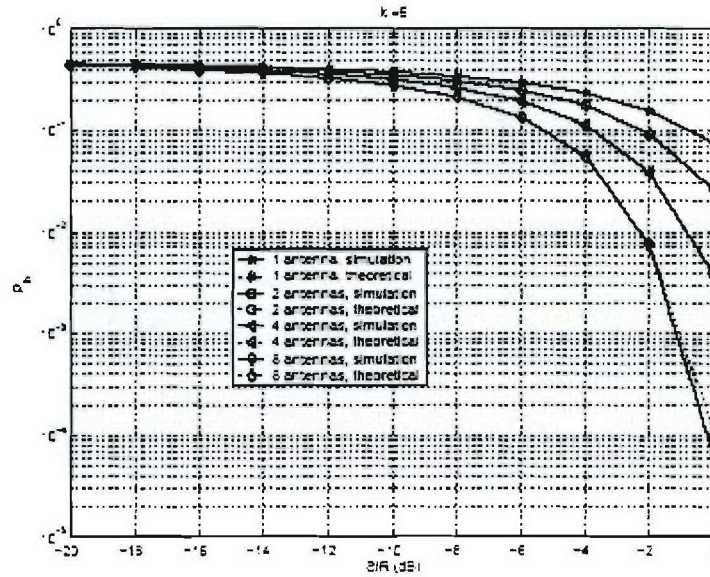


Figure 1.2-17 SD performance under NBI Ricean Fading. $K = 5$.

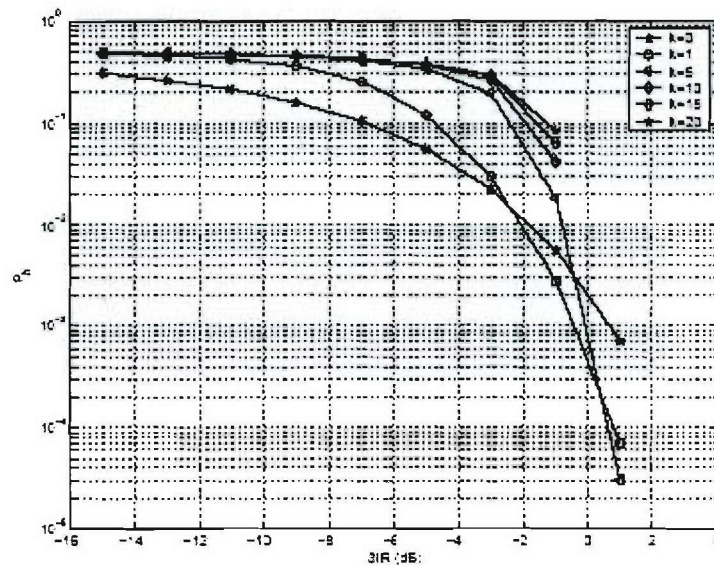


Figure 1.2-18 SD Performance under NBI Ricean Fading for varying K . $M=4$.

Subtask 1.2c Software radio designs for collaborative systems that take advantage of this radio, particularly for interference environments.

Please refer to Task 4.1, TIP #1.

Subtask 1.2d Vector channel models, including Markov Models, and supporting channel measurements.

Task objective: We use discrete channel models for simulating error traces produced by wireless channels. Most of the time, these channels have memory and we use discrete time Markov chains, hidden or semi-hidden Markov models to simulate them. The primary advantage of using these models is easy, rapid experimentation and prototyping.

Efficient estimation of the parameters of a Markov model (including its number of states) is important to reproduce or analyze channel statistics accurately. Although the parameter estimation of a Markov process has been addressed extensively, its order estimation problem has been addressed just recently. In this report, we discuss our preliminary results on the order estimation of Markov chains and survey on existing hidden Markov models order estimation techniques.

Markov Chain Order Estimation

We will focus our attention on binary error sequences, i.e., sequences represented by zeros and ones, in which a binary 1 denotes an error and a 0 denotes no error. Mathematically, an error sequence e_0, e_1, \dots, e_n with order k has conditional probability of an error at the moment n written as

$$\Pr(e_n | e_0, e_1, \dots, e_{n-1}) = \Pr(e_n | e_{n-k}, \dots, e_{n-1})$$

Here the states are defined as k -tuples $S_n = (e_{n-k+1}, e_{n-k+2}, \dots, e_n)$ and the state transition matrix for a k -th order Markov chain has $2^k \times 2^k$ dimensions. In general, the multiple orders Markov chain of order k having n symbols has $n^k \times n^k$ dimensions and in our case of binary sequences $n = 2$.

The states have physical meanings since different basis sequences constitute different set of states. As the order of a Markov chain increases, the basis sequences that constitute these models also increases and this increases the number of states. However, we note that increasing the order of a Markov chain exponentially increases the chain complexity.

In Markov model building we usually use two test criteria namely χ^2 criterion and the information criterion I . If $n(e_1, e_2, \dots, e_{k+1})$ denotes the frequency of transitions of error patterns e_1, e_2, \dots, e_{k+1} and $\hat{p}_{e_1 e_2 \dots e_{k+1}}$ are the corresponding probabilities, then we can write

$$I = \sum_{e_1, e_2, \dots, e_{k+1}} n(e_1, e_2, \dots, e_{k+1}) \ln(\hat{p}_{e_1 e_2 \dots e_{k+1}} / \hat{p}_{e_2 e_3 \dots e_{k+1}})$$

Here I is distributed asymptotically as $0.5 \chi^2$. The χ^2 criterion can be written as

$$\chi^2 = \sum_{e_1, e_2, \dots, e_{k+1}} n^*(e_1, e_2, \dots, e_{k+1}) (\hat{p}_{e_1 e_2 \dots e_{k+1}} - \hat{p}_{e_2 e_3 \dots e_{k+1}})^2 / \hat{p}_{e_2 e_3 \dots e_{k+1}}$$

For large data samples we can replace $n^*(e_1, e_2, \dots, e_{k+1})$ with $n(e_1, e_2, \dots, e_{k+1})$. It is shown in [Turin] that for large data samples, $2I$ and χ^2 criteria are approximately equal.

Given an error sequence, the general steps for finding the optimum order of Markov chain are as follows:

Start with the hypothesis that the sequence is obtained from a binary symmetric channel with no memory. Test this hypothesis against the hypothesis that it is obtained from a first-order Markov chain. If the above hypothesis is rejected then test the hypothesis that the sequence is drawn from a 2nd order Markov chain against the hypothesis that it is drawn from a 1st order Markov chain. Keep testing until the correct order fits the experimental data reasonably well.

For finding the degrees of freedom, we refer to [Turin], [Billingsley] and [Anderson]. According to [Turin] the total number of degrees of freedom is 2^k , where k denotes the order of Markov chains. [Anderson] states that the testing of null hypothesis that a chain is r -th order Markov chain within the hypothesis that it is of t -th order is asymptotically χ^2 with $(2^{t+1} - 2') - (2^{r+1} - 2')$ degrees of freedom.

We should now consider the effect of using a finite length Markov sequence in order estimation. There could be three possible test results that are mentioned below.

Pessimist Test

A test is *pessimist* when the CDF of I is less than the CDF of the theoretical $0.5\chi^2$ plot. As shown in the Figure 1.2-19, if we choose the information criterion to be 3, then the theoretical plot recommends selecting this value with 88% confidence whereas the information criterion gives a confidence level of 82%.

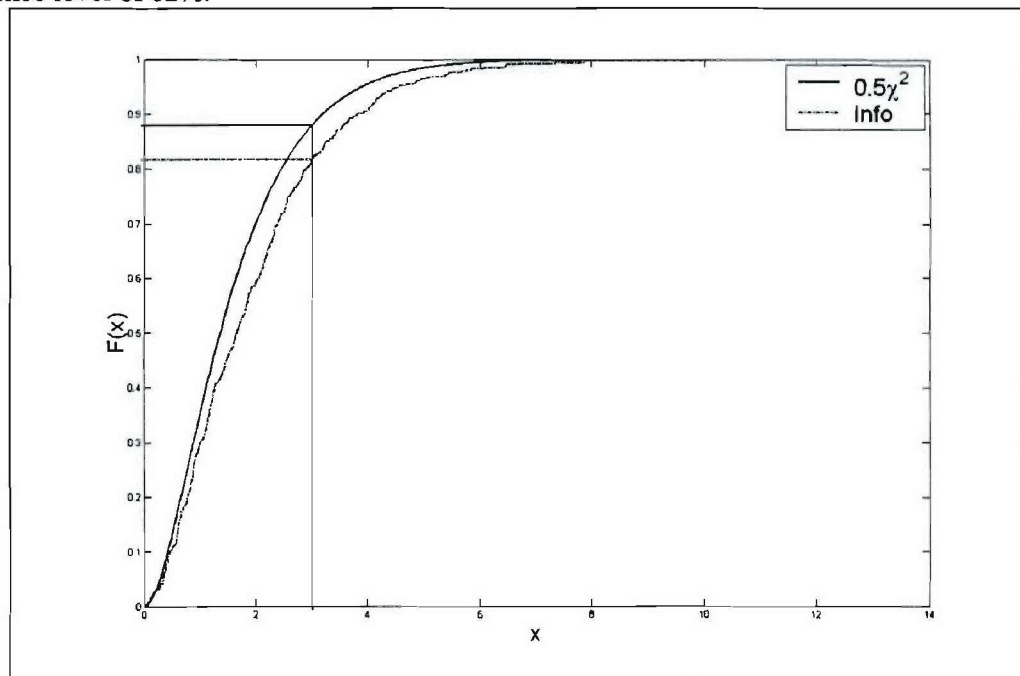


Figure 1.2-19 Pessimist test.

Optimist Test

In an *optimistic* case, the theoretical χ^2 is lower than the information criterion, as shown in Figure 1.2-20. In this case, for an information criterion of 3, the theoretical $0.5\chi^2$ plot recommends us to choose a confidence level of around 77%, whereas from the information criterion we get around 82% confidence on our test.

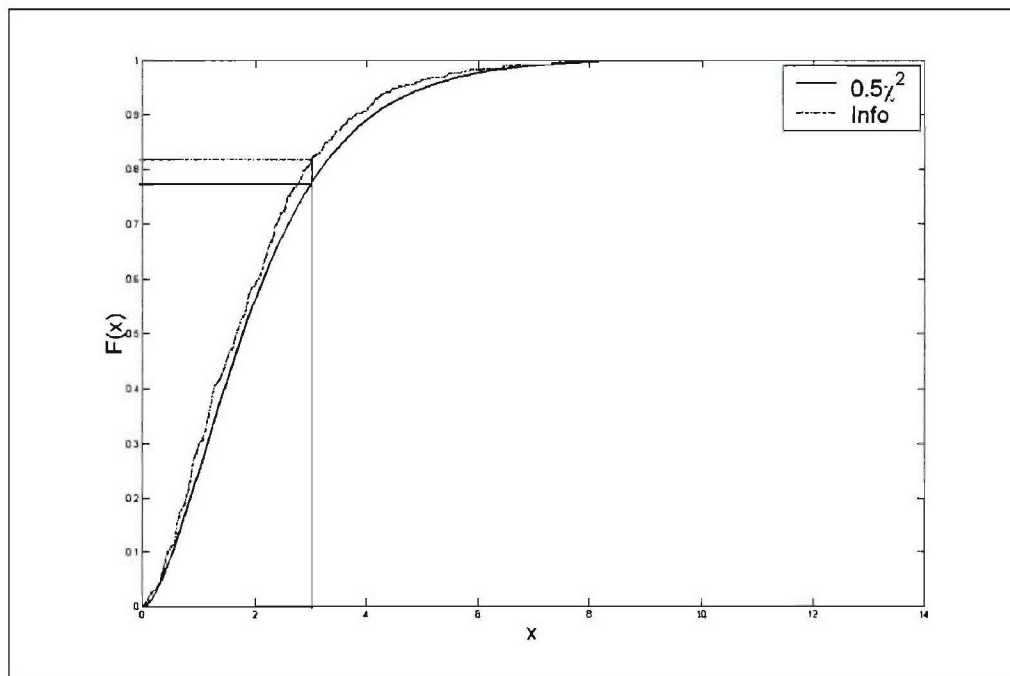


Figure 1.2-20 Optimist test.

True Test

In a *true* test, there is no difference in the CDFs of I and $0.5\chi^2$ plot as shown in Figure 1.2-21.

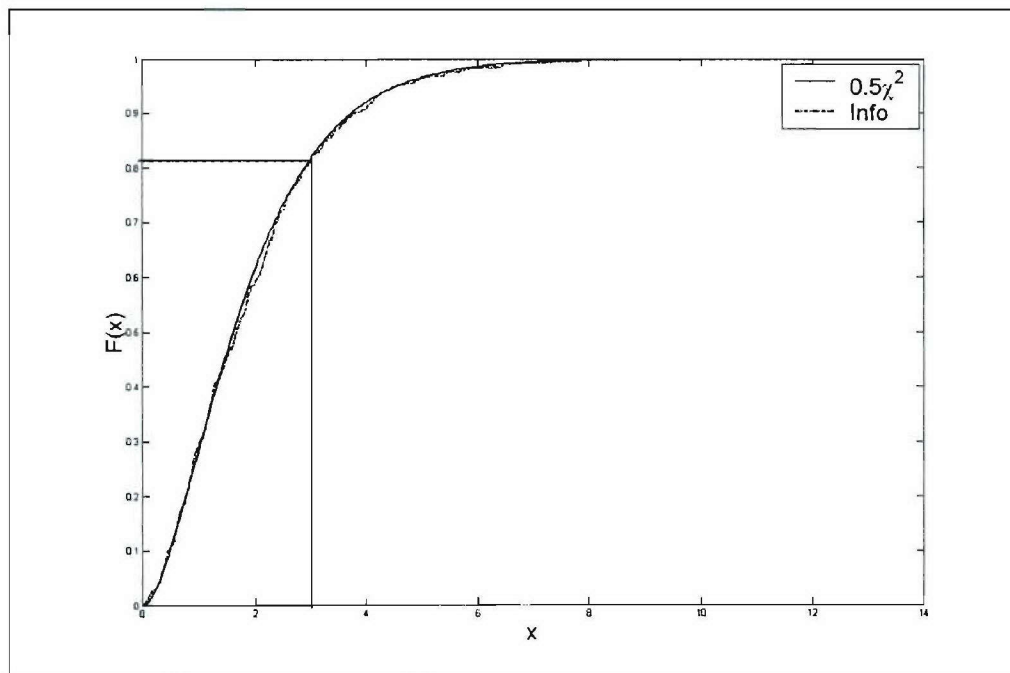


Figure 1.2-21 True test.

We now apply the tests to three different cases.

Case 1- Zero-Order Markov Chain

We perform order estimation test on a binary memoryless chain with the BER of 0.1. Figure 1.2-22 5 shows CDFs of different test statistics. The first plot shows the test result to be optimistic. However in all the cases, we found out that information criteria are very close to the theoretical χ^2 plots. Hence we reject these hypotheses and conclude that the given sequence is a binary symmetric channel with no memory.

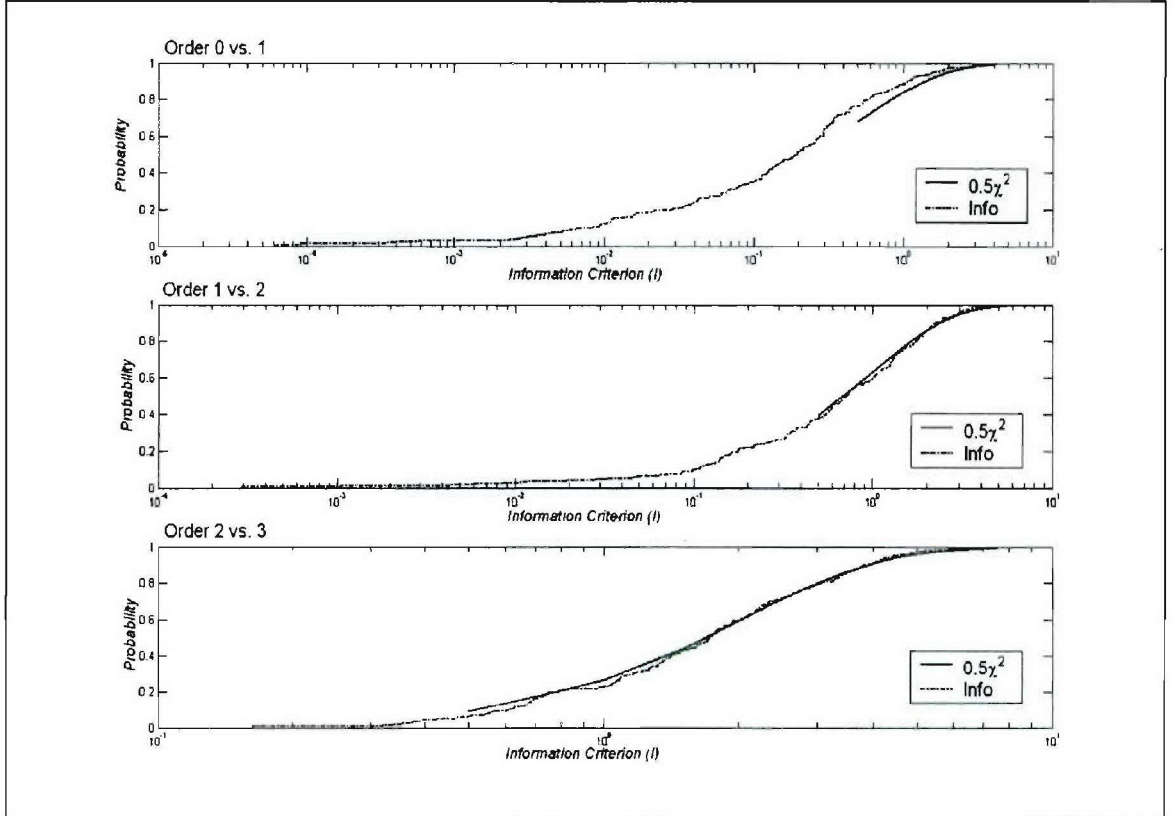


Figure 1.2-22 Order estimation (memoryless chain).

Case 2 – First-Order Markov Chain

A first-order Markov chain can be written as

$$\Pr(e_n | e_0, e_1, \dots, e_{n-1}) = \Pr(e_n | e_{n-1})$$

The state transition matrix takes the form

$$\mathbf{P} = \begin{bmatrix} \Pr(0 | 0) & \Pr(1 | 0) \\ \Pr(0 | 1) & \Pr(1 | 1) \end{bmatrix}$$

We next generate error sequences based on the following state transition matrix

$$\mathbf{P} = \begin{bmatrix} 0.90 & 0.10 \\ 0.73 & 0.27 \end{bmatrix}$$

The length of error sequences that are generated for these tests is 100,000 bits and the tests are performed 1000 times to get the statistics information criteria. The first test, order 0 vs. 1,

determines that the information criterion is not close to the theoretical $0.5\chi^2$ CDF. However for order 1 vs. order 2 and order 2 vs. order 3, we find I to be distributed as $0.5\chi^2$. Hence we choose the order of the Markov chain to be 1.

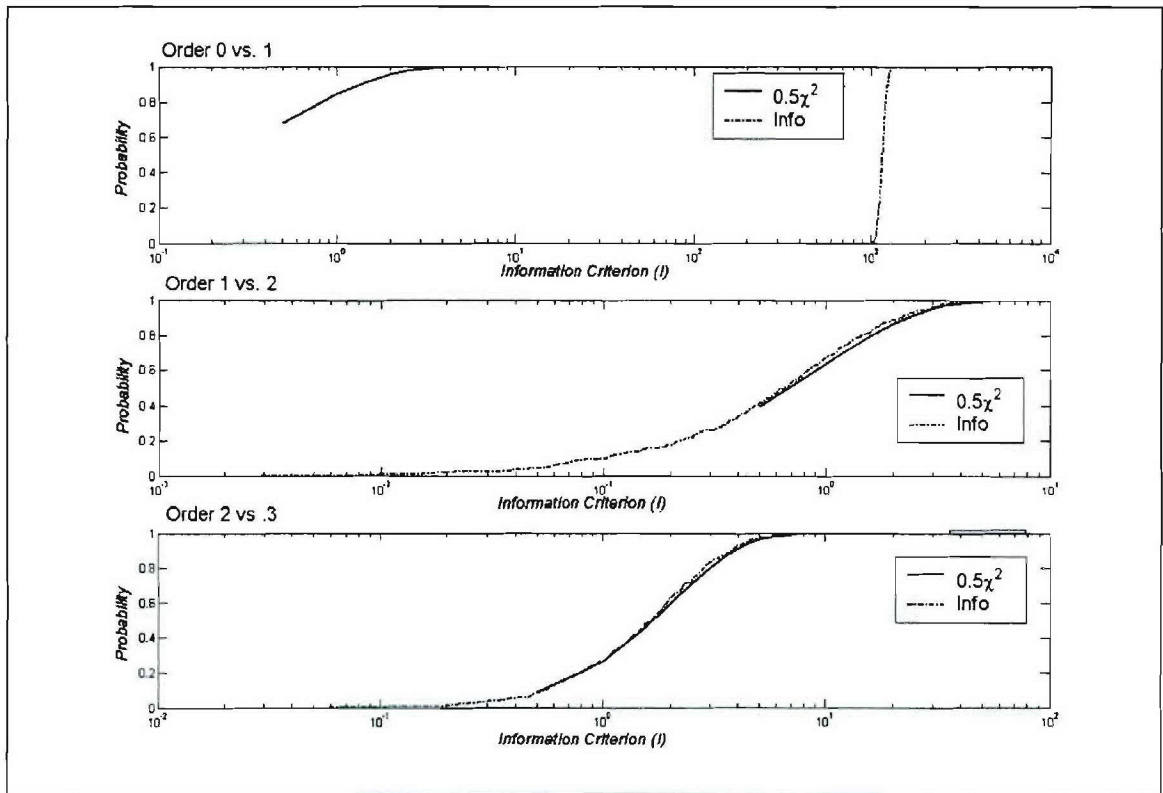


Figure 1.2-23 Markov chain order estimation (true order is 1).

Case 2 – Second-Order Markov Chain

Let us now consider order estimation of a second-order Markov chain with transition matrix having the form

$$\mathbf{P} = \begin{bmatrix} \Pr(0|0,0) & 0 & \Pr(1|0,0) & 0 \\ \Pr(0|1,0) & 0 & \Pr(1|1,0) & 0 \\ 0 & \Pr(0|0,1) & 0 & \Pr(1|0,1) \\ 0 & \Pr(0|1,1) & 0 & \Pr(1|1,1) \end{bmatrix}$$

We consider the following state transition matrix

$$\mathbf{P} = \begin{bmatrix} 0.90 & 0 & 0.10 & 0 \\ 0.60 & 0 & 0.40 & 0 \\ 0 & 0.95 & 0 & 0.05 \\ 0 & 0.70 & 0 & 0.30 \end{bmatrix}$$

Figure 1.2-24 shows that first two information criteria are greater than the theoretical χ^2 plots whereas in the third plot, (test for order 2 vs. order 3), I is found to be distributed as $0.5\chi^2$. Hence from the plots we infer that the Markov chain is of order 2.

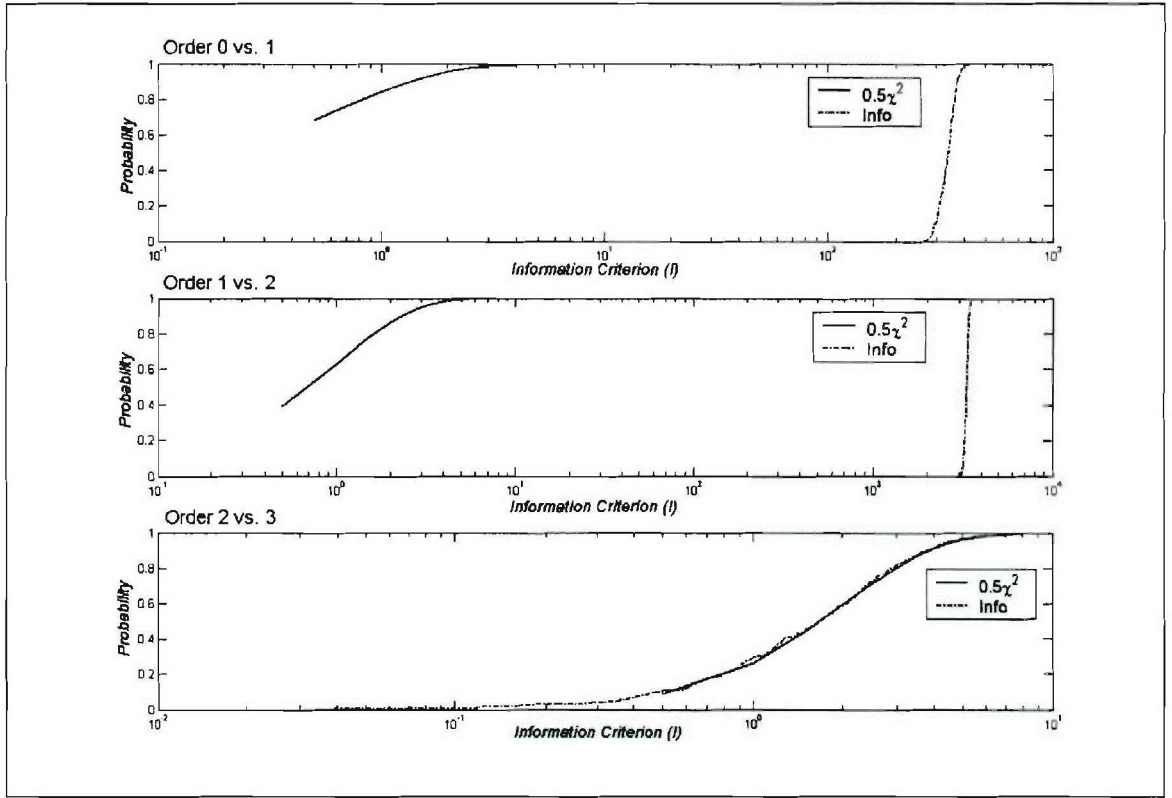


Figure 1.2-24 Markov chain order estimation (true order is 2).

Case 3 – Third-Order Markov Chain

The third-order Markov chain state transition matrix for error sequences is an extension of the second order Markov chain given in [Turin]. The state transition matrix takes the form

$$P = \begin{bmatrix} \Pr(0|0,0,0) & 0 & 0 & 0 & \Pr(1|0,0,0) & 0 & 0 & 0 \\ \Pr(0|1,0,0) & 0 & 0 & 0 & \Pr(1|1,0,0) & 0 & 0 & 0 \\ 0 & \Pr(0|0,1,0) & 0 & 0 & 0 & \Pr(1|0,1,0) & 0 & 0 \\ 0 & \Pr(0|1,1,0) & 0 & 0 & 0 & \Pr(1|1,1,0) & 0 & 0 \\ 0 & 0 & \Pr(0|0,0,1) & 0 & 0 & 0 & \Pr(1|0,0,1) & 0 \\ 0 & 0 & \Pr(0|1,0,1) & 0 & 0 & 0 & \Pr(1|1,0,1) & 0 \\ 0 & 0 & 0 & \Pr(0|0,1,1) & 0 & 0 & 0 & \Pr(1|0,1,1) \\ 0 & 0 & 0 & \Pr(0|1,1,1) & 0 & 0 & 0 & \Pr(1|1,1,1) \end{bmatrix}$$

We generate Markov sequences according to the following state transition matrix

$$P = \begin{bmatrix} 0.9000 & 0 & 0 & 0 & 0.1000 & 0 & 0 & 0 \\ 0.6000 & 0 & 0 & 0 & 0.4000 & 0 & 0 & 0 \\ 0 & 0.7800 & 0 & 0 & 0 & 0.2200 & 0 & 0 \\ 0 & 0.9900 & 0 & 0 & 0 & 0.0100 & 0 & 0 \\ 0 & 0 & 0.8500 & 0 & 0 & 0 & 0.1500 & 0 \\ 0 & 0 & 0.8000 & 0 & 0 & 0 & 0.2000 & 0 \\ 0 & 0 & 0 & 0.7500 & 0 & 0 & 0 & 0.2500 \\ 0 & 0 & 0 & 0.5500 & 0 & 0 & 0 & 0.4500 \end{bmatrix}$$

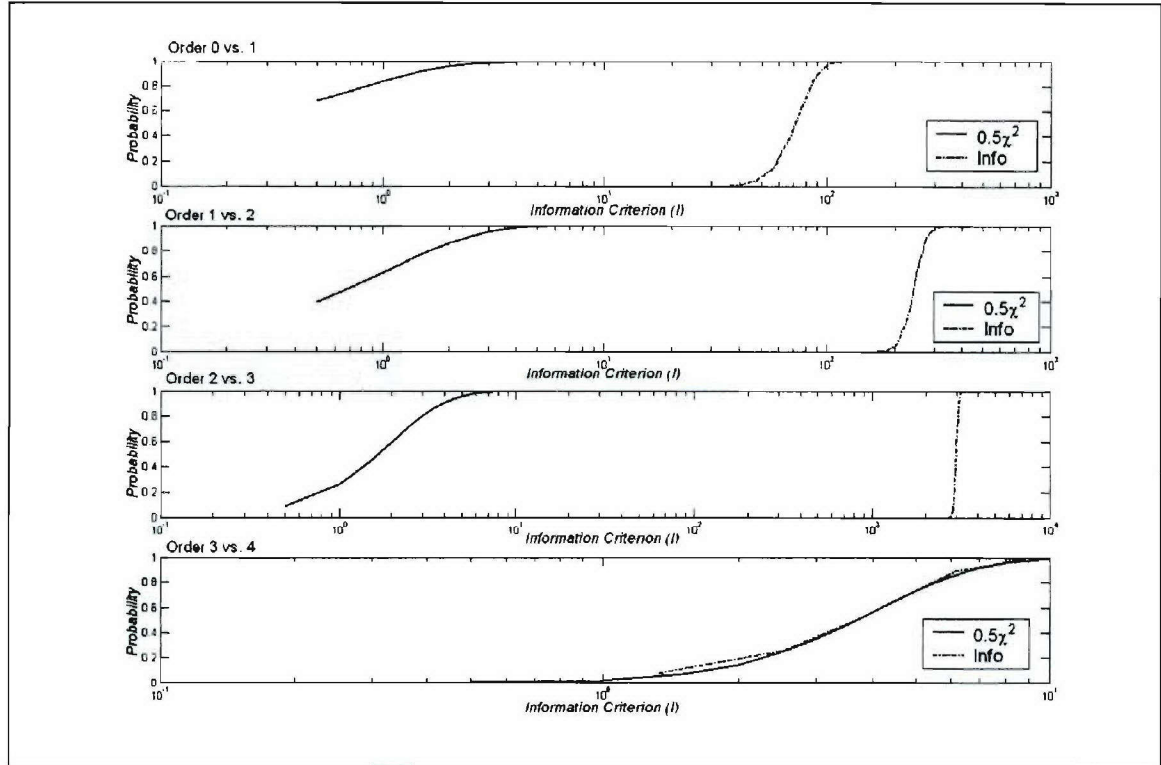


Figure 1.2-25 Markov chain order estimation (true order is 3).

Figure 1.2-25 shows that the information criteria in all three tests are greater than the corresponding theoretical χ^2 plots.

We infer from the tests performed above that the information criterion remains greater than the theoretical χ^2 plots till the optimum order is estimated. After estimating the correct order, the information criterion I is found to be $0.5\chi^2$ distributed.

We have shown how to estimate the correct order of a Markov chain before fitting Markov models to experimental data. We hope that using these tests before applying Markov models to the experimental data will help us in getting more accurate models. Now we will move forward and study the consistency and efficiency of Markov chain order estimator.

Hidden Markov Process Order Estimation

According to [MacDonald], “in the case of HMM, the problem of model selection (and in particular the choice of the number of states in the Markov chain component model) has yet to be satisfactorily solved.”

We test different order HMMs on Ultra-Wideband (UWB) channel statistics which were based on channel measurements performed at MPRG. These error statistics are then used as training sequences to train different HMMs.

We use a 2-state, 10-state and 15-state HMMs and evaluate the performance of these models in terms of bit error probability and frequency of error-free runs.

Table 1.2-1

	Length 1	Length 2	Length 3	Length 4	Length 5
Original sequence	9123	1085	112	12	1
2 state HMM	9123	1067	136	15	3
10 state HMM	8801	1144	150	24	1
15 state HMM	8904	1174	153	24	3

Model parameters including the state transition matrix, the output symbol probability matrix and the initial state probability vector are obtained by using Baum-Welch algorithm [Turin] with random initial parameters. Error traces are regenerated and then compared with the original error statistics. From Table 1.2-1, we can observe some performance degradation as we increase the number of states of hidden Markov models. The 2-state HMM seems to be the closest match with this particular UWB error trace.

Let us now give a brief introduction to the theory of order estimation for HMMs. The problem of order estimation of Markov processes deals with the compensation of the likelihood function. A penalty term is added to the maximum likelihood and the resulting compensated likelihood is maximized. The general form of an order estimator is as follows [Gassiat]

$$r_n := \arg \max_r \left[\sup_{P \in M^r} \log P(y_1^n) - \text{pen}(n, r) \right]$$

Proper choice of the penalty term allows the strongly consistent estimation of the structural parameter

For the case of a Markov chain, the order estimation problem is easier. Finesso uses the Law of Iterated Logarithm (LIL) to get an estimate on the order of a Markov chain [Finesso]. Since such knowledge is not available from LIL for the case of HMMs and we rely on universal coding when dealing with Markov models with hidden state space. The universal code maps the integers (representing messages) onto prefix-free (sometimes called self-delimiting or instantaneously decodable) binary codes. These codes do not require the receiver or the transmitter to know the maximum integer (number of potential messages) ahead of time. These codes include unary coding, Fibonacci coding and Rice coding etc. [Elias]. The use of universal coding arises when we need to understand the behavior of

$$\sup_{P \in M^r} \log P(y_1^n) - \sup_{P \in M^0} \log P(y_1^n)$$

We give a survey of HMM order estimators and explain our future contribution in this area. An excellent survey of these estimators is provided in [Cappé] and [Gassiat] and we borrow some important results from there.

Different HMM order estimators are used mainly relying on the theory of universal source coding, among which the Bayesian Information Criterion (BIC), Minimum Description Length (MDL) and Penalized Maximum Likelihood (PML) [Gassiat] are the most popular. All these order estimators are related to generalized likelihood ratio testing. To prove their consistency, we need Asymptotic Equipartition Principles (AEP) or Shannon-McMillan-Breiman theorem. Most of the order estimators satisfy a generalized Neyman-Pearson criterion of optimality. Specifically, the optimal error estimator minimizes the probability of underestimation among all estimators whose probability of overestimation lies below a specific value.

Another main topic of HMM order estimation is the study of *error exponents* for different estimators. Error exponent or Bahadur efficiency [Gassiat] has proved to be a relevant measure of asymptotic relative efficiency. It is the best rate of exponential decay of the probability of underestimation among all estimators whose probability of overestimation is uniformly bounded away from unity over the entire range of (unknown) measures that could generate the observations.

Semi-Hidden Markov Models Order Estimation

The order estimation problem of semi-hidden Markov models was studied recently by Khundapur and Narayan in [Khundapur]. They consider a SHMM order estimator based on renewal type, which was introduced in [Csiszar].

Given a binary sequence y_1^n , $n \geq 1$, the n 's for which $y_1^n = 1$ constitute renewal epoch, and one plus the number of intervening 0's between successive 1's corresponds to a renewal times. Let

$$N = N(y_1^n) = \sum_{i=1}^n y_i$$

denote the number of renewal in y_1^n . Let $\gamma_j = \gamma_j(y_1^n)$, $0 \leq j \leq N$, be the renewal epoch in y_1^n , where we assume $\gamma_0 = 0$ corresponding to $N = 0$. For $z_n = z_n(y_1^n)$, $1 \leq j \leq N$, be the renewal times of the realization y_1^n .

The renewal type of a binary sequence $y_1^n \in \{0,1\}^n$, $n \geq 1$, with $N \geq 1$, denoted by $K(y_1^n) = (k_1, k_2, \dots, k_n)$, is an n -tuple of non-negative integers defined by

$$k_m = k_m(y_1^n) = \sum_{j=1}^N I(z_j = m) \quad 1 \leq m \leq n$$

where $I(\cdot)$ is the indicator function. Note that $\sum_{m=1}^n k_m = N$.

It is shown that this estimator is strongly consistent with the probability of underestimation of the true order decays exponentially in the number of observations while the probability of overestimation goes to zero significantly fast. The estimator is shown to achieve best error exponent in a large class of estimators.

Our interest in semi-hidden Markov model is natural because of the structure of error patterns in wireless channels. The error patterns have long stretches of zeros (no errors) usually followed by small bursts of ones (errors) with some zeros, distributed according to some distribution, in them. A general HMM takes significant time to model/generate these observation sequences. With SHMM we can develop runlength codes from binary sequences and estimate the parameters of the model using parameter estimation technique similar to traditional BWA [Akbar]. This can be done with higher accuracy if the order of the hidden states could be known through some order estimation technique. We will investigate the order estimators presented by [Khundapur] in this setting.

References

- I. Akbar, Markov Modeling of Third Generation Wireless Channels, M.S. Thesis, Virginia Tech, 2003.
- T. W. Anderson and L. A. Goodman, "Statistical inference about Markov chains," *Ann. Math. Statist.*, vol. 28, 1957, pp. 89-110.
- P. Billingsley, "Statistical methods in Markov chains," *Ann. Math. Statist.*, vol. 32, 1961, pp. 12-40.
- Oliver Cappé, Eric Moulines & Tobias Rydén, *Inference in Hidden Markov Models*, Springer, 2005.
- P. Elias, "Universal codeword sets and representations of integers," *IEEE Trans. Inform. Theory*, vol. 21, no. 2, 1975, pp. 194-203.
- W. Feller, *Introduction to Probability Theory and Its Applications*, Volume 1, 1950, John Wiley & Sons, Inc.
- L. Finesso, Consistent Estimation of the Order for Markov and Hidden Markov Models, Ph.D. Dissertation, 1990, University of Maryland.
- E. Gassiat & S. Boucheron, "Optimal error exponent in hidden Markov models order estimation," *IEEE Trans. Inform. Theory*, 49, 2003, 964-980.
- S. Khundapur & P. Narayan, "Order Estimation of Hidden Markov Sources and Binary Renewal Processes," *IEEE Trans. Inform. Theory*, 48, 2002, pp. 1704-1713.
- W. Turin, *Digital Transmission Systems: Performance Analysis and Modeling*, 1998, McGraw-Hill.

Subtask 1.2e Software radio integration into the AWINN demonstrations

Task objective: The goal of this subtask is to integrate the software radio developed in Subtask 1.2a into AWINN activities. To achieve this objective, the software radio is being designed with two distinct modes of operation: a communication mode and a data capture mode. The communication mode is currently optimized for impulse UWB signals, however, it is capable of operating using any broadband communication technique (such as DSSS or OFDM). The only limitations on the types of signals that the receiver can handle are: (1) the 2.2 GHz analog input

bandwidth limitation of the MAX104 ADCs, (2) the 8 GHz effective receiver sampling frequency, and (3) the processing power of the FPGA.

In the data capture mode, the receiver will simply capture ADC samples and store them in the FPGAs RAM memory. The data can then be processed in non-real time using one of the FPGAs PowerPC processors, or the sample values can be transmitted to a host computer via the USB interface. The number of samples that can be captured is limited by the amount of high-speed RAM memory that can be allocated, but is currently estimated to be around 256,000-512,000 samples—corresponding to about 32-64 μ sec of captured data. A trigger signal input allows the receiver to estimate the time of arrival of received samples for ranging, and the ability to synchronize multiple receivers to a common clock signal allows for precise position location.

Accomplishments during reporting period: Several provisions for integrating the software radio into the AWINN activities have been included in the design of both the prototype and full receiver. To facilitate synchronization of several receivers, the clock distribution network was modified to allow for several receivers to be synchronized to a single clock source. A trigger signal input allows the receiver to operate in the data capture mode and measure the time of arrival for UWB pulses. A trigger output allows the FPGA to control an external UWB pulse generator, to facilitate evaluation of the communication system, ranging, and position location algorithms. Finally, FPGA code for the data capture mode is under development and will be implemented on the prototype receiver board.

Schedule:

- August/September 2005 – Evaluate Prototype Receiver
 - Verify the Receiver Operates in All Modes
 - Verify FPGA Code for Data Capture as well as PowerPC Processing
- October-December 2005 – Refine FPGA/PowerPC code for ranging and/or position location
 - Support Code Development with Measurements either from Lab Equipment or the Prototype Receiver
- Spring 2006 – Integrate Full Receiver into AWINN Activities
 - Crane Demonstration
 - Position Location
 - Imaging
 - Channel Measurements

Personnel:

Chris R. Anderson – Transmitter and Receiver Hardware Development
Deepak Agarwal – Receiver FPGA Code Development

Subtask 1.2f UWB applications to technology development applicable to Sea-Basing: position location, ranging, and imaging.

Please refer to Task 4.2, TIP #2

1.2.3 Importance/Relevance

The simulation results from the SDR testbed simulations demonstrate that the time-interleaved sampling approach is a viable hardware architecture. The use of TI-Sampling with digital demodulation provides a tremendous amount of flexibility in the receiver operation. Even though

the receiver is optimized for impulse UWB communication, it should be capable of using almost any broadband communication scheme.

The UWB SDR algorithm design is investigating ways of improving signal acquisition and tracking, as well as operation in multipath environments. Ship-based environment tend to generate a large number of multipath signals and represent a tremendous amount of energy available for the receiver to capture. Using a pilot-based matched filter topology, the receiver can capture a large percentage of the available energy without resorting to the complex tracking algorithms required by Rake receivers.

The distributed MIMO architecture investigated in this task will allow a number of UAVs to coordinate their transmissions and take advantage of space-time coding performance gains. These performance gains are available even if the various UAVs are not perfectly synchronized—an important consideration if the transmission involves a UWB signal. Combining UWB with distributed MIMO, we believe that long-range transmissions should be possible while still maintaining the LPI properties of UWB signals.

Finally, UWB signals have been demonstrated to have precision ranging and position location properties. Combining 3D ranging information with the crane control system should allow for sea-based ship-ship cargo transfer. Additionally, the position location abilities of UWB will allow for inventory control and tracking, as well as the precision maneuvering required to establish the ship-ship cargo transfer.

Students supported

Chris R. Anderson, Jan. 15, 2005 – present
Jihad Ibrahim, Jan. 15, 2005 – present
Swaroop Venkatesh, Jan. 15, 2005 – present
Maruf Mohammad, Jan. 15, 2005 – present

Faculty supported

Jeffrey H. Reed, Jan. 15, 2005 – present
R. Michael Buehrer, Jan. 15, 2005 – present
William H. Tranter, Jan. 15, 2005 – present

1.3 Task 1.3 Collaborative and Secure Wireless Communications

1.3.1 Overview

The Task 1.3 research team was given the duty of deriving an approach to allow independent mobile transceivers to work collaboratively to improve communications link dynamics for far-field exchanges. By doing so, this approach will improve communication range, improve communication quality, reduce power consumption, and/or reduce sensor weight. The proposed solution will utilize the spatial distribution of the sensor network by creating a large virtual antenna. The team will utilize beamforming techniques to accomplish this; however, the proposed approach differs from contemporary approaches in two ways. First, traditional approaches rely on having a set of antennas that have a fixed spatial relationship, located along a geometric shape such as a line, circle, or other form. Here, the antennas are on mobile transceivers (1 per device), and their position relative to the other mobile nodes and the base station change over time. Second, traditional approaches rely on having either a single transceiver or a set of transceivers that are tightly coupled. Mobile transceivers are independent and can only coordinate spatial and temporal information with each other wirelessly. Beamforming using mobile transceivers will thus require an entirely new approach.

Organization: This task is managed by Directors of Virginia Tech Configurable Computing Lab using the following personnel:

Peter Athanas, Co-Director
Mark Jones, Co-Director
Deepak Agarwal, MSEE (graduated)
Brian Marshall, MSEE (graduated)
Todd Flemming, PhD student
Tingting Meng, PhD student
Yousef Islander, PhD student
James Webb, MSEE student
Matthew Blanton, MSEE student
Marc Somers, MSEE student
Lael Matthews, MSEE student

1.3.2 Task Activity Summary

Effort this quarter was primarily directed towards Task 1.3a and Task 1.3b. This section summarizes the activities on these two tasks over the past quarter.

1.3.2.1 Collaborative Communications Methods

In this task, the team is investigating a method of improving the communication link performance between a (mobile) base station and a spatially distributed, and possibly mobile, sensor network. The team will exploit the collective behavior of the sensor network to solve specific communications problems collaboratively. A new technique for querying distant mobile sensor networks is being investigated. In doing so, multiple mobile stations work together to send a shared message to the querying base-station. There are important advantages to this approach:

- The power requirements for a single mobile are small since the burden of transmission is shared among all nodes.
- Due to the nature of directed energy, the overall system has low detectability (or for security, low interference).
- The system is highly fault-tolerant, and does not rely on the operation of any given node.

There are several key problems that are the central focus of this task:

- **Phase Synchronization:** At the base-station receiver end, all of the transmitted signals from the individual sensor nodes must be combined to form one higher power signal. To do this, the individual nodes must phase their transmissions accordingly. Assuring that all the component signals combine positively at the receiver is a challenging task, especially when the mobile stations are in different directions and using high frequency signals.
- **Time Synchronization:** A coarser grain of time synchronization is required so that each of the mobile nodes commences their message transmission at the same time.
- **Spatial Synchronization:** Each of the nodes must know their (relative) spatial position in order to compute the necessary phase offset.

It is assumed in this problem that the sensor network is relatively far away from the querying base-station. An analogous scenario is that the sensor network consists of a cluster of buoys monitoring a distant region of a sea. The team examined several potential algorithms that combine transmission power from multiple independent and mobile transceivers. Such a scheme would be fair in distributing the power drain of far-field communications to all nodes. A high-level radio-centric view of the system is depicted in Figure 1.3-1. This section covers the three leading approaches that the team has focused on this past quarter. The remainder of this section presents these alternatives.

Multiple Transmitter Single Receiver Beam Forming

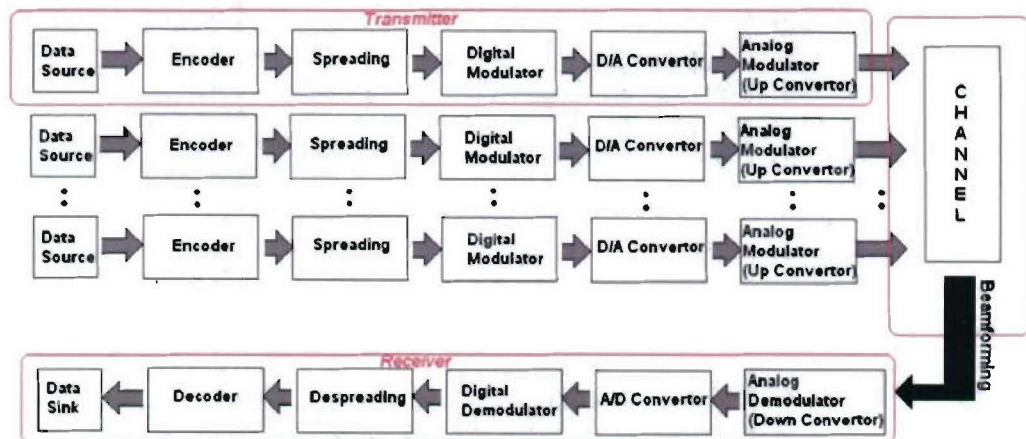


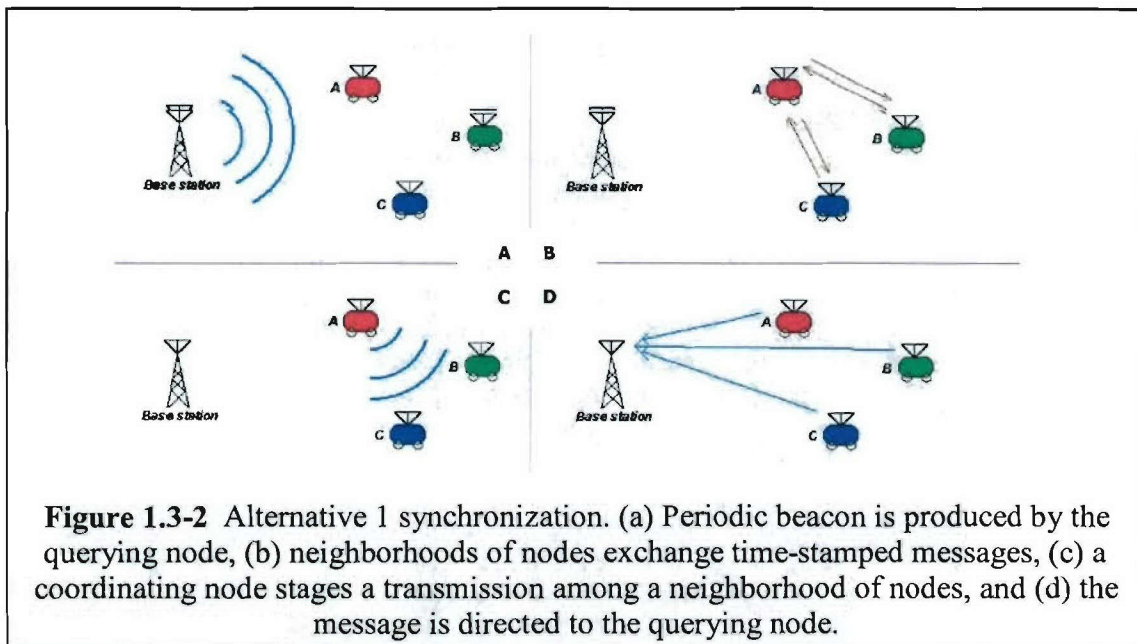
Figure 1.3-1 Conceptual MISO sensor-network query model where multiple mobile transmitters are combined at a single base station.

Alternative 1: Tagged Messages

In this first alternative, the base station broadcasts periodic synchronization packets to the nodes and the nodes record the arrival times of these packets (Figure 1.3-2a). In this case, it is assumed that a node (the "originating" node, labeled as "A") needs to send a message to the base station. This node first exchanges packets with other nearby nodes (Figure 1.3-2b). This allows "A" to get the synchronization packet arrival time at every other node. It also allows "A" to calculate the offset between its local time and every other node's local time. "A" uses this information to calculate when each node should start transmitting the message to the base station. The node then broadcasts the message to the other nodes along with the start times (Figure 1.3-2c). Each node then transmits the message at its assigned time and the transmissions converge at the base station (Figure 1.3-2d).

In this alternative, every packet is a synchronization point. A transceiver schedules packet transmission so that the synchronization point is transmitted at a certain time according to the transceiver's local time. Likewise, a transceiver measures the arrival time of a packet's synchronization point using local time. For brevity, a packet's synchronization point transmission time is called the packet transmission time. Likewise, a packet's synchronization point arrival time is called the packet arrival time.

The base station broadcasts periodic synchronization packets to the nodes and the nodes record the arrival times of these packets. A node (the "originating" node, "A") needs to send a message to the base station. This node exchanges packets with other nearby nodes. This allows "A" to get the synchronization packet arrival time at every other node. It also allows A to calculate the offset between its local time and every other node's local time. "A" uses this information to calculate when each node should start transmitting the message to the base station. It broadcasts the message to the other nodes along with the start times. Each node then transmits the message at its assigned time and the transmissions converge at the base station.



Alternative 2: Progressive Alignment

In this alternative, an iterative method is used to synchronize a group of remote nodes to a common time base. There are a number of ways to approach this with different degrees of complexity and rates-of-convergence. One simple method is depicted in Figure 1.3-3. Here, when a message needs to be conveyed to the base-station, the nodes send a sequence of phase-offset carrier bursts. The sequence of phase offsets used by each node are determined by individual "phase wheels". The base station then sends out a short message indicating the time slot where received power is at a maximum. This data are sufficient for each node to determine its proper phase offset for maximum beam gain. The nodes then convey their message to the base-station in unison, using the proper phase offsets.

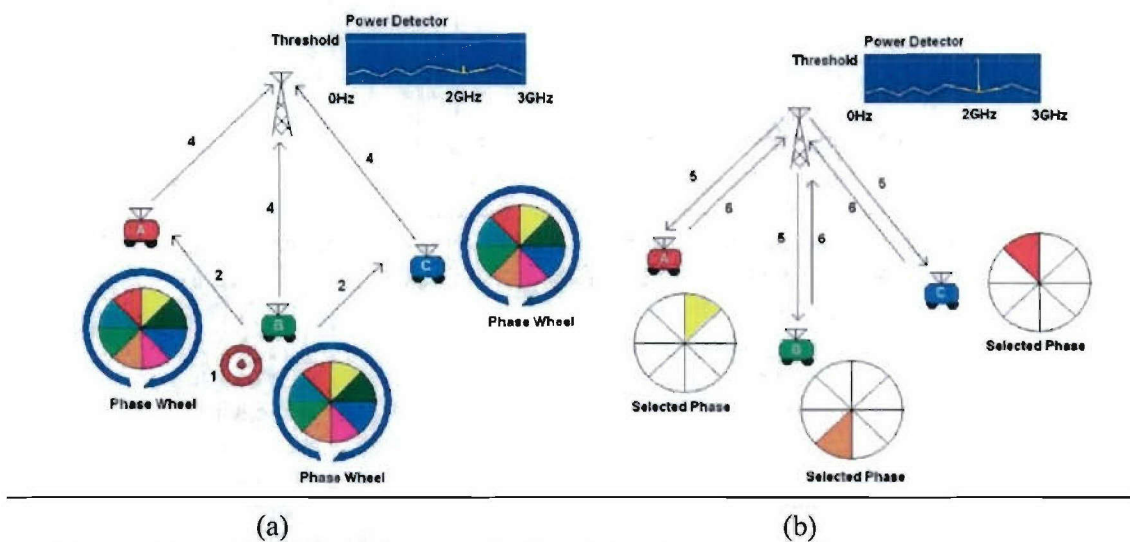


Figure 1.3-3 Alternative 2 synchronization. (a) nodes sequence through a sequence of known phase offsets, (b) nodes are informed of peak power time frame indicating alignment, which then send their shared message.

It should be noted that due to oscillator drift, oscillator precision, and a host of other factors, once synchronization is achieved the nodes will loose synchronization in a very short time.

Alternative 3: Beacon Synchronization

The transceivers for this alternative have the same requirements as the ones for Alternative 1. In addition, each node must know its spatial position (relative to other nodes, and or to the base-station) to within 1/10 of the carrier frequency's wavelength.

Here, the base station broadcasts n periodic synchronization packets at times t_0, t_1, \dots, t_{n-1} , where the times are regularly spaced. The base station is silent for m periods, after which it repeats the process. The nodes record the arrival times of these packets. A node (the "originating" node, "O") needs to send a message to the base station. This node broadcasts its message to the other nodes. Each node schedules its transmission time so that its packet will arrive at the base station at time t_{n+m-1} . The transmissions thus converge at the base station.

Both Alternative 1 and Alternative 3 depend on precisely measuring packet arrival times. Likewise, these alternatives need to precisely schedule packet transmission times. The obvious approach is to directly synthesize the modulated signal in digital logic and send it through a digital-to-analog converter with fine-grain phase adjustments. The team is considering alternative approaches to measure time that may not need high sample rates.

Alternative 3 depends on precise knowledge of the distance from the base station to every node. Alternative 1 does not rely on any distance knowledge; it is entirely based on time. Both algorithms have a significant portion that can be implemented in software; the complexity difference between these two alternatives is in the software portion.

1.3.2.2 Determining Position (for prototyping)

The purpose of this subtask is to develop a behavioral program using current robotics software to accurately estimate a robot's position to within 1.5 cm. Position is relative to an arbitrary location in a test room to which all participating robots orient themselves and operate on the same x, y plane. This task can be extended to determine the relative position from a base station by creating an offset to the relative map's origin. The same technique can also be applied to determine absolute position on the earth's surface. Position accuracy is required in the AWINN project to correctly transmit data from individual point sources (robots) to a base station. A basic premise for this project is that each robot does not have enough power on its own for the signal to reach the base station. However, when multiple robots send timed signals with the same wavelength and phase, the signals will combine coherently providing a signal strong enough to reach the base

station. To achieve the proper phase, the wavelength alignment of each robot's signal cannot be off by more than 10 percent. To ensure that the phase and timing of each robot's transmitted signal combines to form an amplified beam, the position of each robot must be determined within 1.5 cm.

The platforms for demonstrating the practicality of the AWINN project are robots running the ERSP 3.0 robotic development software. The basic structure for the software for their operation is a wander-and/or-explore pattern that directs each robot around its environment while avoiding obstacles and creating an internal map so it can analyze its position and make corrections to its location as the map becomes increasingly more accurate.

The most difficult part of this task is adapting the capabilities of the robotics software to the specifications. The current software uses wheel odometry and visual landmarks to create a map and estimate position on an internal x, y grid. The wheel odometry provides a coarse estimate of position by decoding the ticks of a stepper motor and translating it into distance. Unfortunately, this estimate continually diverges from the actual position due to wheel slippage. To correct its position the software takes images from a camera and establishes any object with significant distinguishable features as a landmark. By noting its position at the time the landmark is identified, it now has a reference to compare with its odometry data. As the robot continues to explore its environment, it is able to make adjustments to these landmarks by referencing them to other landmarks as well as to its odometry data, thus continually making improvements to the internal map. Once the robot has established an accurate map, its estimated position should be fairly accurate.

Problems arise due to our current camera and software. Potential landmarks are frequently undetected by the camera and the robot is unable to create an accurate map of its surroundings. Without the map position data becomes unreliable and cannot be corrected. On a larger scale, the difficulties expand meaning that in a larger open space the robot will not have access to any landmarks and be susceptible to the errors induced from wheel odometry. They also do not have the capability of determining distances from objects outside of their localized map unless an offset is introduced into their position logic. Difficulties can also arise in ensuring all participating robots operate on the same x, y plane. Despite the fact that each individual robot can be loaded with the same map reference, the initial position estimate of each robot is generated from its own wheel odometry and is relative to the point at which it initializes its sensors and begins to explore its environment. Therefore, it will be necessary for all participating robots to orient themselves on the loaded map before attempting to transmit any data to the base station.

The major accomplishments this quarter on this portion of the project mostly revolve around determining the problems. Testing the accuracy of the wheel odometry and ability of the camera to detect good visual landmarks has been a primary focus. Experiments conducted thus far indicate that a robot's wheel odometry tends to diverge an average of 10 cm after traveling only 10 feet on a hard surface. On a soft surface (carpet) the divergence is closer to 15 cm after the same distance. On average, if no visual landmark corrections are executed, the divergence is about 4.2 cm/m, which can cause some severe problems if wavelength timing depends on robot position.

Visual landmarks have been the biggest concern for this part of the project. Unfortunately, most natural landmarks do not have sufficient features to create a viable landmark. Therefore an accomplishment has been finding features that are robot friendly and can be easily learned and recognized by the visualization technology. Friendly features have multiple shapes with thick outlines so the camera can still make them out at large distances. Solid color shapes have few

features and are ineffective. Multiple small distinct shapes offer a large number of features but can only be detected at short distances. The maximum distance a well-defined landmark can be detected has experimentally determined to be about 125 cm while other less distinct landmarks have been detected at about 60 cm. This has led to the determination that the camera should be repositioned toward the front of the robot in order to avoid missing potential landmarks that are out of range due to the obstacle avoidance behavior.

A third accomplishment has been in the creation of effective monitoring tools. During operation, a robot continually collects information on both its wheel odometry and corrected odometry x, y coordinates. It also assesses when landmarks are created, when they are re-identified, and whether a successful range to the object was established. All of this information is internal to the robot's navigation mechanism. We have established an effective method that captures the information in real-time and logs it to a file for further analysis. Although these tools could still be improved upon, they are sufficient for determining effectiveness of the robot's position estimate.

A few experiments were performed to investigate the use of inertial guidance techniques as a way to produce accurate position information for the mobile nodes. An embedded system software development environment was built for one of the laboratory's O-Navi inertial guidance platforms. This board was comprised of an embedded microcontroller tied to accelerometers and solid-state gyroscopes. Software for the embedded processor and for the PC was created to transfer the inertial data from the board to the PC. The PC software then manipulated the inertial data in real time to update the current velocity and location of the mobile node. It was determined that the O-Navi embedded system that was being considered was not well-suited for the application. Very precise data are needed to perform inertial guidance. As shown in the Figure 1.3-4, considerable noise and non-negligible shifts in bias point have made inertial guidance impossible with the current setup.

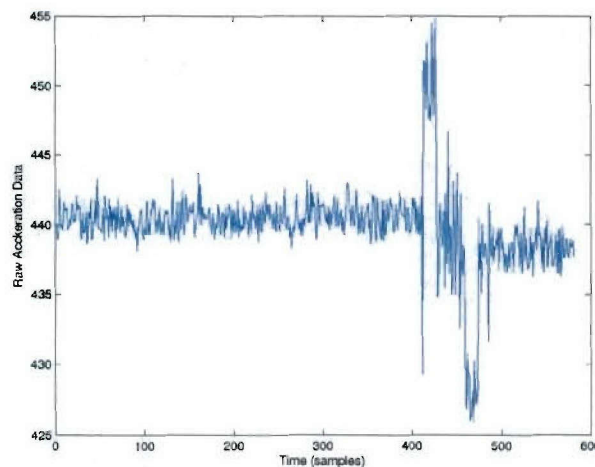


Figure 1.3-4 Raw accelerometer data acquired from robot movement acquired from the O-Navi inertial sensor board.

In the next quarter, work will primarily revolve around the creation of an effective map as the robot's working environment. Multiple artificial landmarks will be placed in the space to allow for continual correction of the robot's position. Additional code will most likely be developed to direct the robot to its last known landmark after a fixed time limit without seeing a landmark to ensure its position data does not drift too far between landmarks. Testing will be extended to include multiple robots all using the same generated map. This is the proposed solution for

determining each robot's position relative to the other robots. Work will also be conducted to create an offset between the local robot's map and the base station so that position relative to that station can be calculated and used in the beam forming algorithms.

1.3.2.3 Mobile Radio Platform

The final project prototype will utilize the 8 GHz UWB software defined radio also developed under the AWINN project. Until this becomes available, the radio team considered other intermediate radio platforms that could be readily adapted to our prototyping needs. Because the proposed mobile radio system on each node is comprised of a complex interaction between the flexible receiver and transmitter, it was necessary to derive a method of communication between the devices that gives an acceptable end-to-end delay and delay jitter. The inter-node communication link will have to be controlled precisely as exact information about the current time and location of the node will be required. Two laboratory platforms considered for this were the Red River Engineering WaveRunner M301 PMC software-defined transceiver and the Harris PM1 platform.

At first, an attempt was made to use the Red River's Wave Runner digital transceiver hardware. This module is a compact PMC-format card that communicates to a host using a PCI bus. The team quickly assembled a Xilinx M310 FPGA-based board with the Red River card. The Xilinx board was running Linux on a PowerPC. After performing a few initial experiments, it was determined that we could not obtain a high-degree of timing control on this board, needed to precisely manipulate the transmitter functions. When this was discovered, the team shifted focus to the Harris Programmable Modem platform instead.

The Harris Programmable Modem platform, one in a series of research prototypes created by The Harris Corporation's Government Communications Division (Melbourne, Florida), is a versatile platform for communications research. Harris has been a leading pioneer in both research and commercialization of Software Defined Radios. The Virginia Tech Configurable Computing Laboratory has been working with the research and development team within Harris to better exploit the configurability and security potential of their programmable modem platforms.

Harris' Programmable Modem platform is amazingly configurable, allowing the rapid construction of common radio waveforms. The Programmable Modem can function well beyond the capabilities of conventional fixed radio platforms by exploiting dynamic configurability as well as reconfigurability among: components, waveforms, and processing paths. Harris' Software Defined Radio platforms are designed and developed utilizing the Software Communication Architecture (SCA) infrastructure specifications developed by the US DoD Joint Tactical Radio System (JTRS) for radio communication.

Multiple waveforms are supported on a single card along with various modulator and demodulator types. New waveforms are easily implemented, and flexible mezzanine cards can be interchanged for application customization. The system FPGAs can change dynamically, creating different hardware combinations using Harris-developed, software-controlled programmable modem technology and waveforms.

The Harris PM1 Programmable Modem consists of four FPGAs on the baseband board with an additional FPGA on a mezzanine transmitter card, and an additional mezzanine receiver card. The baseband board provides excellent infrastructure for data processing and system input/output. In addition to the FPGAs, DSPs assist in the overall system control. The baseband board has an expansion header that couples with a specialized mezzanine board. In addition to a high-capacity

FPGA, the transmitter mezzanine card contains a high-speed D/A converter, programmable filters, an up-converter, and gain stages, allowing it to directly drive an antenna. The receiver mezzanine card contains a 2 GHz direct down converter, programmable filters, and a high-speed A/D converter, which mates to another high-capacity FPGA. Overall, the system is nicely partitioned, allowing a designer to quickly develop a radio prototype. In addition to the raw signal processing capability, there are ample resources on-board to facilitate the exploration of interesting reconfigurable radio management functions. Harris has been using this platform on a number of military programs, including the Tactical Common Data Link (TCDL), the Navy AEHF, the Army WIN-T, and JTRS.

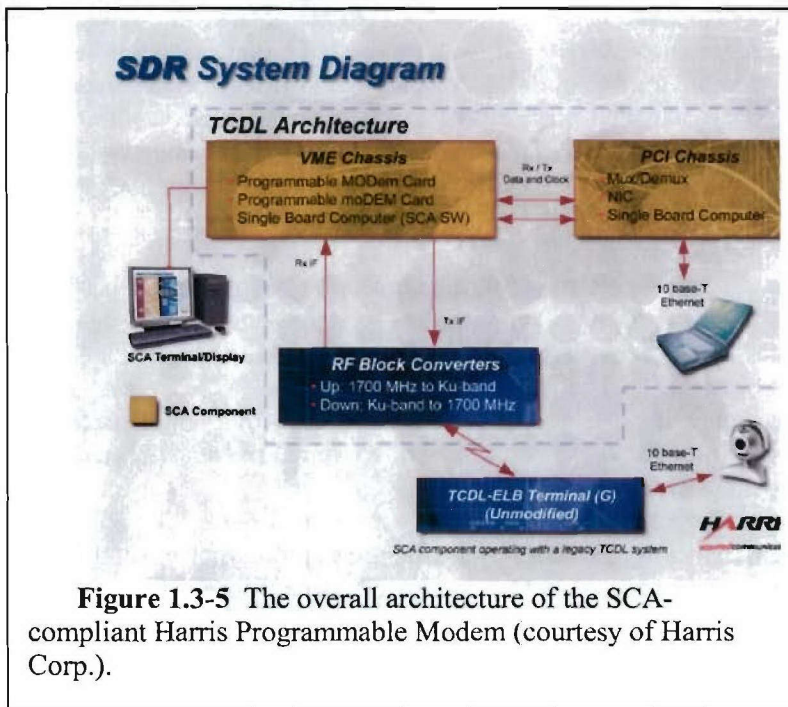


Figure 1.3-5 The overall architecture of the SCA-compliant Harris Programmable Modem (courtesy of Harris Corp.).

On the Harris Programmable Modem platform (see Fig. 1.3-5), the receiver and transmitter are on separate boards and only connected via a VME bus. Furthermore, the transmitter and receiver are on daughter cards and are separated from the VME bus by another bus and the control FPGA. The VME bus's speed causes a problem when the two boards need to communicate with one another in time sensitive applications such as the current application.

As a work around solution, the radio team is attempting to connect the two daughter cards directly to one another via a 16 bit test port provided on both. Through the test port, they will transmit data as well as a "go" signal to the Harris transmitter. The "go" signal will specify when the transmitter card should transmit the data it has obtained from the receiver. This way, the task of computing sending times can remain on the receiver and thus reduce the amount of information that needs to be sent to the transmitter board. If success is achieved in resending received data, the end-to-end delay will need to be measured. If the skew is too great, then the sending time will not be controllable to the degree necessary to match up the phases between nodes to perform beamforming. If the end-to-end delay is successful, then the digital design for inter-node communication will be designed and created. This hardware will be responsible for tracking time, deciding when to transmit data to the base station, and transmitting data between nodes.

1.3.2.4 Embedded Multi-core RTOS for Node Management

In this task, nodes in the sensor network will need to sequence their operations carefully. Due to the nature of the multitude of computational tasks required on each node, a popular embedded real-time operating system (RTOS) is being adapted for use in our soft-core FPGA platform for the purposes of modem management.

The Xilinx MicroBlaze is a soft processor intended to be used in FPGA applications and embedded products. Its acceptance has recently grown in the embedded and research

communities and several groups have contributed or created products that have increasingly aided its popularity. For instance, an Australian university ported the ucLinux real-time operating system to the MicroBlaze and this combination has become a viable option for developers.

In the Virginia Tech Configurable Computing Laboratory, researchers have been conducting research in the field of configurable computing. One of the products of this research has been a MicroBlaze instruction-level compatible soft-processor called the *OpenFire*, which has been recently released as open source. To further his research in configurable arrays, an operating system is required. eCos is a popular open-source operating system frequently used in single application, single-process embedded products. Originally maintained by the RedHat Corporation (it is not a Linux product), it is now maintained by an independent group.

eCos is an excellent choice as an operating system for the MicroBlaze platform for the following reasons:

- eCos is popular and well-received in the community as is the Xilinx MicroBlaze
- Many developers, institutions and companies have requested an eCos port for the MicroBlaze over the past years all over the world and one is yet to be created.
- The eCos system is simple - it is intended for processors that contain no memory management unit (MMU).
- eCos is extendible and configurable. Its popularity and power comes from its simplicity and the ability to choose exactly which components you would like included and the ability to add others. This enables it be a workable solution for all types and sizes of applications and systems.
- eCos is open-source enabling us to extend and modify it to future applications and research.

The Configurable Computing Laboratory has undertaken the task of producing a port of the eCos RTOS for the Xilinx MicroBlaze/ML310 and ultimately the OpenFire processor.

As of now, the team has completed an implementation of the configuration tool portion of the system and almost completely mapped the requirements needed by the operating system against the capabilities of the processor. A base for the port has been selected, that of the MBX/PowerPC platform. This was a suitable starting point because of the simplicity of its eCos implementation. This new base is almost fully registered with the supplied configuration tool.

The eCos configuration tool requires that the individual sections be written manually in a pseudo-language called CDL, the Component Description Language, which is an extension the Tcl/Tk language. The configuration tool recognizes which portions of the code can be conditionally compiled into the RTOS executable and how to present these options to the user. It also determines compilation options, such as which libraries are available in the build chain (such as math and string processing) as well as the level of the library support. The CDL portion consists of a hierarchical structure of configuration files resident with the necessary drivers and source code. Little work remains in completing the research required of the MicroBlaze platform and its tool chain. Much expertise is available in the lab on MicroBlaze's structure as with the eCos system itself.

The team is now able to successfully lay out a source tree suitable for a RTOS build. This alone is a milestone that will assist us in the development process. The configuration tool is capable of creating a suite of testing applications and libraries to test the implementation as well as building a RedBoot instance for the platform. RedBoot is a specialized bootstrap environment that can

assist in booting and loading applications as well as communicating with the outside world via serial port or Ethernet.

Significant challenges remain. eCos porting is a formidable task as documentation is sparse and the only authoritative guidelines are existing ports. A port requires starting from an existing platform and manually line-by-line determining which sections are required, which are incompatible and which are optional. For optional sections, a suitable configuration option and a manner that enables this code to be conditionally compiled without affecting the rest of the code is needed.

Since the code is embedded assembly code within macros, there are few portions that can be unit tested until the entire port is completed. Errors can also be missed during compilation as with traditional applications. In addition, research is required to determine the assembly code required to implement the service level routines. These routines include thread context switches, enabling and disabling **interrupts**, handling software and hardware interrupts, enabling and disabling the different caches and saving and restoring the context under various circumstances. These require extensive mapping of the target hardware to the HAL and mapping the memory to enable eCos to handle its vector table.

1.3.3 Importance/Relevance

Software defined radios have the potential of changing the fundamental usage model of wireless communications devices, but the capabilities of these transceivers are often limited by the speed of the underlying processors. Here we make an attempt to solve this problem by using reconfigurable architectures to develop custom datapaths which can handle these high data rates using commercially available FPGAs as an alternative to custom ASICs which lead to the obvious cost and development time benefits. An added advantage of such architecture is the capability to use run-time reconfigurability to adapt to the effects of pulse shaping, channel coding, error control, and network algorithms on UWB communication. It can also be used to implement advanced cryptosystems or obfuscate communication.

1.3.4 Productivity

Conference publications

- D. Agarwal, "An 8 GHz UWB Transceiver Prototyping Testbed," Master's Thesis, Virginia Tech, Blacksburg, VA, Oct 2005.
- Brian Marshall, "A Swarm Intelligence Approach to Distributed Mobile Surveillance", Master's Thesis, Virginia Tech, Blacksburg, VA, Sep 2005.
- Stephen Craven, Cameron Patterson, and Peter Athanas, "A Methodology for Generating Application-Specific Heterogeneous Processor Arrays", Proceedings of the 39th Hawaii International Conference on System Sciences, HICSS 2006 / MOCHA 2006, Kauai, HI, Jan 2006.

Invited talks

P. Athanas, "Secure Communications and High Performance Configurable Computing," Wright State University, Department of ECE Seminar Series, September 2005.

Students supported

Deepak Agarwal, MSEE (graduated)
Brian Marshall, MSEE (graduated)
Todd Flemming, PhD student
Tingting Meng, PhD student
Yousef Islander, PhD student
James Webb, MSEE student
Matthew Blanton, MSEE student
Marc Somers, MSEE student
Lael Matthews, MSEE student

2. TASK 2 Secure and Robust Networks

2.1 Task 2.1 Ad Hoc Networks

2.1.1 Overview

Task Goal: This task investigates core network capabilities for quality of service (QoS), security, and routing in ad hoc networks, especially mobile ad hoc networks (MANETs).

Organization: This task is managed by Scott Midkiff and involves the following personnel:

Scott F. Midkiff, task director

Luiz A. DaSilva, faculty

Nathaniel J. Davis, IV, faculty (1/15/05-8/14/05)

Y. Thomas Hou, faculty

Shiwen Mao, post-doctoral research associate

Walter M. de Sousa, GRA (5/15/05-present)

George C. Hadjichristofi, GRA (4/1/05-5/14/05), Post-doctoral associate (7/25/05-present)

Unghee Lee, GRA (33% for 4/1/05-5/14/05, 100% for 5/15/05-present)

Xiaojuan Wang, GRA

Summary: This quarter we continued work on integration of routing and medium access control (MAC) protocols for ad hoc networks to support multiple channel operation, implementation of test bed conversion to support both Internet Protocol (IP) version 6 (IPv6) and IP version 4 (IPv4) including with IP Security (IPsec) and key management. We also continued to investigate how to exploit path diversity in ad hoc networks to better support video communication. The accomplishments and other details are provided in Section 2.1.2 below.

2.1.2 Task Activities for the Period

Subtask 2.1(a) Policy-based Quality of Service

Task Objective: The objectives of this subtask are to investigate and develop quality of service mechanisms that provide differential bandwidth allocation and scheduling based on traffic type, node type, and the current network environment. We seek to increase the adaptability of the QoS mechanisms to operate more robustly in a variety of environments. We will also explore automatic adaptation at the physical and data link layers in response to application and network-layer demands, as an initial exploration of cognitive networks as an approach to cross-layer optimization.

Accomplishments during reporting period: Investigation and planning for this task continued during this quarter. We made the decision to not modify the signaling components of policy-based network management (PBNM), developed during the NAVCIITI project, to work with IPv6. The level of effort would be too great to justify research benefits, mainly because we rely on an existing implementation of the Common Open Policy Services (COPS) protocol which would need to be written by us “from scratch” to work with IPv6. Instead, we will support IPv4 and IPv6 in the test bed, thus allowing PBNM signaling to be carried in IPv4 datagrams. Policy enforcement points (PEPs) will need to be IPv6 aware to apply policies to both IPv4 and IPv6 traffic. We also continued to investigate relevant literature in the field.

Links to other tasks: This subtask has natural synergies with Task 2.4 (Cross-Layer Optimization), as the mechanisms that support QoS in mobile ad hoc networks span the physical,

data link, network and application layers. It also integrates with Task 2.2 (Real-Time Resource Management, Communication, and Middleware) as some of the QoS mechanisms developed here will support real-time applications and must integrate with the real-time middleware developed in Task 2.2.

Schedule: The updated schedule for this subtask is as follows.

- Develop extended policy-based QoS mechanism (April-November 2005)
- Explore adaptability methods (July-December 2005)
- Integrate cross-layer design features (July-December 2005)
- Realize prototype implementation (July-December 2005)
- Integrate protocols using test bed (January-March 2006)
- Refine protocols based on performance evaluation and demonstrations (April-June 2006)

Personnel: The following personnel were assigned to this subtask during the quarter:

Luiz A. DaSilva, faculty (subtask leader)

Scott F. Midkiff, faculty

Waltemar de Sousa, GRA

Subtask 2.1(b) Security Mechanisms for Ad Hoc Environments

Task Objective: The objectives of this subtask are to investigate and, where feasible and deemed appropriate, develop security mechanisms that are efficient for ad hoc network environments. Our initial emphasis considers a distributed key management system (KMS) and associated shared trust schemes.

Accomplishments during reporting period: During the quarter, we upgraded our test bed to the latest version of the Linux kernel with Fedora Core 3, we moved to the Openswan implementation of IPsec, and we extended the Key Management System (KMS) to work in a mixed IPv4-IPv6 environment.

The upgrade of the Linux kernel was to improve support for IPv6 and IPsec and enable testing and integration of the network functionalities in an IPv6-based network. This has proven to be successful.

We identified the most suitable solution that would provide network -level security in our test bed and investigated deployment issues of IPsec over IPv6. Openswan, an IPsec implementation, has been integrated with IPsec built into the Linux kernel, thus overcoming the functionality and interoperability limitations that existed when utilizing the FreeS/WAN implementation of IPsec. More specifically, with FreeS/WAN IPsec, a virtual interface was created for a tunnel with keys negotiated using the Internet Key Exchange (IKE) protocol. This allowed packets to be routed through that interface. The functionality of FreeS/WAN IPsec was limited because routing was used to determine the IPsec policy to be applied to every packet since packets destined for a particular subnet and requiring encryption had to be routed through the corresponding IPsec virtual interface. Furthermore, the MANET routing protocol operation conflicted with the FreeS/WAN IPsec operation. The routing protocol modified the subnet routing entries created by IPsec. Both of these limitations have been removed by deploying the Openswan IPsec mechanism since IPsec built into the kernel does not utilize IPsec virtual interfaces. This mechanism has been tested and can operate with both IPv6 and IPv4.

We successfully extended the Key Management System (KMS) developed in the NAVCIITI project and earlier in AWINN to accommodate security associations (SAs) between nodes

utilizing either IPv6 or IPv4. Any node can establish SAs by utilizing both its IPv4 and IPv6 addresses. The KMS has been integrated and tested with Openswan so that certificates can be dynamically distributed in the network to aid in the establishment of security associations in a MANET.

Links to other tasks: This subtask has synergies with Subtask 2.1(c) and Task 2.4 (Cross-Layer Optimization) as link layer and, especially, network layer information can be employed to improve key management and other security functions. We are working to deploy a prototype for evaluation in the test bed developed in Subtask 2.1(e) and use tools of Subtask 2.1(f).

Schedule: The schedule for this subtask is as follows. There is no change from the previous quarter.

- Develop DCA and trust management system (January-June 2005)
- Integrate cross-layer design features (July-September 2005)
- Realize prototype implementation (July-December 2005)
- Integrate protocols using test bed (January-March 2006)
- Refine protocols based on performance evaluation and demonstrations (April-June 2006)

Personnel: The following personnel were assigned to this subtask during the quarter.

Nathaniel J. Davis, IV, faculty (through 8/14/05 only)

Scott F. Midkiff, faculty (subtask leader)

George C. Hadjichristofi, post-doctoral associate (beginning 7/25/05)

Subtask 2.1(c) Ad Hoc Routing Optimization

Task Objective: The objectives of this subtask are to investigate schemes to improve routing and to use network layer functionality to improve other network services.

Accomplishments during reporting period: We continued to investigate the cross-layer design of a multi-channel system that integrates medium access control (MAC) functions and routing layer functions. We investigated the Channel Distribution Index (CDI) as a way to improve performance for channel assignment, implement a mechanism using virtual interfaces that allows control of the channel used for packet forwarding, and continued work on multi-channel version of the Open Shortest Path First with Minimum Connected Dominating Sets for Multiple Channels (OSPF-MCDS-MC or, simply, OMM) and Optimized Link State Routing for Multiple Channels (OLSR-MC) MANET routing protocols.

The Channel Distribution Index is an index to reflect the fairness of channel distribution in a multi-channel network. Depending on the network topology and traffic pattern, the channel allocation can become unfair and this unfair distribution can degrade network throughput. We identified the properties and proposed the definition of the CDI based on simulation studies using the Network Simulator 2 (ns2) package.

We implemented a Virtual Interface Module (VIM). The VIM driver is a logical network interface that implements special-purpose processing on data packets without actual physical packet transmission, while avoiding the complexity of changes to the kernel's network subsystem. This module plays a pivotal role in our prototype implementation, including channel decision, channel switching, and packet lookup functions.

We investigated the effectiveness of our multi-channel scheme. We implemented the OLSR-MC module to augment the existing Naval Research Laboratory (NLR) implementation of OLSR by

adding multi-channel capabilities. To realize OLSR-MC we introduced new message formats, including the Channel Update (CU) message and delayed initial HELLO message. The OLSR-MC protocol is currently being extended to work over IPv4 and IPv6-based networks. The OMM routing protocol was simulated in ns2 and is currently being implemented and tested.

Links to other tasks: This subtask has direct ties to Task 2.4 (Cross-Layer Optimization) as our focus makes the network layer a key part of our cross-layer optimization schemes. In addition, we will explore synergy with Task 2.2 (Real-Time Resource Management, Communication, and Middleware). We are deploying a prototype for evaluation in the test bed developed in Subtask 2.1(e) and use tools of Subtask 2.1(f).

Schedule: The updated schedule is as follows.

- Extend DSDV to support multi-channel MAC (January-March 2005)
- Extend OSPF-MCDS to support multi-channel MAC (April-June 2005)
- Extend Optimized Link State Routing (OLSR) to support multi-channel MAC (May-June 2005)
- Realized prototype implementation in Linux, including IPv6 support (July-November 2005)
- Provide enhanced support for policy-based network management (PBNM) (November-January 2005)
- Provide enhanced support for security services (October-December 2005)
- Integrate additional cross-layer enhancements (October-December 2005)
- Integrate protocols using test bed (January-March 2006)
- Refine protocols based on performance evaluation and demonstrations (April-June 2006)

Personnel: The following personnel were assigned to this subtask during the quarter.

Scott F. Midkiff, faculty (subtask leader)

Unghee Lee, GRA

Subtask 2.1(d) Cross-Layer Approach for Routing of Multiple Description Video over Ad Hoc Networks

Task Objective: The objectives of this subtask are to investigate a theoretical foundation for cross-layer approaches for carrying video using Multiple Description (MD) coding over ad hoc networks and to build on this foundation to demonstrate key concepts via a prototype implementation.

Accomplishments during reporting period: We continued to investigate how to exploit path diversity in ad hoc networks to better support video communications. The video coding that we employ is called Multiple Description coding, which is a new video coding technique that is uniquely suitable for video transport over wireless ad hoc networks. We consider the problem of how to support video multicast with MD video in ad hoc networks. Instead of just finding multiple paths in the network, we follow an application-centric, cross-layer routing approach with the objective of minimizing the overall video distortion. We propose an MD video multicast scheme where multiple source trees are used. Furthermore, each video description is coded into multiple layers to cope with diversity in wireless link bandwidths. Based on this multicast model, we formulate cross-layer multicast routing as a combinatorial optimization problem and propose an efficient solution procedure. Our preliminary results show significant gains for a wide range of network operating conditions.

During the quarter, we continued our efforts on prototype development and test bed demonstration of video communication in ad hoc networks.

Links to other tasks: This subtask has direct ties to Task 2.4 (Cross-Layer Optimization) as it considers cross-layer optimization schemes that involve applications, in this case, video. We are deploying a prototype for evaluation and this will be integrated into the test bed developed in Subtask 2.1(e).

Schedule: The updated schedule is as follows.

- Develop foundation for cross-layer optimization (January-July 2005)
- Develop prototype system (June-November 2005)
- Integrate prototype system into interoperability test bed (December 2005-January 2006)
- Conduct experiments with interoperability test bed (February-March 2006)
- Refine protocols based on performance evaluation and demonstrations (April-June 2006)

Personnel: The following personnel were assigned to this subtask during the quarter.

Y. Thomas Hou, faculty (subtask leader)

Shiwen Mao, post-doctoral associate

Xiaojun Wang, GRA

Subtask 2.1(e) Test Bed Evaluation and Demonstration

Task Objective: The objectives of this subtask are to integrate and demonstrate, through research and prototype implementations, key ideas from Subtasks 2.1(a), 2.1(b), 2.1(c), and 2.1(d) and, as feasible and appropriate, from Task 2.2 (Real-Time Resource Management, Communication, and Middleware), Task 2.3 (Network Interoperability and Quality of Service), and Task 2.4 (Cross-Layer Optimization). The objective includes exploring interactions between different components and functions and to evaluate and demonstrate both functionality and performance.

Accomplishments during reporting period: As noted in descriptions of Subtasks 2.1(b) and 2.1(c), we continued to deploy and test components to support the evolution of the test bed from supporting only IPv4 to supporting both IPv4 and IPv6. We completed the upgrade of the operating system in the test bed nodes to the most recent version of Red Hat Fedora Core Linux. We have demonstrated the integration of IPsec, KMS, and OLSR-MC, although further work is needed for combined support of both IPv4 and IPv6 in OLSR-MC. We have also modified and tested the OLSR-MC configuration to support routing across logical subnets to support our test bed configuration.

Links to other tasks: The test bed evaluation and demonstrations rely on results from Subtasks 2.1(a), 2.1(b), 2.1(c), and 2.1(d), as well as Tasks 2.2, 2.3, and 2.4.

Schedule: The updated schedule for this subtask is as follows:

- Identify and clarify needs (July-September 2005)
- Acquire and deploy test bed hardware (October 2005-January 2006)
- Deploy technologies in test bed (October 2005-March 2006)
- Final performance evaluation and demonstrations (April-June 2006)

Personnel: The following personnel were assigned to this subtask during the quarter.

Scott F. Midkiff, faculty (subtask leader)

George C. Hadjichristofi, post-doctoral associate (beginning 7/25/05)

Unghee Lee, GRA

Subtask 2.1(f) Configuration and Monitoring Tools

Task Objective: The objectives of this subtask are to investigate and develop software configuration and monitoring tools to facilitate network testing and demonstration.

Accomplishments during reporting period: We identified issues with our topology and node state monitor, TopoView, running in a combined IPv4-IPv6 environment. Issues relate to use of the Simple Network Management Protocol (SNMP) with IPv6 and changes to SNMP and Management Information Base (MIB) configuration in the new version of Linux. Work is continuing to resolve these problems.

Links to other tasks: The tools support the test bed described above for Subtask 2.1(e).

Schedule: The updated schedule for this subtask is as follows.

- Identify and clarify needs (April-September 2005)
- Implement and test tools (October 2005-January 2006)
- Utilization and refinement of tools (February-June 2006)

Personnel: The following personnel were assigned to this subtask during the quarter.

Scott F. Midkiff, faculty (subtask leader)

George C. Hadjichristofi, post-doctoral associate (beginning 7/25/05)

2.1.3 Importance/Relevance

Ad hoc networks are of particular importance to the Navy and other Department of Defense (DoD) units because of their ability to be quickly configured and operate without infrastructure. Research in ad hoc networks to date has been dominated by solutions to particular, specific problems and not to general system and network infrastructure issues. This task focuses on making ad hoc network operate successfully as a system with efficient routing, the ability to offer quality of service, and the robustness and security required of military networks. We also examine the challenging problem of delivering video, specifically Multiple Description video, in an ad hoc network.

2.1.4 Productivity

Journal publications (appeared)

1. G. C. Hadjichristofi, W. J. Adams, and N. J. Davis, "A Framework for Key Management in Mobile Ad Hoc Networks," *International Journal of Information Technology (IJIT)*, vol. 11, no. 2, pp. 31-61, 2005.
2. Y. T. Hou, Y. Shi, H. D. Sherali, and S. F. Midkiff, "On energy provisioning and relay node placement for wireless sensor networks," *IEEE Transactions on Wireless Communications*, vol. 4, no. 5, Sept. 2005.
3. C. Wang, B. Li, Y. T. Hou, K. Sohraby, and K. Long, "A stable rate-based algorithm for active queue management," *Computer Communications Journal*, vol. 28, no. 15, pp. 1731-1740, Sept. 2005.
4. J. Pan, L. Cai, Y. T. Hou, Y. Shi, and S. X. Shen, "Optimal base-station locations in two-tiered wireless sensor networks," *IEEE Transactions on Mobile Computing*, vol. 4, no. 5, pp. 458-473, Sept./Oct. 2005.

Journal publications (accepted)

1. Y. Shi, Y. T. Hou, H. D. Sherali, S. F. Midkiff, "Cross-layer optimization for routing data traffic in UWB-based sensor networks," *IEEE Journal on Selected Areas in Communications*.
2. Y. T. Hou, Y. Shi, J. Pan, A. Efrat, and S. F. Midkiff, "Maximizing lifetime of wireless sensor networks through optimal single-session flow routing," *IEEE Transactions on Mobile Computing*.

Conference publications (appeared)

1. Y. T. Hou, Y. Shi, H. D. Sherali, and S. F. Midkiff, "Prolonging sensor network lifetime with energy rovisioning and relay node placement," *Proc. IEEE Communications Society Conference on Sensor and Ad Hoc Communications and Networks (SECON)*, Sept. 26-29, 2005, Santa Clara, CA.
2. Y. Shi, Y. T. Hou, H. D. Sherali, and S. F. Midkiff, "Cross-layer optimization for routing data traffic in UWB-based sensor networks," *Proc. ACM Mobicom*, pp. 299-312, Aug. 28-Sept. 2, 2005, Cologne, Germany.
3. Y. T. Hou, Y. Shi, and H. D. Sherali, "On base station selection for anycast flow routing in energy-constrained wireless sensor networks," *Proc. Second International Conference on Quality of Service in Heterogeneous Wired/Wireless Networks (QShine)*, Aug. 22-24, 2005, Orlando FL.
4. K. Channakeshava, K. S. Phanse, L. A. DaSilva, B. Ravindran, S. F. Midkiff, and E. D. Jensen, "IP Quality of Service Support for Soft Real-Time Applications," *Proc. Workshop on Real-Time Networks (RTN)*, EuroMicro Conference on Real-Time Systems (ECRTS), July 5, 2005, Palma de Mallorca, Spain.

Conference publications (accepted)

1. R. W. Thomas, L. A. DaSilva, and A. B. MacKenzie, "Cognitive Networks," *Proc. First IEEE International Symposium on New Frontiers in Dynamic Spectrum Access Networks (DySPAN)*, Nov. 2005, Baltimore, MD.
2. U. Lee, S. F. Midkiff, and T. Lin, "OSPF-MCDS-MC: A routing protocol for multi-channel wireless ad-hoc networks," *Proc. IEEE Communications and Networking Conference (CCNC)*, Jan. 2006, Las Vegas, NV.

Students supported (100% unless otherwise noted)

Waltemar de Sousa 7/1/05-9/30/05
Unghee Lee, 7/1/05-9/30/05
Xiaojun Wang, 7/1/05-9/30/05

Faculty supported

Scott F. Midkiff, 7/1/05–9/30/05
Luiz A. DaSilva, 7/1/05–9/30/05
Nathaniel J. Davis, 7/1/05–8/14/05
Y. Thomas Hou, 7/1/05–9/30/05
George C. Hadjichristofi, 7/25/05-9/30/05 (post-doctoral associate)
Shiwen Mao, 7/1/05–9/30/05 (post-doctoral associate)

2.2 Task 2.2 Real-Time Resource Management, Communications, and Middleware

2.2.1 Overview

Task Goal: This task investigates new software technologies that support the Navy's need to rapidly deploy distributed, real-time systems.

Organization: This task is managed by Dr. Binoy Ravindran. Graduate student support includes: Jonathan Anderson (January 2005 – present)
Hyeonjoong Cho (January 2005 – present)
Edward Curley (May 2005 – present)

The objectives of Task 2.2 include:

1. Develop time/utility function (TUF)/utility accrual (UA) scheduling algorithms for scheduling Real-Time CORBA 1.2's distributable threads with *assured timeliness properties* under failures. Develop distributable thread maintenance and recovery (TMAR) protocols that are integrated with such scheduling algorithms.
2. Develop TUF/UA *non-blocking synchronization mechanisms* for synchronizing distributable threads and single-processor threads for concurrently and mutually exclusively accessing shared objects.
3. Investigate how TUF/UA scheduling algorithms, synchronization mechanisms, and TMAR protocols can co-reside with policy-based network QoS management schemes, and jointly optimize (with network QoS schemes) UA timeliness optimality criteria, as envisaged in Task 2.3.
4. Develop the *Distributed Real-Time Specification for Java (DRTSJ)* standard under the auspices of Sun's Java Community Process (JCP)¹, incorporating scheduling algorithms, synchronization mechanisms, and TMAR protocols developed in (1) and (2).

Embedded real-time systems that are emerging such as control systems in the defense domain (e.g., Navy's DD(X), Air Force's AWACS) are fundamentally distinguished by the fact that they operate in environments with dynamically uncertain properties. These uncertainties include transient and sustained resource overloads due to context-dependent activity execution times and arbitrary activity arrival patterns. For example, many DoD combat systems include radar-based tracking subsystems that associate sensor reports to airborne object tracks. When a significantly large number of sensor reports arrives, it exceeds the system processing capacity causing overloads, resulting in important tracks to go undetected.

When resource overloads occur, meeting deadlines of all application activities is impossible because the demand exceeds the supply. The urgency of an activity is typically orthogonal to the relative importance of the activity—e.g., the most urgent activity can be the least important and vice versa; the most urgent can be the most important and vice versa. Hence, when overloads occur, completing the most important activities irrespective of activity urgency is often desirable. Thus, a clear distinction has to be made between the urgency and the importance of activities during overloads. (During under-loads, such a distinction need not be made because deadline-

¹ The DRTSJ effort is currently ongoing under a JCP called JSR-50. The core members of the DRTSJ team include those from The MITRE Corporation and Virginia Tech.

based scheduling algorithms such as EDF are optimal for those situations [hor74]—i.e., they can satisfy all deadlines.)

Deadlines by themselves cannot express both urgency and importance. Thus, we consider the abstraction of time/utility functions (or TUFs) [jlt85] that express the utility of completing an application activity as a function of that activity's completion time. Utility is typically mapped to application-level quality of service (QoS) metrics such as track quality and track importance in a command and control application. We specify deadline as a binary-valued, downward “step” shaped TUF; Figure 2.2-1(a) shows examples. Note that a TUF decouples importance and urgency—i.e., urgency is measured as a deadline on the X-axis, and importance is denoted by utility on the Y-axis.

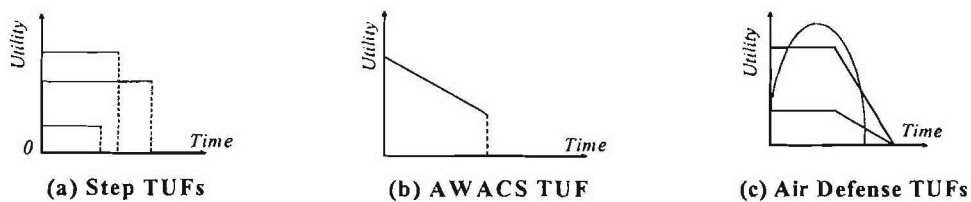


Figure 2.2-1 Example timing requirements specified using time/utility functions.

Many embedded real-time systems also have activities that are subject to *non-deadline* time constraints, such as those where the utility attained for activity completion *varies* (e.g., decreases, increases) with completion time. This is in contrast to deadlines where a positive utility is accrued for completing the activity anytime before the deadline, after which zero or infinitively negative utility is accrued. Figures 2.2-1(b) and 2.2-1(c) show such example time constraints from two real applications (see [cjk+99] and the references therein).

When activity time constraints are specified using TUFs, which subsume deadlines, the scheduling criteria is based on accrued utility, such as maximizing sum of the activities attained utilities. We call such criteria *utility accrual* (or UA) criteria and scheduling algorithms that optimize them are called UA scheduling algorithms.

UA algorithms that maximize summed utility under downward step TUFs (or deadlines) [loc86, cla90, wrjb04] default to EDF during under-loads, because EDF can satisfy all deadlines during those situations. Consequently, they obtain the maximum total utility during under-loads. When overloads occur, they favor activities that are more important (because more utility can be attained from them), irrespective of their urgency. Thus, UA algorithms' timeliness behavior subsumes the optimal timeliness behavior of deadline scheduling.

The major Task 2.2 accomplishments this quarter include work on Distributed Thread scheduling and Distributed Thread integrity. As a part of a demonstration, a testbed is being created to explore the behavior of various thread integrity, or “Thread Maintenance and Repair” (TMAR) algorithms. The first implementation of the Thread-polling algorithm on the Tempus middleware is nearly complete. New results for the timeliness and fault-tolerance properties of this algorithm will be documented.

Significant analytical work in the area of Distributed Thread scheduling has produced two new consensus-based algorithms. These algorithms, given some a-priori knowledge of the Distributed Thread topology and runtime behavior, yield “optimal” schedules in the case of underload and no failures. Further work characterizing their behavior in more challenging environments is ongoing.

With respect to DRTSJ, permission was recently granted to sign the Sun JSPA agreement. This frees our research group to start work on the DRTSJ reference implementation and begin integrating technologies previously implemented in Tempus with our research focus. We summarize this result in Section 2.2.2.

Summary: This quarter the following activities were performed:

Produced a Thread Integrity Manager subsystem for the Tempus middleware

- Produced an implementation of the Thread-Polling TMAR algorithm in Tempus
- Simulated the behavior of new distributed thread scheduling algorithms
- Integrated TMAR algorithms into our demonstration

2.2.2 Importance/Relevance

We believe that the TUF/UA real-time technology developed in this task is directly relevant to DoD's network-centric warfare concept, Navy combatant systems including DD(x), and other DoD systems such as Air Force's next generation command and control aircrafts. In fact, the fundamental aspects of this class of real-time problems include:

1. Need for transparent programming and scheduling abstractions for distributed computation workflows that are subject to time constraints.
2. Systems that are subject to significant run-time uncertainties that are often manifested in execution and communication times, and event and failure occurrences that are non-deterministically distributed.
3. Systems that are subject to transient and permanent overloads.
4. Need for time-critical and mission-oriented resource management (i.e., timely management of resources in the best interest of the current application mission).
5. Need for industry/commercial standards- and COTS-based solutions for portability, robustness, and maintainability.

All these aspects are directly addressed by Task 2.2 research. In particular, Real-Time CORBA 1.2's and DRTSJ's distributable threads abstraction provides a transparent programming and scheduling abstraction for distributed real-time computation workflows. Further, the class of TUF/UA scheduling algorithms, TMAR protocols, synchronization mechanisms, and policy-based network QoS management schemes target application activities, whose execution/communication latencies and event/failure occurrences are non-deterministically distributed and are subject to overloads. TUF/UA algorithms provide time-critical and mission-oriented resource management by (system-wide) scheduling to maximize system-wide accrued utility, where utility is mapped to application-level QoS. Consequently, utility maximization leads to managing system resources to maximize utility achieved for the users by the system. Furthermore, Task 2.2's work on the DRTSJ industry standard directly promotes industry/commercial standards and COTS-based solutions.

Thus, Task 2.2 research is directly relevant to Navy systems and other DoD systems.

DD(X) is currently using RTSJ, and is building a distributed real-time infrastructure using RTSJ. The DD(X) team has expressed significant interest in using DRTSJ – in particular, the distributable threads abstraction and end-to-end timing analysis capability. We believe that

DD(X) can directly leverage DRTSJ's advanced adaptive time-critical (TUF/UA) resource management techniques, and DRTSJ's synergy with RTSJ.

2.2.3 Productivity

Journal publications

1. P. Li, H. Wu, B. Ravindran, and E. D. Jensen, "On Utility Accrual Resource Management with Assured Timeliness Behavior," *IEEE Transactions on Computers*, Submitted October 2005 (under review).
2. H. Wu, B. Ravindran, E. D. Jensen, and P. Li, "Energy-Efficient, Utility Accrual Scheduling under Resource Constraints for Mobile Embedded Systems," *ACM Transactions on Embedded Computing Systems*, Accepted September 2005.
3. H. Wu, B. Ravindran, E. D. Jensen, and P. Li, "Time/Utility Function Decomposition Techniques for Utility Accrual Scheduling Algorithms in Real-Time Distributed Systems," *IEEE Transactions on Computers*, Volume 54, Number 9, pages 1138 - 1153, September 2005.

Conference publications

1. H. Wu, B. Ravindran, and E. D. Jensen, "Utility Accrual, Real-Time Scheduling with Energy Bounds," *2006 ACM Symposium On Applied Computing (SAC), Track on Embedded Systems*, Submitted September 2005.
2. H. Cho, B. Ravindran, and E. D. Jensen, "On Utility Accrual Processor Scheduling with Wait-Free Synchronization for Embedded Real-Time Software," *2006 ACM Symposium On Applied Computing (SAC), Track on Embedded Systems*, Submitted September 2005.
3. P. Li, B. Ravindran, and E. D. Jensen, "Utility Accrual Real-Time Resource Access Protocols with Assured Individual Activity Timeliness Behavior," *2006 ACM Design, Automation, and Test in Europe (DATE), Real-Time Systems Track*, Submitted September 2005.
4. H. Cho, B. Ravindran, and E. D. Jensen, "Lock-Free Synchronization for Dynamic Embedded Real-Time Systems," *2006 ACM Design, Automation, and Test in Europe (DATE), Real-Time Systems Track*, Submitted September 2005.
5. H. Cho, H. Wu, B. Ravindran, and E. D. Jensen, "Multiprocessor Utility Accrual Real-Time Scheduling With Statistical Timing Assurances," *2006 IEEE Real-Time and Embedded Technology and Applications Symposium (RTAS)*, Submitted October 2005.
6. H. Wu, U. Balli, B. Ravindran, and E. D. Jensen, "Utility Accrual Real-Time Scheduling Under Variable Cost Functions," *IEEE International Conference on Embedded and Real-Time Computing Systems and Applications (RTCSA)*, Hong Kong, August 17-19, 2005.

Students supported

Jonathan Anderson, January 2005 – present
Hyeonjoong Cho, January 2005 – present
Edward Curley, May 2005 – present

References

- [cla90] R. K. Clark, "Scheduling Dependent Real-Time Activities," PhD thesis, CMU CS Dept., 1990.

- [cjk+99] R. K. Clark, E. D. Jensen, et al., "An adaptive, distributed airborne tracking system," In *IEEE WPDRTS*, pages 353--362, April 1999.
- [hor74] W. Horn, "Some Simple Scheduling Algorithms," *Naval Research Logistics Quarterly*, 21:177--185, 1974.
- [jlt85] E. D. Jensen, C. D. Locke, and H. Tokuda, "A time-driven scheduling model for real-time systems," In *IEEE RTSS*, pages 112--122, December 1985.
- [loc86] C. D. Locke, "Best-Effort Decision Making for Real-Time Scheduling," PhD thesis, Carnegie Mellon University, 1986.
- [wrjb04] H. Wu, B. Ravindran, E. D. Jensen, and U. Balli, "Utility Accrual Scheduling Under Arbitrary Time/Utility Functions and Multiunit Resource Constraints," *IEEE Real-Time Computing Systems and Applications*, April 2004.

2.3 Task 2.3 Network Interoperability and Quality of Service

2.3.1 Overview

Task Goal: The goal of Task 2.3 is to integrate network services (as investigated in Task 2.1) with real-time middleware (as investigated in Task 2.2). Specifically, we will investigate and develop methods and mechanisms to integrate policy-based quality of service (QoS) capabilities at the network level, and perhaps at the link layer, with real-time services offered by middleware.

Organization: This task is managed by Scott Midkiff using the following personnel:

Scott F. Midkiff, task director

Luiz A. DaSilva, faculty

Binoy Ravindran, faculty

Summary: Task 2.3 integrates results from Tasks 2.1 and 2.2. As these tasks are just beginning, no significant activity specifically in support of Task 2.3 took place during the reporting period beyond continuation of integration planning. The following sections summarize subtasks and schedule.

2.3.2 Task Activities for the Period

Task Objective: The goal of Task 2.3 is to integrate network services (from Task 2.1) with real-time middleware (from Task 2.2).

Accomplishments during reporting period: We did continue planning integration of the two tasks.

Links to other tasks: This task integrates results from Task 2.1 and Task 2.2. It is also potentially synergistic with Task 2.4 (Cross-Layer Optimization) because it may be possible to integrate optimizations at the link and network layer with requirements presented by the real-time middleware.

Schedule: The revised schedule for this task is as follows:

- Plan integration approach (April-November 2005)
- Begin integration based on preliminary results (December 2005-January 2006)
- Integrate cross-layer design features (January-February 2006)
- Integrate protocols using test bed (March-April 2006)
- Refine protocols based on performance evaluation and demonstrations (May-June 2006)

Personnel: No personnel were assigned to this subtask for the reporting period.

2.3.3 Importance/Relevance

Many military systems rely on real-time operation, but can often be characterized using “soft” real-time constraints. This work paves the way to providing real-time capabilities, based on time-utility functions (TUFs), in an ad hoc network environment.

2.3.4 Productivity

There is currently no productivity items to report for Task 2.3.

2.4 Task 2.4 Cross-Layer Optimization

2.4.1 Overview

Task Goal: The goal of this task is to investigate and develop methods and metrics to characterize and evaluate the interaction between physical, data link, network and application layer protocols. This will be accomplished through two specific applications (a) position location networks and (b) collaborative radio networks.

Organization: This task is managed by Dr. R. Michael Buehrer and Dr. Scott Midkiff.

Dr. R. Michael Buehrer, faculty
Dr. Scott Midkiff, faculty
Dr. Tom Hou, faculty
Qiao Chen, GRA
Swaroop Venkatesh, GRA

Summary: In this quarter we have focused on two subtasks: (a) Cross-layer design for UWB position-location networks and (b) collaborative radio networks. The latter sub-task has been broken down into two studies, the study of collaborative UWB networks and collaborative beam-forming techniques.

2.4.2 Task Activities for the Period

2.4.2.1 Subtask 2.4.1a Cross-Layer Design for Ultra-Wideband Position-Location Networks

Introduction: In this subtask, we look at the problem of location estimation in the absence of LOS between the unlocalized node and location-aware “anchor” nodes. This problem has been considered before, but mostly [1] in the context of cellular communications. In indoor position-location networks, the line-of-sight (LOS) path between nodes is likely to be obstructed as shown in Figure 2.4-1. As a consequence, the TOA-based range estimates that are used to compute a node’s location are biased with high probability. These bias errors in the range estimates lead to large errors [1] in the computation of a node’s location. The literature on the NLOS problem typically falls in two categories: *NLOS Identification* and *NLOS mitigation*. The former deals with the problem of distinguishing between LOS and NLOS range estimates, whereas the latter typically deals with the reduction of NLOS range errors, once the NLOS ranges have been identified.

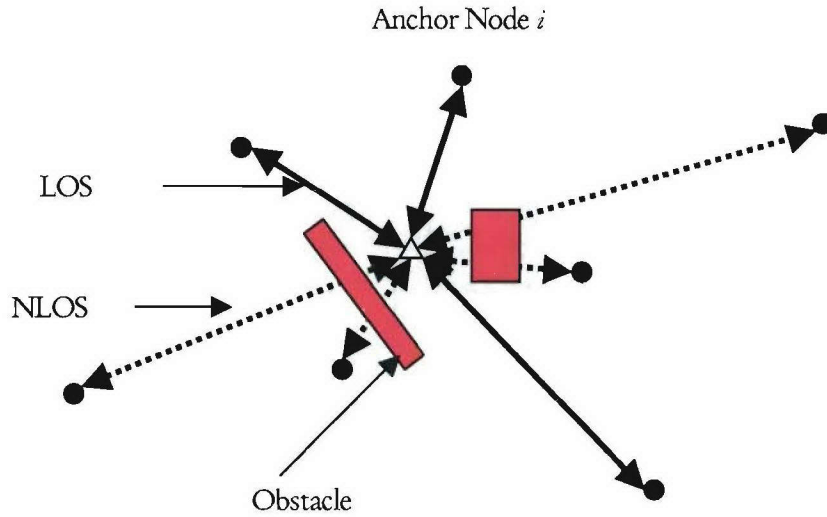


Figure 2.4-1 Illustration of Ranging in NLOS propagation environments.

Several statistical NLOS identification techniques (mostly for cellular systems) have been discussed previously [2]. A simplistic approach to the NLOS identification problem in the case of UWB signals would be to observe the received multipath profile and apply hypothesis testing to the delay spread of the multipath profile. For a given transmit power, a small delay spread would indicate an LOS range estimate and a large delay spread would indicate an NLOS range estimate. In this section, we look at NLOS mitigation techniques with the assumption that the NLOS range estimates have been identified. The Cramer-Rao Lower Bound analysis presented in [3] suggests that, given a mixture of LOS and NLOS range estimates, the minimum variance unbiased estimator (MVUE) of the unknown location discards the biased NLOS range estimates and utilizes only LOS range information. However as will be demonstrated, in the case of practical estimators, such as the Least-Squares (LS) estimator [4], discarding NLOS range information does not necessarily improve performance. Additionally, for two-dimensional position-location, we require at least three range estimates to obtain an unambiguous solution. In indoor PoLoNets, limited connectivity may imply that we may not have the luxury of discarding any range estimates.

We present a linear programming approach in order to incorporate both LOS and NLOS range information into the solution of a node location. This approach was suggested in [5], but was not analyzed. A Semi-Definite Programming (SDP) approach was investigated in [6], but results in high computational complexity [5]. A quadratic programming approach with TOA-based ranges was discussed in [7]. The Residual Weighting Algorithm (Rwgh) was proposed in [8]. The main advantage of this algorithm is that NLOS identification is not required *a priori*. However, this algorithm implicitly assumes that the range measurement noise is much smaller than the bias introduced in order to distinguish between the LOS and NLOS range estimates. Additionally, this algorithm relies on the availability of a large number of range estimates, so that the set of range estimates finally selected to compute a nodes location results in the smallest error.

Motivation: Let the node whose location is to be estimated be $\mathbf{x} = [x \ y]^T$. The LOS range estimates r_{Lj} are modeled as Gaussian unbiased estimates of the true ranges R_{Lj} :

$$r_{Lj} = R_{Lj} + n_{Lj}, \quad j = 1, 2, \dots, m_L.$$

where R_{Lj} represents the true distance between nodes i and j and n_{Lj} represents zero-mean Gaussian range measurement noise in the j th range estimate:

$$n_{Lj} \sim \mathcal{N}(0, \sigma_j^2), \quad \sigma_j^2 = \frac{K_R R_{Lj}^n}{K_p P_T} = K_E R_{Lj}^n, \quad j=1, 2, \dots, m_L,$$

where,

$$K_E = \frac{K_R}{K_p P_T}$$

is the **proportionality** constant that determines the dependence of the variance of the range estimate on the true range. The NLOS range estimates are assumed to be positively biased Gaussian estimates of the true ranges:

$$r_{Nj} = R_{Nj} + n_{Nj} + b_{Nj}, \quad j = 1, 2, \dots, m_N.$$

We assume that the bias errors are much larger than the standard deviation of the range measurement noise: $b_{Nj} \gg \sigma_{Nj}, j=1, 2, \dots, m_N$. This assumption is justified in the case of UWB signals since the standard deviation of the measurement noise is of the order of centimeters, and the bias errors could be of the order of meters. We further assume that the coordinate axes are selected such that $\mathbf{x} \geq \mathbf{0}$. When the number of NLOS range estimates $m_N = 0$, the LS estimator [4] can be used to accurately estimate the location \mathbf{x} . However, when $m_N > 0$ we need effective ways of incorporating NLOS information into the estimation procedure. Directly incorporating the NLOS ranges into the LS solution without correction can lead to an increase in error as shown in Figure 2.4-2. Here, the measure of localization accuracy used is the *localization error* defined by

$$\Omega = \|\mathbf{x} - \hat{\mathbf{x}}\|^2$$

where $\hat{\mathbf{x}}$ is the computed LS estimate. However, in some cases, introducing the NLOS range estimate directly into the LS estimation without any mitigation of the bias in the range, can *improve* performance (in terms of the statistics of the localization error) as shown in Figure 2.4-3. In general, discarding the NLOS range estimates does not result in poor performance when the geometry of LOS anchor nodes has a high GGDOP. In practice however, we cannot guarantee good geometrical conditions in indoor ad hoc position-location networks. In the case of poor geometry of anchors, the presence of an additional range estimate compensates for the inaccuracy of the added range estimate.

These two examples show that directly incorporating NLOS ranges into existing practical estimators without reducing the impact of the bias can adversely impact localization accuracy. At the same time, we do not wish to discard the NLOS range estimates, since their use could improve the performance of practical estimators. Indeed, in indoor networks, we may have more NLOS range estimates than LOS range estimates. Therefore, we are looking for a method that incorporates NLOS range estimates effectively, while mitigating the impact of their (unknown) bias.

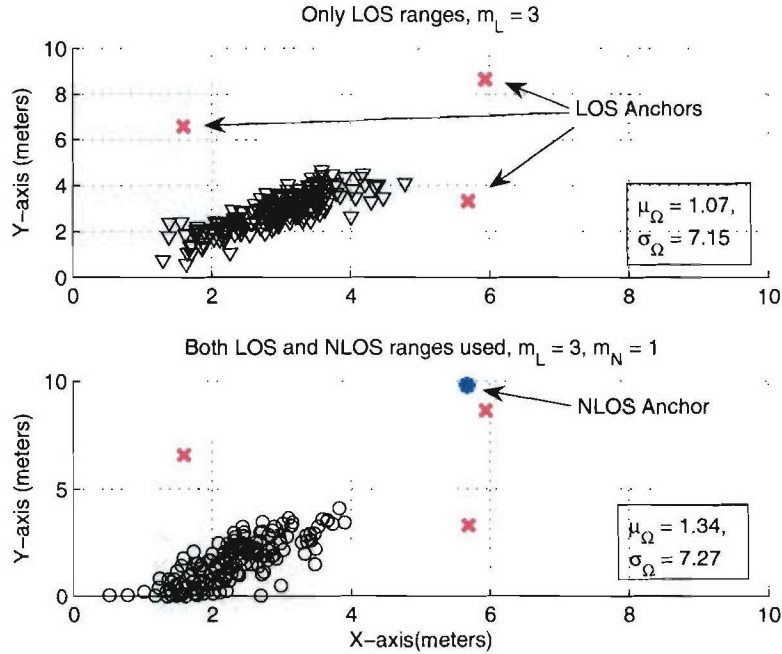


Figure 2.4-2 An example illustrating a case where directly incorporating NLOS range estimates degrades performance. This example shows several instances of the location estimate $\hat{\mathbf{x}}$, one for each realization of the Gaussian range measurement noise, with $\mathbf{x} = [3 \ 3]^T$. In this case, $m_L = 3$, $n = 2$, $K_E = 0.1$ (this implies that the standard deviation of the range measurement noise is 1 meter which the true distance is 10 meters) μ_Ω and σ_Ω (both in meter²) represent the mean and standard deviation of the localization error Ω over a large number of range measurement noise realizations.

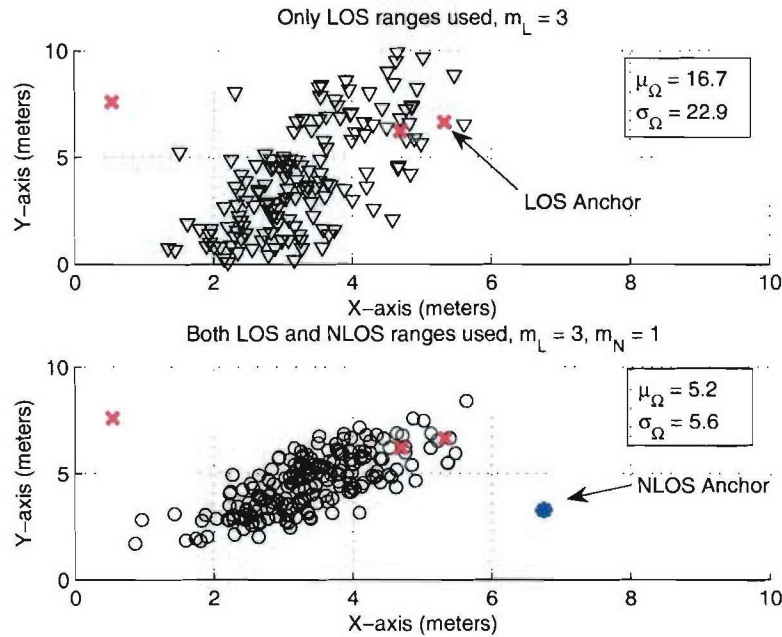


Figure 2.4-3 An example illustrating a case where NLOS range estimates are useful, even when directly incorporated into the LS solution without the mitigation of bias errors. This example shows several instances of the location estimate $\hat{\mathbf{x}}$, one for each realization of the

Gaussian range noise, with $\mathbf{x} = [3 \ 3]^T$. In this case, $m_L = 3$, $m_N = 1$, $K_E = 0.1$, $B_{\max} = 4$ meters (which implies that the maximum TOA measurement error is approximately 12 nanoseconds) and the Least-Squares (LS) estimator was used to compute $\hat{\mathbf{x}}$. The NLOS range estimated is treated exactly like an LOS range estimate and is directly incorporated into the LS solution.

A Linear Programming Approach

The LOS ranges, which are unbiased, are treated as accurate. We can write

$$\begin{aligned}\|\mathbf{x} - \mathbf{x}_i\| &= r_{Li}, \quad i = 1, 2, \dots, m_L \\ (x - x_i)^2 + (y - y_i)^2 &= r_{Li}^2\end{aligned}\tag{2.4-1}$$

These equalities are non-linear relations in x and y and represent the fact that \mathbf{x} lies on a circle of radius r_{Li} whose center is \mathbf{x}_{Li} . These can be linearized by taking the difference of each of these equations from the others, forming a system of $M = \binom{m}{2}$ distinct equations:

$$\begin{aligned}a_{ij}x + b_{ij}y &= c_{ij}, \quad i = 1, 2, \dots, m_L \\ a_{ij} &= (x_{Li} - x_{Lj}), \quad b_{ij} = (y_{Li} - y_{Lj}), \quad c_{ij} = \left(\frac{x_{Li}^2 + y_{Li}^2 - x_{Lj}^2 - y_{Lj}^2 - (r_{Li}^2 - r_{Lj}^2)}{2} \right)\end{aligned}\tag{2.4-2}$$

Each of these M equations represents the straight line formed by joining the intersection points of the circles defined in (2.4-1). This is shown in Figure 2.4-4 for $m_L = 3$. Since the range estimates are noisy, in general $r_{Li} \neq R_{Li}$, solving these equations simultaneously may not yield a solution. Therefore, we resort to an error minimization approach. Let $\hat{\mathbf{x}} = [\hat{x} \ \hat{y}]^T$ represent the estimate of the node's location. Then, for every potential solution \mathbf{x} , and for every equation, we can define a measure of the error as:

$$e_{ij} = a_{ij}x + b_{ij}y - c_{ij}, \quad i, j = 1, 2, \dots, m_L, \quad j > i\tag{2.4-3}$$

The final estimate $\hat{\mathbf{x}} = [\hat{x} \ \hat{y}]^T$ can be selected such that an objective function Z is minimized:

$$\hat{\mathbf{x}} = \arg \min_{\mathbf{x}} Z(x, y) = \arg \min_{\mathbf{x}} \sum_{i=1}^{m_L} \sum_{j>i}^{m_L} e_{ij}^2\tag{2.4-4}$$

This is the equivalent to the total least squares (TLS) approach. It is important to note that the objective function Z is non-linear. The TLS solution is given by

$$\hat{\mathbf{x}} = (\mathbf{A}^T \mathbf{A})^{-1} \mathbf{A}^T \mathbf{c},\tag{2.4-5}$$

where

$$\mathbf{A} = \begin{bmatrix} a_{12} & b_{12} \\ a_{13} & b_{13} \\ \vdots & \vdots \\ a_{1m_L} & b_{1m_L} \\ a_{23} & b_{23} \\ \vdots & \vdots \\ a_{(m_L-1)m_L} & b_{(m_L-1)m_L} \end{bmatrix}, \quad \mathbf{c} = \begin{bmatrix} c_{12} \\ c_{13} \\ \vdots \\ c_{1m_L} \\ c_{23} \\ \vdots \\ c_{(m_L-1)m_L} \end{bmatrix}.$$

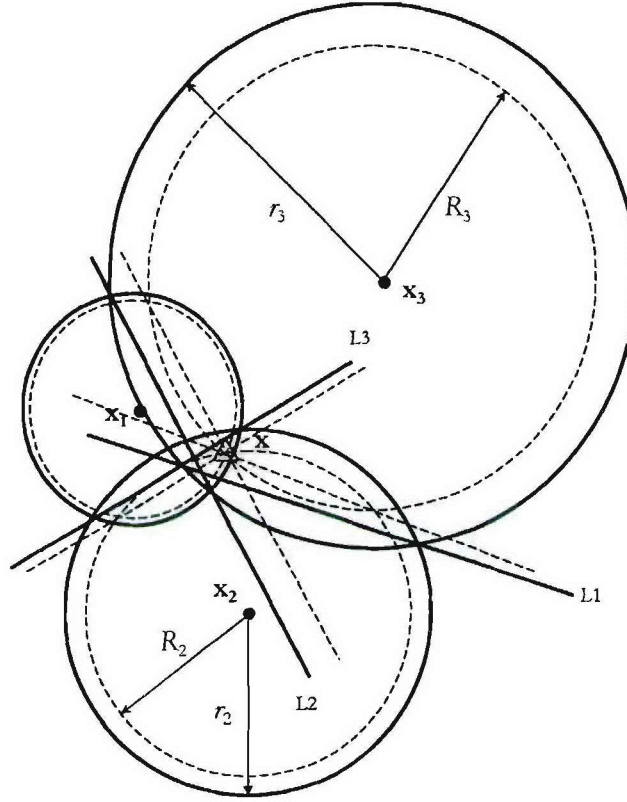


Figure 2.4-4 Linearization of LOS range equations, with $m_L = 3$. L1, L2 and L3 are the three lines formed by connecting the intersection of the three circles. Note this since the ranges are noisy, L1, L2 and L3 do not intersect at \mathbf{x} .

We see from (2.4-2) that the set of variables $\{e_{ij}\}$ plays the role of unconstrained slack variables [9] in each of the M equations. This system of equations can be converted to a linear program if the objective function Z is linear. If we define

$$Z = \sum_i^{m_L} \sum_{j,j>i}^{m_L} |e_{ij}| \quad (2.4-6)$$

and replacing the unconstrained variable e_{ij} by $e_{ij} = e_{ij}^+ - e_{ij}^-$, $e_{ij}^+, e_{ij}^- \geq 0$, we can write the *linear* objective function to be minimized as

$$Z = \sum_i^{m_L} \sum_{j>i}^{m_L} (e_{ij}^+ + e_{ij}^-) \quad (2.4-7)$$

It must be noted that in the optimal solution, only one of e_{ij}^+, e_{ij}^- will be positive and the other will be zero. The constraints are then given by

$$a_{ij}x + b_{ij}y + e_{ij}^+ - e_{ij}^- = c_{ij}, \quad i, j = 1, 2, \dots, m_L, j > i \quad (2.4-8)$$

Let \mathbf{e} denote the vector of $2M$ slack variables:

$$\mathbf{e} = \begin{bmatrix} e_{12}^+ \\ e_{12}^- \\ e_{13}^+ \\ e_{13}^- \\ \vdots \\ e_{(m_L-1)m_L}^+ \\ e_{(m_L-1)m_L}^- \end{bmatrix} \quad (2.4-9)$$

Defining $\mathbf{z} = [x \ y \ \mathbf{e}^T]^T$ as the vector of $(2M + 2)$ variables, the linear program (LP) can be formulated in *standard form* as

$$\begin{aligned} \min Z &= \mathbf{f}_L^T \mathbf{z} \quad \text{such that} \\ [\mathbf{A} \ \mathbf{J}] \mathbf{z} &= \mathbf{c} \\ \mathbf{z} &\geq \mathbf{0} \end{aligned} \quad (2.4-10)$$

where \mathbf{A} and \mathbf{c} were defined in (2.4-5),

$$\mathbf{J} = \begin{bmatrix} -1 & 1 & 0 & 0 & \dots & \dots & 0 & 0 \\ 0 & 0 & -1 & 1 & \dots & \dots & 0 & 0 \\ \vdots & \vdots & \dots & \dots & \dots & \ddots & \ddots & \vdots \\ 0 & 0 & 0 & 0 & 0 & \dots & -1 & 1 \end{bmatrix}_{M \times 2M}$$

and $\mathbf{f}_L = [\mathbf{0}_{2 \times 1}^T \ \mathbf{1}_{2M \times 1}^T]$, where $\mathbf{0}_{k \times l}$ represents a $k \times l$ matrix of zeros and $\mathbf{1}_{k \times l}$ represents a $k \times l$ matrix of ones. Figures 2.4-5 and 2.4-6 compare the mean and standard deviation of the location error $\Omega = \|\mathbf{x} - \hat{\mathbf{x}}\|^2$ averaged over several range measurement noise realizations obtaining using the (i) LS estimator and (ii) the LP approach. We see that the linearization of the objective function has negligible impact on performance.

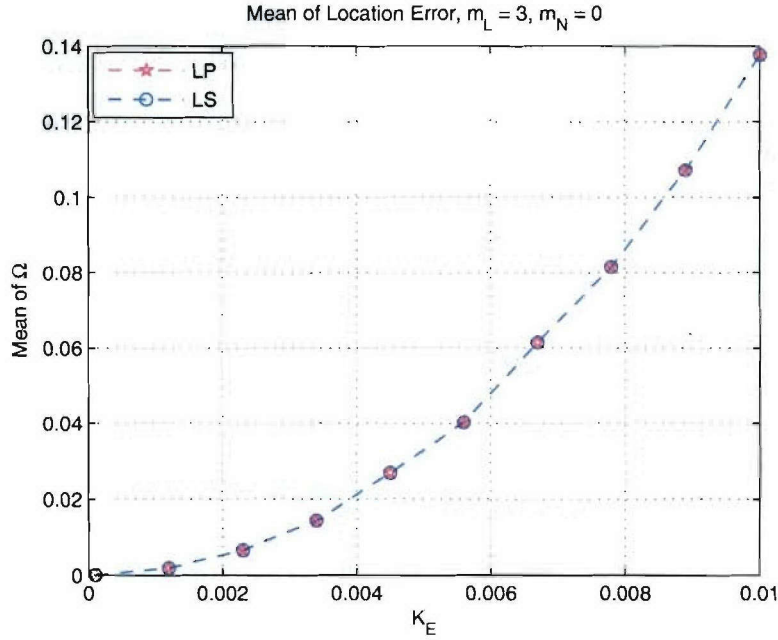


Figure 2.4-5 Mean of the Localization Error Ω , $m_L = 3$, $m_N = 0$ versus the proportionality constant K_E for a specific distribution of anchors.

NLOS ranges

The TLS method described previously, when applied directly to NLOS ranges, can potentially lead to large errors. Since the bias errors on the NLOS ranges are always positive, we convert the NLOS range information into inequalities:

$$\begin{aligned} \|\mathbf{x} - \mathbf{x}_i\| &\leq r_{Ni}, \quad i = 1, 2, \dots, m_N \\ (x - x_i)^2 + (y - y_i)^2 &\leq r_{Ni}^2 \end{aligned} \quad (2.4-11)$$

These inequalities imply that the feasible region for \mathbf{x} lies in the interior of the circles defined by (2.4-11). As the bias errors are large and positive, the true location \mathbf{x} is within this feasible region with high probability. Note that this assumption cannot be made if the standard deviation of the zero-mean measurement noise and the positive bias are comparable. Once again, these are non-linear constraints on x and y . However, these constraints can be relaxed to the following linear constraints:

$$\begin{aligned} x - x_i &\leq r_{Ni}, \\ -x + x_i &\leq r_{Ni}, \\ y - y_i &\leq r_{Ni}, \\ -y + y_i &\leq r_{Ni}, \quad i = 1, 2, \dots, m_N. \end{aligned} \quad (2.4-12)$$

This essentially relaxes the circular constraints to rectangular constraints as shown in Figure 2.4-6. It is readily seen that the new rectangular feasible region contains the original feasible region formed by the intersection of three circular regions.

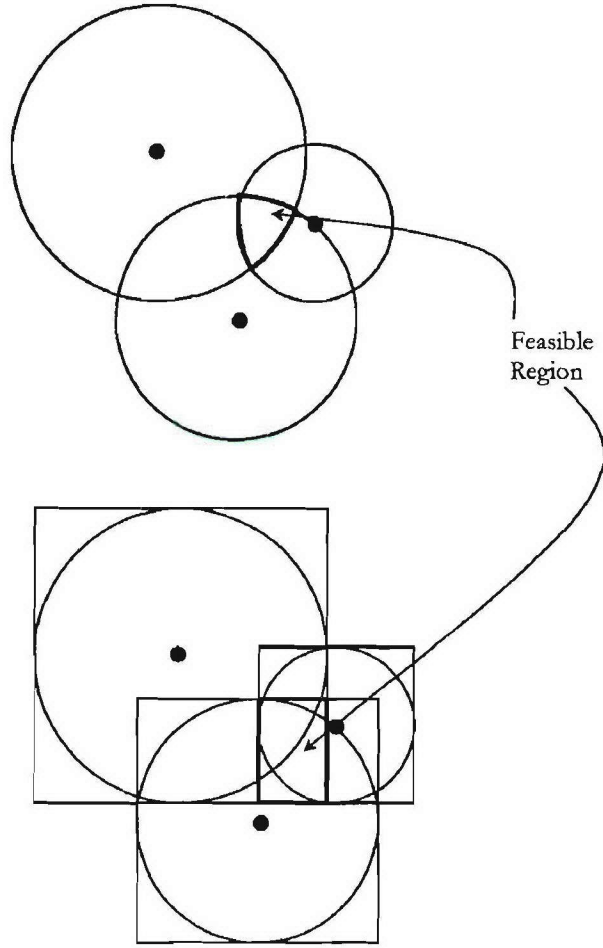


Figure 2.4-6 Linearization of NLOS constraints; the NLOS non-linear circular constraints are relaxed to rectangular linear constraints.

Writing the above constraints for the i th NLOS range in standard form

$$\begin{aligned}
 x - x_i + u_{1i} &= r_{Ni}, \\
 -x + x_i + u_{2i} &= r_{Ni}, \\
 y - y_i + v_{1i} &= r_{Ni}, \\
 -y + y_i + v_{2i} &= r_{Ni}, \\
 u_{1i}, u_{2i}, v_{1i}, v_{2i} &\geq 0, \quad i = 1, 2, \dots, m_N.
 \end{aligned} \tag{2.4-13}$$

Defining $\mathbf{w}_i = [u_{1i} \ u_{2i} \ v_{1i} \ v_{2i}]^T$ and $\mathbf{z}_i = [x \ y \ \mathbf{w}_i^T]^T$ as the vector of variables for the i th NLOS range estimate, we can express the above equations in matrix form

$$\begin{aligned}
 \begin{bmatrix} \mathbf{B}_1 & \mathbf{I}_{4 \times 4} \end{bmatrix} \mathbf{z}_i &= \mathbf{r}_i \\
 \mathbf{z}_i &\geq \mathbf{0}
 \end{aligned} \tag{2.4-14}$$

where

$$\mathbf{B}_i = \begin{bmatrix} -1 & 0 \\ 1 & 0 \\ 0 & -1 \\ 0 & 1 \end{bmatrix}_{4 \times 2}, \quad \mathbf{r}_i = \begin{bmatrix} r_{Ni} + x_{Ni} \\ r_{Ni} - x_{Ni} \\ r_{Ni} + y_{Ni} \\ r_{Ni} - y_{Ni} \end{bmatrix}$$

Conclusions

It was shown that we can formulate the problem of solving for a node's location, given either LOS and NLOS range estimates from location-aware anchors, as a linear programming problem. In the case where we are given a mixture of LOS and NLOS estimates, using the above formulation, we see that the LOS range estimates determine the objective function for the linear program, and the NLOS range estimates constrain the feasible region for the problem.

References

- [1] T. Silventoinen and M. Rantalainen, "Mobile station emergency locating in GSM," in *1996 IEEE International Conference on Personal Wireless Communications*, pp. 232–238, Feb. 19–21 1996.
- [2] J. Borras, P. Hatrack, and N. B. Mandayam, "Decision theoretic framework for NLOS identification," in *1998 Vehicular Technology Conference, (VTC '98)*, vol. 2, pp. 1583–1587, May. 18–21 1998.
- [3] Y. Qi and H. Kobayashi, "Cramer-Rao lower bound for geolocation in nonline-of-sight environment," in *Proceedings of ICASSP 2002*, vol. 3, pp. III–2473–III–2476, May 2001.
- [4] J. J. Caffery, "A new approach to the geometry of TOA location," in *2000 IEEE Vehicular Technology Conference*, vol. 4, pp. 1943–1949, September 2000.
- [5] E. G. Larsson, "Cramer-Rao bound analysis of distributed positioning in sensor networks," *IEEE Signal Processing Letters*, vol. 11, pp. 334–337, March 2004.
- [6] L. Doherty, K. S. J. Pister, and L. E. Ghaoui, "Convex position estimation in wireless sensor networks," in *Proceedings of INFOCOM 2001*, vol. 3, pp. 1655–1663, April 2001.
- [7] X. Wang, Z. Wang, and R. O'Dea, "A TOA-based location algorithm reducing the errors due to non-line-of-sight (NLOS) propagation," *IEEE Transactions on Vehicular Technology*, vol. 52, pp. 112–116, January 2003.
- [8] P.-C. Chen, "A non-line-of-sight error mitigation algorithm in location estimation," in *Wireless Communications and Networking Conference 1999*, vol. 1, pp. 316–320, Sept. 21–24th 1999.
- [9] B. M. P. Fraticelli, *Course Notes: Optimization*. 2004. ISE 5405, Virginia Tech.

2.4.1.2 Subtask 2.4.1b Cross-Layer Design of Cooperative UWB Networks

Summary: Based on the accomplishments from the second quarter, we focused on rate-adapted UWB cross layer design. First, three different UWB signature sequence design strategies are introduced into UWB systems to improve link performance. Both analytic expressions and simulation results are derived for centralized and non-centralized UWB systems, respectively. Second, the three signature sequence designs are included in a UWB cross-layer design. Overall system utility is examined for decentralized networks via simulation using the two different scheduling approaches and two different routing protocols (Minimum Energy Routing (MER) and Direct Routing (DIR)). Finally, conclusions based on the simulation results are provided and future research directions are discussed.

Accomplishments during reporting period: Consider M nodes communicating with M corresponding receivers. The transmission of each user is assumed to be sequence-based, and that received signals are roughly synchronized (this assumption will be relaxed later). Let H_{ki} be the channel matrix from the k^{th} user to the i^{th} receiver:

$$H_{m \times n} = \begin{bmatrix} h_0 & 0 & \cdots & 0 \\ h_1 & h_0 & \cdots & 0 \\ \vdots & \vdots & \ddots & \vdots \\ h_{N_x-1} & h_{N_x-2} & \cdots & h_0 \\ 0 & h_{N_x-1} & \cdots & h_1 \\ \vdots & \vdots & \ddots & \vdots \\ 0 & 0 & \cdots & h_{N_x-1} \end{bmatrix} \quad (2.4-15)$$

Let p_k be the signal power, X_k be the transmit sequence vector and b_k be the data bit transmitted by the k^{th} user, respectively. The received signal vector after pulse matched filtering but before the sequence matched filter is given by:

$$r_i = \sum_{k=1}^M \sqrt{p_k} H_{ki} X_k b_k + n \quad (2.4-16)$$

where n is a vector of zero-mean Gaussian random variables with variance $\sigma^2 = \frac{N_0}{2}$.

For one transmit/receive pair, given the channel $H_{m \times n}$, if the transmit sequence vector X_k is chosen to be the eigen-vector corresponding to the maximum eigen-value of channel matrix $H^T H$, the transmit sequence X_k maximizes the SNR by coherently combining the large number of multipath components prior to reception. This sequence is denoted by s_k . From a matched filter perspective, the correlation template is the product of HX_k , which equals to HS_k for this case.

For a multi-access system, the interference vector can be written as $I_k = \sum_{\substack{j=1 \\ k \neq j}}^{N-1} \sqrt{p_j} \hat{H}_{ji} X_j b_j$ and

the interference-plus-noise matrix is defined as:

$$Z_k = I_k * I_k^T + \sigma^2 \mathbf{I} \quad (2.4-17)$$

where \mathbf{I} is the identity matrix. Now if X_k is the eigen-vector corresponding to the maximum eigen-value of the matrix $H_{kk}^T Z_k^{-1} H_{kk}$, X_k can be rewritten as s_z , and is the maximum SINR sequence. To form an MMSE receiver, the unit-energy correlation template is equal to the product of $Z_k^{-1} H_{kk} X_k$.

SINR of Centralized Systems

For a centralized system, M users communicate with a fixed receiver. Let C_i be the unit-energy correlation template vector for the i^{th} user. The signal after correlation can be represented as:

$$C_i^T r = C_i^T \sqrt{p_i} H_i X_i b_i + C_i^T \sum_{\substack{j=1 \\ j \neq i}}^{M-1} \sqrt{p_j} H_j X_j b_j + C_i^T n \quad (2.4-18)$$

and where I_i written as $I_i = \sum_{j \neq i}^{M-1} \sqrt{p_j} H_j X_j b_j$. Using equation (2.4-17), the output SINR of the i^{th} user can be written as:

$$SINR_i = \frac{p_i (C_i^T H_i X_i X_i^T H_i^T C_i)}{C_i^T Z_i C_i} \quad (2.4-19)$$

Given the channel matrix $H_i^T H_i$, which is a Hermitian matrix, it can be decomposed using SVD:

$$H_i^T H_i = P \Sigma P^T \quad (2.4-20)$$

where P is a unitary matrix, $\Sigma = \begin{bmatrix} \lambda_1^i & & \\ & \lambda_2^i & \\ & & \ddots \\ & & & \lambda_s^i \end{bmatrix}$, and λ_s^i is the maximum eigen-value of the i^{th} channel matrix, and $\lambda_1^i < \lambda_2^i < \dots < \lambda_s^i$.

Again applying the SVD, the i^{th} channel H_i can be expressed as

$$H_i = U^i \Sigma^{\frac{1}{2}} P^T \quad (2.4-21)$$

where U^i is a unitary matrix with size m -by- n .

Now if the correlator at the receiver is a matched filter, it can be simplified as:

$$H_i s_i = U^i \Sigma^{\frac{1}{2}} P^T s_i = U^i \begin{bmatrix} 0 \\ \dots \\ \sqrt{\lambda_s^i} U_s^i \end{bmatrix} = \sqrt{\lambda_s^i} U_s^i \quad (2.4-22)$$

where U_s^i is the s^{th} column of channel matrix U^i .

Furthermore, assuming the interferers are uncorrelated and every node uses the optimal SNR sequence, the transpose of channel matrix $H_i^T H_i$ and interference-plus-noise matrix Z_i are given by:

$$H_i H_i^T = U \Sigma U^T \quad (2.4-23)$$

$$Z_i = \sum_{j \neq i; j=1}^M p_j H_j s_j s_j^T H_j^T + \sigma^2 I = \sum_{j \neq i; j=1}^M \lambda_s^j p_j U_s^j (U_s^j)^T + \sigma^2 I \quad (2.4-24)$$

We will examine the following three cases which use the above sequences:

- (i) All concurrent channels transmit using the maximum SNR sequence using a matched filter correlator at the receiver.

Given s_i is the maximum eigen-vector of the channel matrix $H_i^T H_i$ and the correlation template $C_i = H_i s_i$, the output SINR of i^{th} user is:

$$\text{SINR}_i = \frac{p_i (C_i^T H_i X_i X_i^T H_i^T C_i)}{C_i^T Z_i C_i} = \frac{p_i \lambda_s^i}{(U_s^i)^T \left\{ \sum_{j \neq i, j=1}^M \lambda_s^j p_j U_s^j (U_s^j)^T \right\} U_s^i + \sigma^2} \quad (2.4-25)$$

(ii) One user (i^{th}) transmits using the maximal SINR sequence, while the remaining concurrent transmitters use the maximum SNR sequence and the matched filter receiver.

$$H^T Z^{-1} H s_z = \lambda_z s_z \quad (2.4-26)$$

For i^{th} channel, the transmit sequence is s_z , defined by (2.4-26), and the correlation template is $Z_i^{-1} H_i s_z$. The SINR of i^{th} channel is :

$$\text{SINR}_i = \frac{p_i (C_i^T H_i X_i X_i^T H_i^T C_i)}{C_i^T Z_i C_i} = p_i s_i^T H_i^T Z_i^{-1} H_i s_i = p_i \lambda_z^i \quad (2.4-27)$$

However, since the signature of the i^{th} channel has changed, the SINR of the other concurrent channels need to be recalculated:

$$\frac{1}{\text{SINR}_k^*} = \frac{1}{\text{SINR}_k} + \frac{(U_s^j)^T p_i H_i s_z s_z^T H_i^T U_s^j - \lambda_s^i p_i (U_s^j)^T U_s^i (U_s^i)^T U_s^j}{P_j \lambda_s^j} \quad (2.4-28)$$

where SINR_k is obtained from (2.4-25).

(iii) All concurrent transmissions use the maximum SNR sequence, with an MMSE receiver. Transmit sequence s_i remains the maximum eigen-vector of the channel matrix $H_i^T H_i$. However, the correlation template switches to $Z_i^{-1} H_i s_z$.

$$\text{SINR}_i = p_i s_i^T H_i^T Z_i^{-1} H_i s_i = p_i \lambda_s^i (U_m^i)^T Z^{-1} (U_m^i) < p_i \lambda_z^i \quad (2.4-29)$$

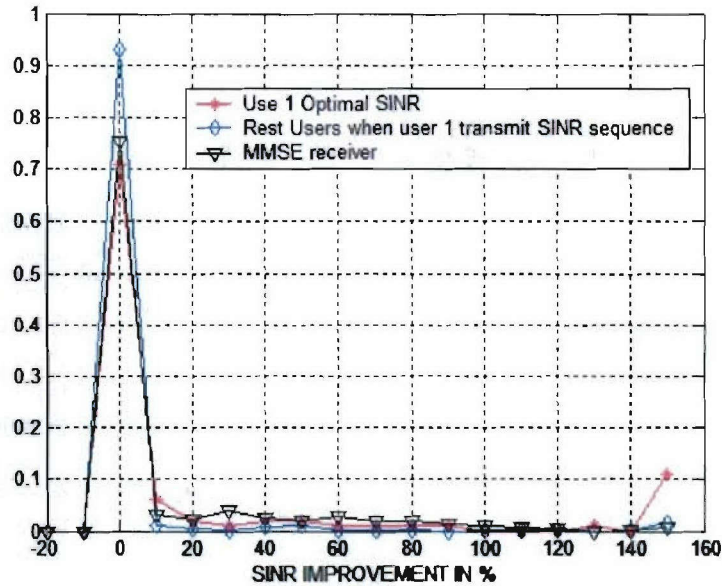
Performance: The performance of these three algorithms was tested via simulation using indoor non-line of sight (NLOS) channel measurements taken at the Mobile and Portable Radio Research Group (MPRG) at Virginia Tech. It is notable that the performance of algorithm (i) is normalized to unity for the same basis of comparison. The baseline performance of this algorithm was discussed in the previous quarterly report and is presented in two recent publications. Without a loss of generality, user 1 is always chosen to be the node that transmits using the maximum SINR sequence in algorithm (ii). The performance of the algorithms in a centralized system with perfect power control and a sequence length of 160 is shown in Figure 2.4-7. The x-axis is the SINR improvement in percentage compared to algorithm (i).

The red line is the output SINR of user 1 when it adopts algorithm (ii). Correspondingly, the blue curve shows the SINR of the rest of the users when user 1 adopts algorithm (ii). It can be shown that the blue curve has some probability of being negative, which indicates that the performance of other users is degraded when user 1 chooses algorithm (ii). However, the histogram shows that positive gains are more frequent.

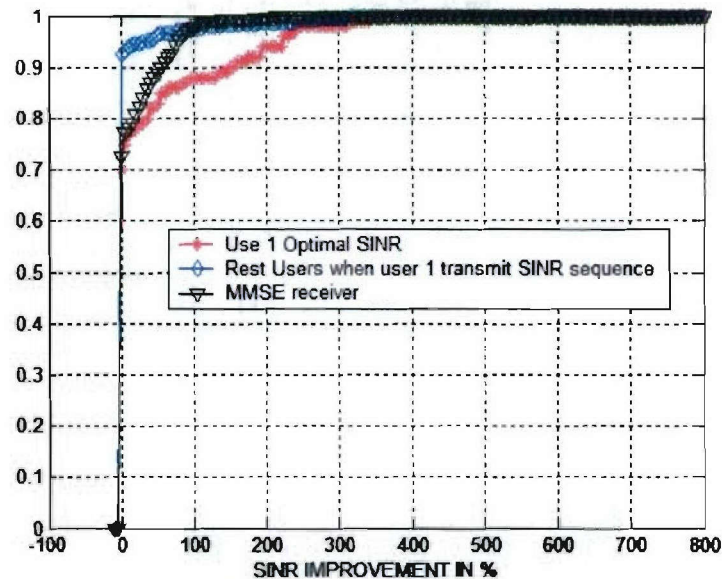
Furthermore, the performance of algorithm (iii) (all users transmit using the maximum SNR sequences and use MMSE receivers) always improves. However, for user 1, using algorithm (ii)

(Red) always provides better performance than algorithm (iii) (Black). It can be concluded using proactive interference avoidance is superior to interference mitigation at the receiver: The difficulty is that if only one user adapts its sequence for interference avoidance, the other users are not guaranteed to have better performance. Using inequalities to represent the relative relationship among the algorithms:

$$\begin{aligned} \text{algorithm ii} &> \text{algorithm iii} > \text{algorithm i (user one)} \\ \text{algorithm iii} &\geq \text{algorithm ii} > \text{algorithm i. (other users)} \end{aligned} \quad (2.4-30)$$



(a) PDF of gains in a centralized system (perfect power control)



(b) CDF of plot(a)

Figure 2.4-7 Histogram of the gains over the maximum SNR sequence for the three algorithms in centralized UWB systems. Red: Performance of user 1 when it transmits using maximum SINR sequence. Blue: Performance of the rest of the concurrent users

corresponding to Red curve. Black: all users transmit using the maximum SNR sequence with an MMSE receiver.

Non-Centralized Systems

The SINR of the non-centralized system is analogous to the centralized system, although now

$I_i = \sum_{j \neq i}^{N-1} \sqrt{p_j} \hat{H}_{ji} s_j b_j$. Additionally, since s_j is no longer the eigen-vector of $(\hat{H}_{ji})^T \hat{H}_{ji}$, the SINR does not have a relatively simple expression. Again, returning to the three cases examined:

- (i) All concurrent channels transmit using the maximum SNR sequence using a matched filter correlator at the receiver.

$$SINR_i = \frac{p_i (\lambda_s^i)^2}{C_i^T Z_i C_i} \text{ where } C_i = H_{ii} s_i \quad (2.4-31)$$

- (ii) One user (i^{th}) transmits using the maximal SINR sequence, while the remaining concurrent transmitters use the maximum SNR sequence and the matched filter receiver.

For the i^{th} channel, the transmit sequence is s_z , the maximum eigen-vector of $H_{ii}^T Z_i^{-1} H_{ii}$, the correlation template is $Z_i^{-1} H_{ii} s_z$. For the rest of the channels, the transmit sequence is s_k , the maximum eigen-vector of $H_{kk}^T H_{kk}$, and its corresponding matched filter is $H_{kk} s_k$.

$$SINR_i = P_i \lambda_z^{ii} \quad (2.4-32)$$

And it is notable that the SINR of the rest of the nodes is derived using (2.4-19).

- (iii) All concurrent channels transmit optimal SNR sequence, with MMSE receiver.

For i^{th} channel, the transmit sequence is s_i , the maximum eigen-vector of $H_{ii}^T H_{ii}$, the correlation template is $Z_i^{-1} H_{ii} s_i$. The SINR is obtained using (2.4-19), and it obeys

$$SINR_i < P_i \lambda_z^{ii} \quad (2.4-33)$$

Performance: The relative performance of the algorithms is given in Figure 2.4-8. All algorithms exhibit similar trends as in the centralized system. However, it is notable, the performance degradation of the concurrent channels, when one channel is randomly chosen to transmit optimal SINR sequence, is not as severe as in the centralized system (blue). This is likely due to the random distribution of the nodes. Therefore, compared to the centralized case, due to near-far issue for all users, algorithm (ii) has the potential to greatly enhance the system utility as we will see.

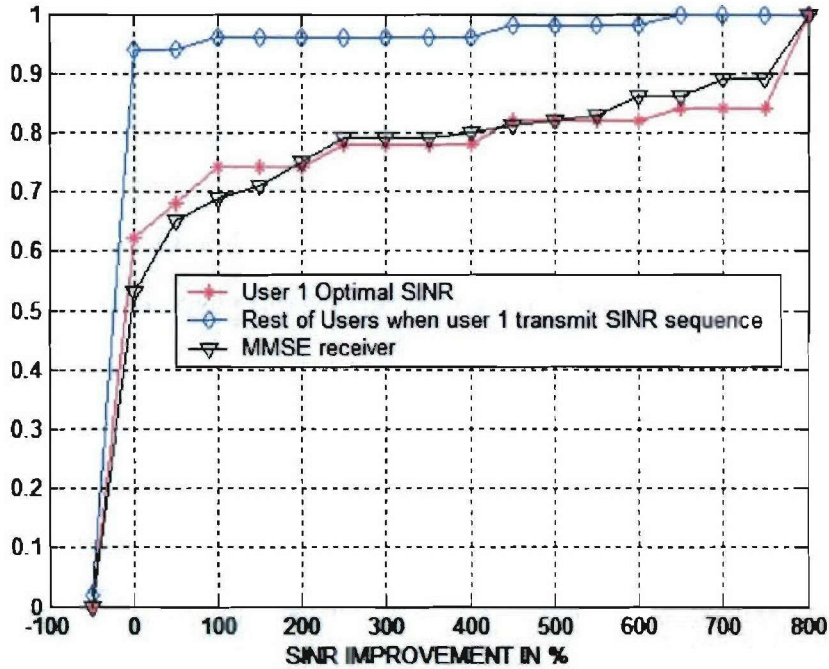


Figure 2.4-8 Cumulative histogram of the three algorithms for a non-centralized UWB system. Red: Performance of user 1 when it transmits the maximum SINR sequence. Blue: Performance of the other concurrent users when user 1 users the optimal SINR sequence. Black: all users transmit using the maximum SNR sequence with the MMSE receiver.

Cross Layer Design

Two routing protocols were examined in the Quarter 2 report for cross-layer design. The first is simple direct routing (DIR) which is a single hop routing protocol. The second, minimum energy routing protocol (MER) is a dynamic multi-hop protocol which minimizes the energy cost function. Additionally, two scheduling strategies are examined. The first is to allow all nodes to transmit simultaneously. The second is to create an exclusion region around each receiver to control the interference level while each node is receiving data. The optimization problem can be written as:

$$\begin{aligned}
 & \text{Max} \quad \sum_{i=1}^I \log(f^i) \\
 & Bf^n \leq \sum_{n=1}^{L+1} w_n r^n \\
 & r_l^n = K * SINR_l^n \\
 & \sum_{n=1}^{L+1} w_n = 1 \\
 & \sum_{l: l.src=0} 1_{\{p_l^n > 0\}} + \sum_{l: l.des=0} 1_{\{p_l^n > 0\}} \leq 1 \\
 & P_l^n \leq P_l^{MAX}
 \end{aligned} \tag{2.4-34}$$

where n, l, B, f, r represent the time slot, link, routing matrix, flow and data rate respectively, w is the duration of the time slots, and P is the power of each node. We assume that the network size is one by one and that all nodes are uniformly distributed in this area. For a centralized system, the base station is in the center of the network area. The optimization routine was run several

times using measured channel data and the resulting utility was recorded for each combination of scheduling, routing and sequence optimization. The results for a centralized system are shown in Table 2.4-1 and for a non-centralized system are shown in Table 2.4-2.

Table 2.4-1 Total utility under different scheduling, routing for UWB centralized system

UTILITY		Max SINR	Max SNR	opt SNR +MMSE
All sending together-Scheduling I	DIR	10.8527	11.4167	11.5837
	MER	60.6695	54.1896	60.4500
Optimal exclusion region-Scheduling II	DIR	48.2401	44.9446	47.6627
	MER	48.3990	44.3770	48.3521

Table 2.4-2 Total utility under different scheduling, routing for UWB non-centralized system

UTILITY		Max SINR	Max SNR	opt SNR +MMSE
All sending together-Scheduling I	DIR	82.1908	36.5402	74.4397
	MER	98.6433	59.0727	92.6078
Optimal exclusion region-Scheduling II	DIR	104.8049	84.9088	101.3306
	MER	112.4473	85.6227	101.6242

Conclusions: For both the centralized and non-centralized UWB system, the performance of the two routing protocols is close when an exclusion region is maintained to control the interference levels. Without the exclusion region, the MER protocol always performs substantially better than DIR routing regardless of sequence optimization.

- Furthermore, using either the maximum SINR sequence or using MMSE receivers achieves similar performance in a centralized system, regardless of routing or scheduling. However, this is not true for a non-centralized system, where active interference avoidance is superior.
- For centralized systems, without the exclusion region, the MER routing provides the best performance no matter which signature sequence is transmitted. Furthermore, the results indicate that no exclusion region is required for centralized scenarios, provided that some type of interference avoidance or mitigation is used.
- For a non-centralized system, without an exclusion region, the performance can be substantially worse.

2.4.1.3 Subtask 2.4.1c Cross-Layer Design of Cooperative Networks through Distributed Beamforming

Introduction: Energy and cost efficient data transmission are fundamental issues in sensor networks. One approach to these problems is distributed beamforming using a cluster of nodes to achieve performance gain. In order to understand the requirements in distributed beamforming with multiple nodes, beamforming with a standard antenna array, which will be referred to as centralized beamforming, will be presented briefly. We focus on transmit beamforming with multiple antennas since distributed beamforming is one variation of centralized transmit beamforming. To simplify the analysis the number of transmit antennas is assumed to be two, and the channel coefficient from i^{th} antenna at the transmitter to the receiver, h_i , is static during the data transmission time. We also assume that the transmitter performs closed-loop transmit beamforming using known channel information. At the transmitter, the transmit signal is compensated by the channel coefficients of each antenna. The propagation delay from each transmit antenna can be assumed to be same since the distance between transmit antennas is short enough as compared to the distance between the transmitter and receiver. Also, the transmit signals have the same carrier phase using a single local oscillator. Figure 2.4-9 shows the centralized closed-loop transmit beamforming. Then, the received signal can be expressed by

$$\begin{aligned} y(t) &= h_1 h_1^* s(t - \tau) \cos(\omega t + \theta) + h_2 h_2^* s(t - \tau) \cos(\omega t + \theta) + n(t) \\ &= (|h_1|^2 + |h_2|^2) s(t - \tau) \cos(\omega t + \theta) + n(t) \end{aligned} \quad (2.4-35)$$

In (2.4-35), we can achieve the beamforming gain based on the following assumptions: 1) the baseband signal, $s(t)$, is synchronized at each transmit antenna and 2) the carrier frequency and phase are same for all antenna elements. These requirements can easily be achieved in centralized beamforming with the common circuits. However, these are challenging problems in distributed beamforming.

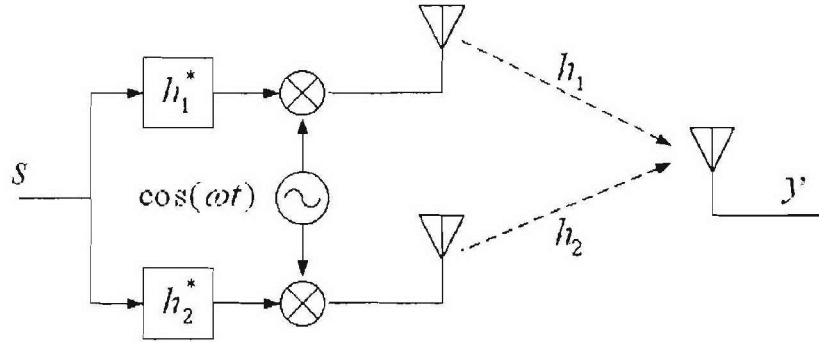


Figure 2.4-9 Centralized transmit beamforming with 2x1 antenna array.

Figure 2.4-10 shows an example of distributed beamforming with K nodes in a cluster. Usually the cluster consists of multiple nodes that are located close to the source. The source broadcasts the data to the nodes in a cluster and they coordinate their transmission to achieve the beamforming gain.

Figure 2.4-11 illustrates the effects of phase offset and baseband synchronization. In the configuration of Figure 2.4-10, we assume that R is 3 m, $d = 30$ m, baseband signal is 2 Mbps which is modulated with BPSK, carrier frequency is 1 GHz, and SNR is 5 dB. We use two nodes in a cluster and the distances to the destination are 30.2 m and 27.51 m, respectively. Figures 2.4-11 (a) and (b) show the situation when the signals from two nodes are combined destructively at

the destination due to the phase offset difference. If each node knows the distance to the destination, the phase offset due to the distance can be calculated and compensated at each node. Figures 2.4-11 (c) and (d) show the gain with the compensated phase offset at each node. However, the finding of accurate distance between nodes is a challenging problem in sensor networks. Therefore, we will present other methods to achieve the beamforming gain at the receiver. Note that the baseband synchronization can be ignored at the receiver if the baseband symbol duration is large enough compared to the difference of propagation delays from the nodes. In example of Figure 2.4-11, the baseband symbol duration is 500 ns and the difference of propagation delays of two nodes is about 9 ns.

Carrier phase synchronization

As mentioned earlier, the propagation delay can be ignored if it is small enough compared to baseband symbol duration. Henceforth, we assume that the synchronization of baseband signal is achieved. We also assume that carrier frequency is synchronized at all nodes in the network. Even though carrier frequencies at all transmitters are synchronized, the synchronization of carrier phase offset cannot be guaranteed at the receiver due to the different channel and propagation delay for each receiving signal. We will present three methods to reduce the effect of carrier phase offset.

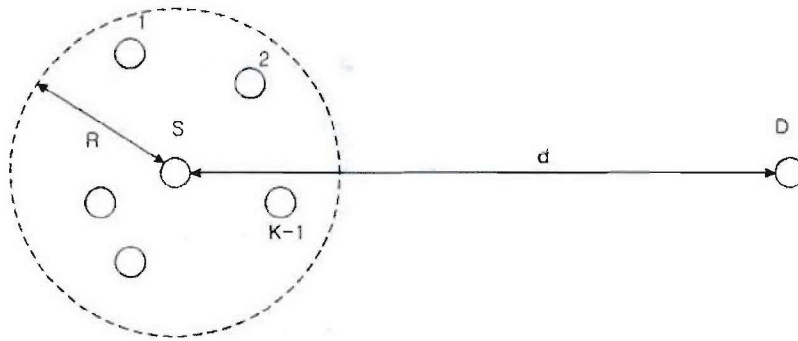
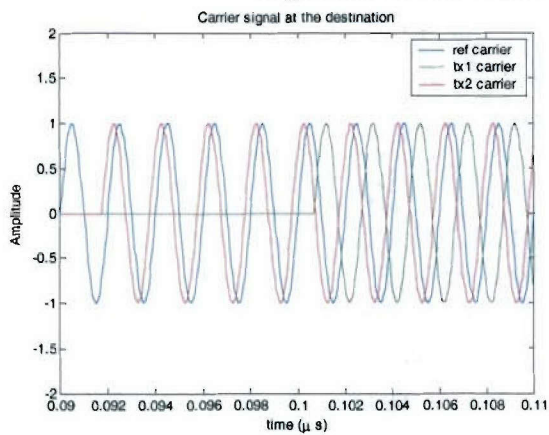
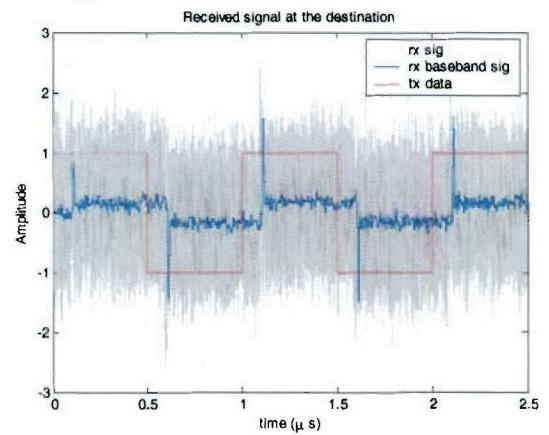


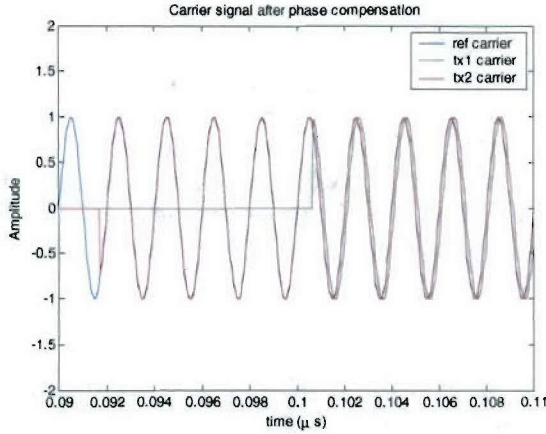
Figure 2.4-10 Distributed beamforming with K nodes.



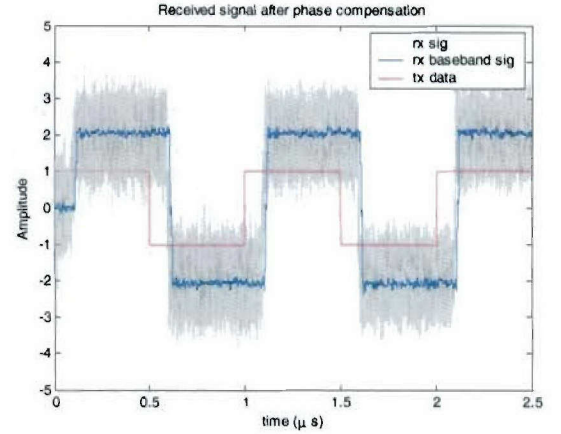
(a)



(b)



(c)



(d)

Figure 2.4-11 Example of carrier phase effects in a distributed beamforming

Random phase selection: At the initial stage of distributed beamforming, proper combination of phase at the transmitters will be searched for a certain time interval. Each transmitter chooses one phase value randomly which are divided uniformly into N points. If the received power with the selected phase values is greater than the previous received power, the reference power at the receiver is replaced with the current received power and an indication flag is sent to the transmitters. If the transmitters receive the indication flag, the current phase values are stored and the random phase selection process is repeated. After finishing the phase selection procedure, the selected phase set will be used for data transmission. The details of this method are as follows.

Transmit the signal with random phase (PO_1) at each transmitter

Measure the received power P_1 and set as $P_{max} = P_1$

While $n \leq \#$ of feedback

Transmit the signal with random phase, PO_n

Measure the received power P_n

If $P_n > P_{max}$

$P_{max} = P_n$

feedback with 1

else

feedback with 0

if feedback is 1

$PO = PO_n$

end while

Use PO as transmit phase offset

Phase compensation with feedback: If the transmitter can extract the channel from the feedback signal, better performance can be achieved by channel compensation at the transmitter. This method is similar to the centralized closed-loop transmit beamforming. Note that the extracted channel from the feedback signal includes the carrier phase offset information. Therefore, the phase offset compensation can be achieved by the channel compensation. An example of a distributed beamforming with two nodes is shown in Figure 2.4-12. Let y_1 and y_2 be the received signals at the destination from node 1 and node 2, respectively. Then, the received signals at the destination are given by

$$\begin{aligned}
y_1(t) &= h_1 h_1^* s(t-\tau) \cos(\omega t + \theta') = |h_1|^2 s(t-\tau) \cos(\omega t + \theta') \\
y_2(t) &= h_2 h_2^* s(t-\tau) \cos(\omega t + \theta') = |h_2|^2 s(t-\tau) \cos(\omega t + \theta')
\end{aligned}
\tag{2.4-36}$$

where τ is the propagation delay from the nodes to the destination, and θ' is the carrier phase of the receiving signal. A short summary of this method follows.

1. One node in a cluster, usually the source, transmits control message to the destination to indicate the start of distributed beamforming
2. Destination responds with reference signal
3. All nodes in a cluster extract channel information
4. Transmit signal after compensating channel

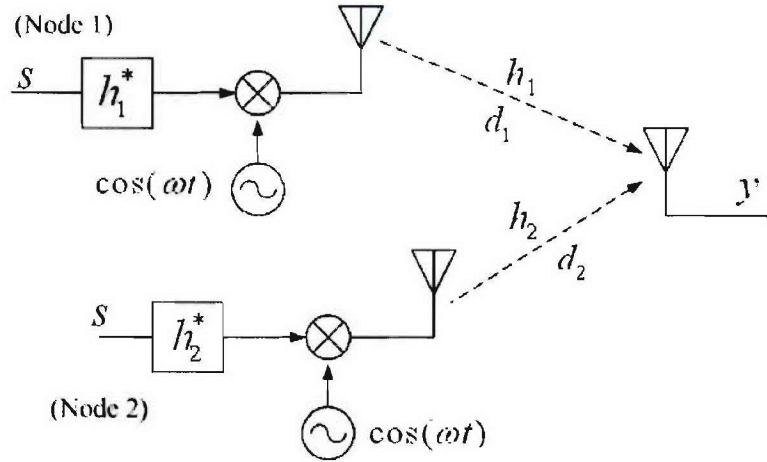


Figure 2.4-12 Distributed transmit beamforming with two nodes.

Figure 2.4-13 shows the simulation results with random phase selection and channel compensation methods. The number of nodes in a cluster is 4, and the number of phase selection points in random phase selection algorithm is 20 and 50 for the upper and the lower figures, respectively. To check the convergence to the proper phase selection, the results with 20 and 50 iterations are shown in left and right sides, respectively. Both methods show good performance gain compared to the performance without phase correction. For random phase selection algorithm, the performance difference with the different number of phase selection points and iteration is very small. In phase compensation method, we only include the phase estimation error due to the noise in this simulation, and it follows the perfect synchronization case well. The performance gap between two methods is due to the phase step size and limit of iteration of random phase selection method.

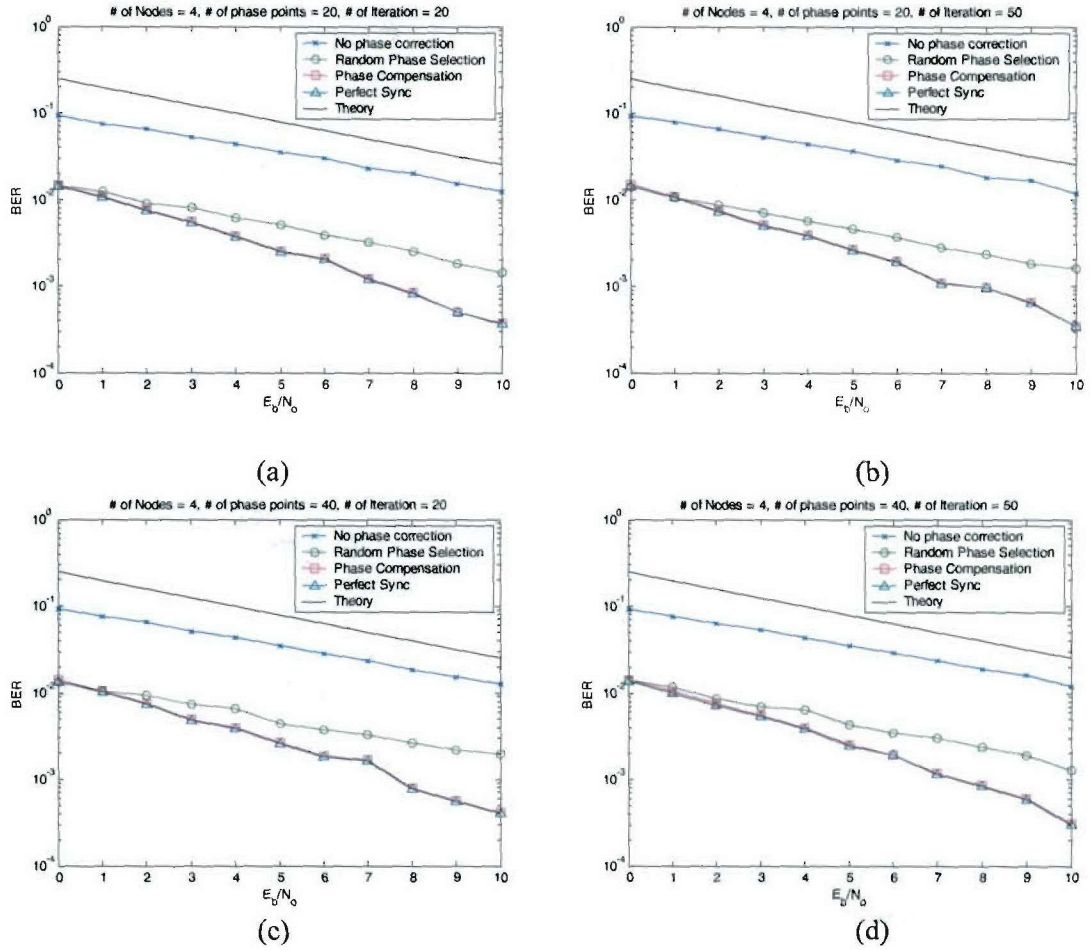


Figure 2.4-13 BER performance of a distributed beamforming with 4 nodes.

Random phase selection in fading channel

Random phase selection and channel compensation methods in distributed beamforming can achieve the gain based on the assumption that the channel does not change during the data transmission. This assumption is quite reasonable for the static indoor channel. However, if large size data transmits to the destination using the data fragmentation such as in IEEE 802.11 MAC, we cannot guarantee this assumption for the whole data transmission time. For this case, the random phase selection algorithm should be modified. If there is a short ACK message for each fragmented packet, feedback information for the current received power can be included in this packet. We want to use this feedback information to track the channel status by changing the phase within certain range. The details of this algorithm are as follows.

Transmit the signal with random phase (PO_i) at each transmitter
perform random phase selection method
set power difference dP
preset threshold power, $P_{th} = \text{average}(N \text{ previous received power})$
From next data, measure the received power P_{curr}
if $(P_{curr} - P_{th}) / P_{th} < dP$


```

        feedback with 0
    else if  $dP \leq (P_{curr} - P_{th}) / P_{th} < 2dP$ 
        feedback with 1
    else if  $2dP \leq (P_{curr} - P_{th}) / P_{th} < 3dP$ 
        feedback with 2
    else if  $3dP \leq (P_{curr} - P_{th}) / P_{th} < 4dP$ 
        feedback with 3
    else
        feedback with number of phase selection points

at the transmitter
    if feedback = 0
        keep current phase
    else if feedback = 1
        new phase = current phase + randsrc[-ph_step:ph_step]
    else if feedback = 2
        new phase = current phase + randsrc[-2×ph_step:2×ph_step]
    else if feedback = 3
        new phase = current phase + randsrc[-3×ph_step:3×ph_step]
    else
        choose new phase randomly

```

2.4.4 Productivity

Journal publications

1. J.Ibrahim and R.M. Buehrer, "Two-Stage Acquisition for UWB in Dense Multipath," accepted for publication in *IEEE Journal on Selected Areas in Communications*, March 2005.
2. J.Ibrahim, R. Menon and R.M. Buehrer, "UWB Waveform Optimization for Dense Multipath Channels," *submitted to IEEE Communication Letters*, August 2005.

Conference publications

1. S. Venkatesh and R.M. Buehrer, "MARCoPoLo: Medium Access Resource Control for UWB-based Position-Location Networks," submitted to ICC 2006.
2. J. Ibrahim and R.M. Buehrer, "A UWB Multiple Antenna System for NBI Mitigation under Rayleigh and Ricean Fading", submitted to ICC 2006.
3. J.Ibrahim, R. Menon, and R.M. Buehrer, "UWB Sequence Optimization for Enhanced Energy Capture and Interference Mitigation," *IEEE Military Communications Conference MILCOM2005*, Atlantic City, NJ, October 2005.
4. J. Ibrahim and R.M. Buehrer, "Two-Stage Acquisition for UWB in Dense Multipath," *IEEE Military Communications Conference MILCOM2005*, Atlantic City, NJ, October 2005.
5. S. Venkatesh, N. Kumar, and R.M. Buehrer, "A Spread-Spectrum MAC Protocol for Impulse-Radio Networks," *IEEE Vehicular Technology Conference*, September 2005.

Students supported

Qiao Chen, January. 1, 2005 – present
 Swaroop Venkatesh, January. 1, 2005 – present

Jihad Ibrahim, January. 1, 2005 – present

Faculty supported

R. Michael Buehrer, Jan. 1, 2005 – present

Scott Midkiff, Jan 1, 2005 – present

3. TASK 3 Visualization of Wireless Technology and Ad Hoc Networks

3.1 Overview

Task Objective: The objective of this task is to identify and investigate AWINN enabling technologies for the Close-in Sea Basing.

Organization: The task is directed by Ali Nayfeh and Rick Habayeb. The personnel list follows.

Rick Habayeb, faculty

Ali Nayfeh, faculty

Ehab Abdul Rahman, faculty

Summary: The main activity during this period was integrating the crane controller into a fielded crane. This will provide the bridge to transition the UWB ranging technology into the Sea Basing environment.

3.2 Task Activities for the period

During this quarter we had a golden opportunity to establish a potential transition path for the AWINN technologies into the Sea Basing environment. Last quarter, the team was given approval to piggy-back on a fielded crane at the seaport of Jeddah, Saudi Arabia. The crane controller developed at VT was integrated into a fielded crane at the seaport. Experiments to evaluate the crane controller are still ongoing.

For the VT anti-sway control system to work, the “sway angle” or the “pendulation angle” of the container must be accurately measured and fed back to the control algorithm. In a live, full-scale test of a quay-side container crane, a “contact” sway sensor must be rugged and able to withstand very large forces from multiple sources. A “contact” sway sensor measures the cable angle through a mechanical linkage attached to the crane hoist cables.

The forces on the sensor arise from the hoist cables. The cables are 30 mm thick greased and galvanized steel. The cables are braided, so whenever the crane moves a motion similar to that of a very high-speed screw is exerted on anything clamping the cables. Also, whenever the crane moves its base position perpendicular to the motion of the trolley (gantry) oscillations can be induced in that direction. Furthermore, due to day-to-day operations, other uncommon forces can be exerted on the system, such as if the operator lets the hoist cables slack and then begins to lift cargo, then the cables “snap” much like a whip.

Figure 3-1 shows the complete design of our sway sensor assembly. All of the materials used were either high strength stainless steel (316) or aircraft grade aluminum (7075-T6). The bottom assembly can be seen in Figures 3-2 and 3-3. The top assembly can be seen in Figure 3-4. The sensor has two degrees of freedom: in-plane with the trolley (and sway motion) of the cargo and out-of-plane with the trolley to compensate for the gantry motion. The hoist cable passes through two spring-loaded pulleys in the bottom assembly.

Figure 3-2 shows the configuration for the bottom assembly. There are two spring-loaded pulleys sandwiched between two aluminum plates, held together by stainless steel rods. The spring loaded pulleys will keep the sensor firmly attached to the hoist cable, and at the same time absorb most of the forces from the braided cable. The bronze rollers are present to prevent any snapping

force from the cables to strike the rest of the assembly and to make sure that the sensor alignment is correct in the horizontal axes.

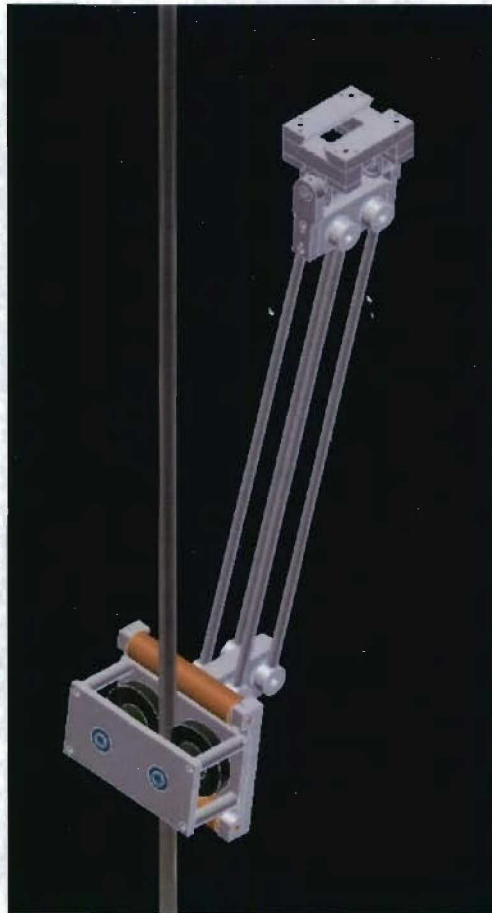


Figure 3-1 Complete sway sensor design.

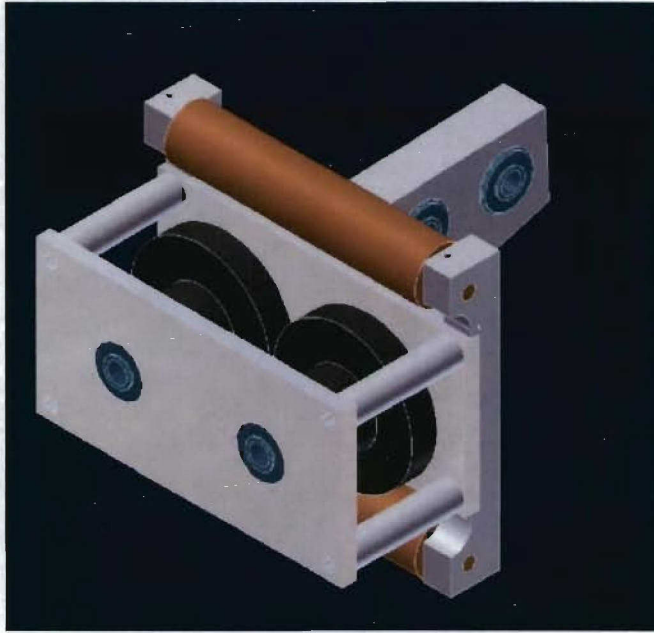


Figure 3-2 Isometric view of the bottom part of the sway sensor.

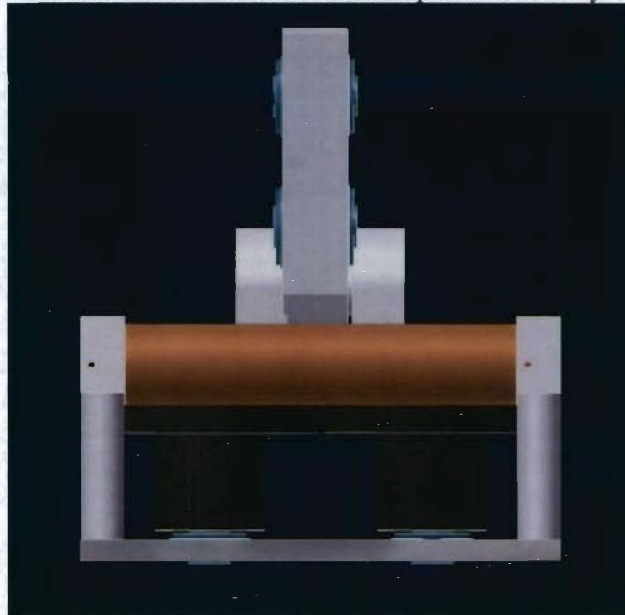


Figure 3-3 Top view of the bottom part of the sway sensor.

Figure 3-3 shows a top view of the bottom assembly. The plate behind the assembly attaches to a “four-bar” mechanism that connects to the top assembly. The four-bar mechanism is used to keep proper alignment of the sensor assembly and for strength.

Figure 3-4 shows the top assembly. An absolute encoder is mounted on the shaft to go between the “Y” shaped plate and arms on the bottom part. This is the direction of motion to be measured. This assembly is mounted directly to the crane structure by use of a “dovetail” mount. The materials in the dovetail are stainless steel. Aluminum is used on the lower “Y” shaped plate and arms to conserve weight.

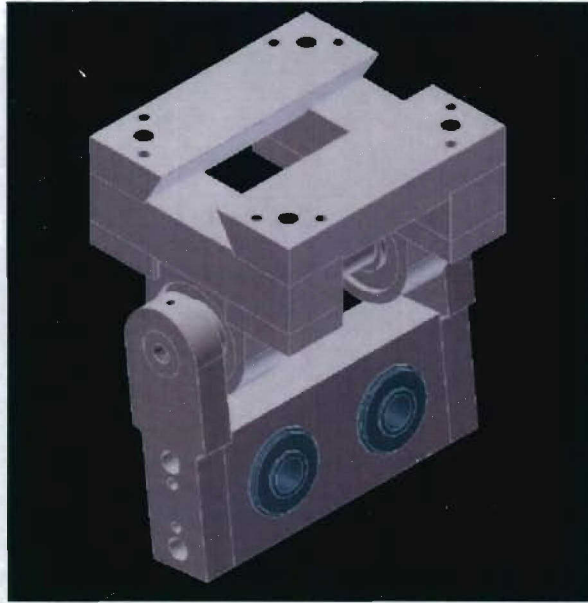


Figure 3-4 Isometric view of the top part of the sway sensor.

The team attempted to machine eight designs in Saudi Arabia, but all of them could not withstand the harsh environment. This is why we have switched to the very expensive materials of high strength stainless steel (316) and aircraft grade aluminum (7075-T6). Moreover, we could not get the precision machining in Saudi Arabia and hence machined all of the fixtures in the US.

The entire assembly for one sensor weighs approximately 85 lbs. Two are required for each crane. The team's experience clearly demonstrated the need for non-contact sensors, such as is possible with UWB position location.

3.3 Importance/Relevance

ForceNet is the Navy implementation plan for Network Centric transformation. There are three fundamental concepts in ForceNet: Sea Shield, Sea Strike, Sea Basing. Sea Basing is projecting joint operational independence. There are several technological challenges associated with the Navy vision for Sea Basing. The first major challenge is the Close-in command, control, and communication (C3). Currently, ship-to-ship Close-in C3 during UNREP is tedious, time consuming, archaic, and labor intensive. This project will explore, develop, visualize, and integrate the high payoff enabling AWINN technologies for the Close-in sea basing environment.

3.4 Productivity

1. A.H. Nayfeh, Z. N. Masoud, N. A. Nayfeh, and E. Abdel-Rahman, "Control of Ship-Mounted Cranes," Plenary Lecture, IUTAM Symposium on Vibration Control of Nonlinear Mechanisms and Structures, Munich, Germany, July 28-22, 2005.
2. A.H. Nayfeh, "Nonlinear Dynamics: Phenomena and Applications", Lyapunov Lecture, ASME 20th Biennial Conference on Mechanical Vibration and Noise, DETC2005-84144, Long Beach, CA, September 24-28, 2005.
3. N. A. Nayfeh, Z. N. Masoud, and W. T. Baumann, "A comparison of three feedback controllers for container cranes," Proceedings of the 5th ASME International Conference on Multibody Systems, Nonlinear Dynamics and Control, Long Beach, CA, Sept. 2005.

Students Supported

N. Nayfeh- January 25, 2005 to present
M.Daqaq – January 25, 2005 to present
O. Marzouk- January 25, 2005 to present

4. TASK 4 Testing and Demonstrations

4.1 TIP#1 Distributed MIMO UWB sensor networks incorporating software radio

Theoretical Analysis of Relay Based Communication System

In this section we evaluate the ABER (average bit error rate) performance of a two-hop multiple relay based communication system with different combinations SSTC, AF and DF. Figure 4.1-1 shows some of the scenarios that were analyzed for ABER performance. The corresponding results are plotted in Figure 4.1-2.

Four schemes were analyzed which are described below:

1. source-broadcast, MRC combining with DF at relays and MRC combining at destination
2. STBC encoding at source, AF at relays and STBC decode with MRC at destination
3. source-broadcast, MRC combining with SSTC based DF at relays, STBC decode at destination
4. source broadcast on multiple frequencies, AF at relays and MRC based combining at destination

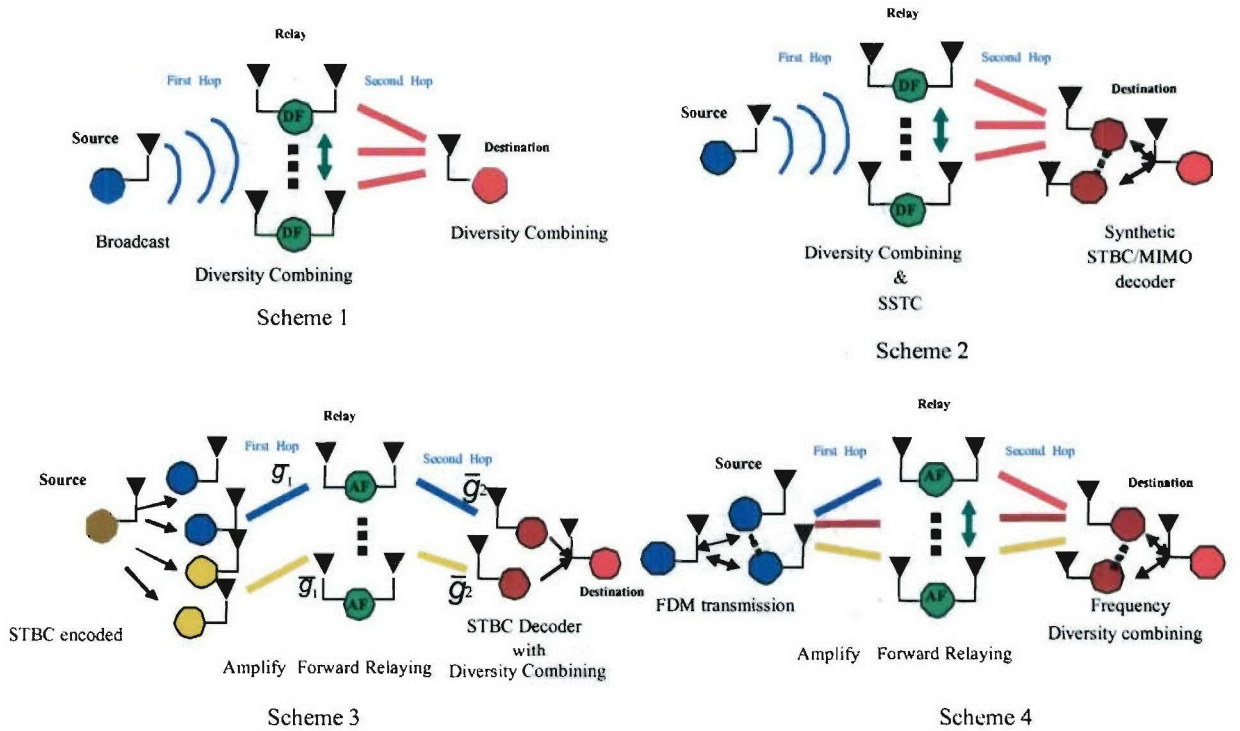


Figure 4.1-1 Simple scenarios for two-hop communication links using distributed MIMO techniques.

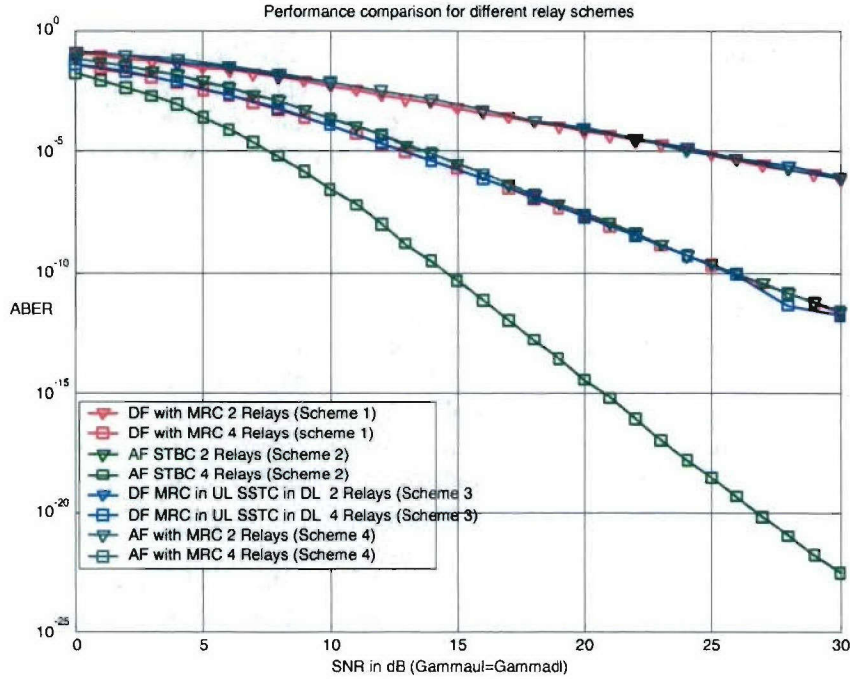


Figure 4.1-2 ABER performance of two-hop communication links.

As seen from Fig 4.1-2 all schemes have similar performance because they provide the same order of diversity. The second scheme with SSTC provides twice the diversity gain but requires more bandwidth. Hence, it should be noted that ABER performance for different schemes can be the same but the implementation complexity and bandwidth efficiency varies with the architecture selected. For example scheme 4 with AF is simple to implement but is bandwidth inefficient. Scheme 3 is bandwidth efficient but implementation complexity is high because cooperation is required.

Having looked at theoretical evaluation of performance, we next examine the effect of timing errors that can arise due to GPS clock inaccuracies and when local clocks are used during GPS outages.

Effect of Time synchronization Error on the Performance of SSTC

Communication using cooperation among distributed nodes was described in earlier sections. However, the performance studies assumed perfect time synchronization among cooperating transmit relay nodes. Use of GPS assisted oscillators at the transmitters can offer high degree of accuracy for coordinated transmission. However, operation under certain environments (for example, urban setting with tall buildings) can result in GPS outages. In such situations, Kalman filtering based approaches with augmentation of the clock can be used to minimize the drift in clock frequency.

In a distributed transmission, lack of accuracy between clocks among the transmitters can cause timing jitters. Failure to track that track and correct for drift of the transmitted signal can result in sampling offsets for signals transmitted from certain cooperating nodes. The combined effects of the former and latter in timing creates inter-symbol interference (ISI) when pulse shaping is applied, which can degrade the performance of a synthetic MIMO system.

Before we suggest algorithms/schemes suitable for synthetic MIMO, it is important to quantify the effect of time synchronization error in such a system. Therefore, we first analyze the SSTC based two hop relay system with time synchronization error. Then, based on the results observed we suggest algorithms and schemes that are well suited for combating errors in a cooperative set up.

SSTC System Model with ISI

In this section we show the analysis to derive the average bit error rate (ABER) of the SSTC system. To make the ABER analysis easier to understand we consider a 2x1 distributed MISO system although it is possible to extend the analysis to MIMO systems. The analysis presented considers the effect of both ISI from any number of adjacent symbols as well as cross-symbol interference from the symbols transmitted from cooperating nodes. The analysis provided can also handle the effects of non identical fading channels over different cooperative links, which is more probable in a distributed ad-hoc network setup.

It is assumed that the channels between the distributed transmitters and the receiver are independent and undergo slow frequency non-selective fading. For coherent STBC under perfect synchronization the received signal model after some manipulation can be written as

$$\begin{bmatrix} r_l \\ -r_{l+1}^* \end{bmatrix} = \begin{bmatrix} h_1 & h_2 \\ -h_2^* & h_1^* \end{bmatrix} \begin{bmatrix} s_{l,1} \\ s_{l,2} \end{bmatrix} + \begin{bmatrix} n_l \\ -n_{l+1}^* \end{bmatrix} \quad (4.1-1)$$

where r_l and r_{l+1} are received signals during l^{th} symbol duration and $l+1^{\text{th}}$ symbol duration respectively. $s_{l,1}$ and $s_{l,2}$ are the symbols transmitted by cooperating transmit nodes 1 and 2, respectively, corresponding to the space-time block code transmitted at l^{th} symbol duration. The channels are assumed to be quasi-static over the duration of the block code. Hence, h_1 and h_2 represent the random channel gains from transmit antenna 1 and 2, respectively. The channel gain can be expressed as

$$h_m = \alpha_m \exp(j\theta_m) \sqrt{P_m} \quad (4.1-2)$$

where α_m is a random amplitude process (fading), θ_m is the uniformly distributed random phase process and P_m is the transmitted power for the symbol received from m^{th} antenna. n_l and n_{l+1} are additive white Gaussian noise (AWGN) terms corresponding to the received symbol durations with zero mean and a two sided power spectral density equal to $N_0/2$. For a maximum likelihood detector the decision statistics under perfect synchronization at the output of the linear combiner is given by

$$\begin{bmatrix} \hat{X}_1 \\ \hat{X}_2 \end{bmatrix} = \Re\{\mathbf{H}^H \mathbf{r}\} = \Re\left\{ \begin{bmatrix} h_1^* & -h_2^* \\ h_2^* & h_1^* \end{bmatrix} \begin{bmatrix} r_l \\ -r_{l+1}^* \end{bmatrix} \right\} \quad (4.1-3)$$

where $\Re\{\cdot\}$ represents the real part.

Next, we introduce pulse shaping into the above analysis. The transmitted signal after pulse shaping can be expressed as

$$s(t) = \sum_{l=-\infty}^{\infty} b_l g(t-lT) \quad (4.1-4)$$

where b_l represents transmitted binary data sequence taking values $\{1, -1\}$ with equal probabilities. $g(t)$ is the impulse response at the output of the matched filter due to pulse shaping and T is the

symbol duration. In discrete form, (4.1-4) can be rewritten as $s = \sum_{l=-\infty}^{\infty} b_l g_l$.

The received signal block starting at k^{th} symbol time duration is now given by

$$\begin{bmatrix} r_k \\ r_{k+1} \end{bmatrix} = \begin{bmatrix} \sum_{m=1}^2 h_{k,m} b_{k,m} g_{k,m} + \sum_{m=1}^2 \sum_{\substack{l=-\infty \\ l \neq k}}^{\infty} h_{l,m} b_{l,m} g_{k-l,m} \\ \sum_{m=1}^2 h_{k,m} b_{k+1,m} g_{k+1,m} + \sum_{m=1}^2 \sum_{\substack{l=-\infty \\ l \neq k+1}}^{\infty} h_{l,m} b_{l,m} g_{k-l+1,m} \end{bmatrix} + \begin{bmatrix} n_k \\ n_{k+1} \end{bmatrix} \quad (4.1-5)$$

The subscripts k and l represent the symbol sampling time. m represents the transmit antenna from which the symbol was transmitted. Due to symmetry considerations of the BPSK system, it will suffice to calculate the probability of error of one of the decision statistics shown in 4.1-3. After some straight forward substitution of (4.1-5) in (4.1-3) the decision statistic at the output of the OSTBC linear combiner can be written as

$$\hat{X}_1 = \Re \left\{ \begin{aligned} & \left(|h_{k,1}|^2 g_{k,1} + |h_{k,2}|^2 g_{k+1,2} \right) b_{k,1} + \left(h_{k,1}^* h_{k,2} g_{k,2} - h_{k,2}^* h_{k,1} g_{k+1,1} \right) b_{k,2} \\ & + h_{k,1}^* \sum_{m=1}^2 \sum_{\substack{l=-\infty \\ l \neq k}}^{\infty} h_{l,m} b_{l,m} g_{k-l,m} + h_{k,2} \sum_{m=1}^2 \sum_{\substack{l=-\infty \\ l \neq k+1}}^{\infty} h_{l,m}^* b_{l,m} g_{k-l-1,m} \\ & + h_{k,2} n_k + h_{k,1}^* n_{k+1} \end{aligned} \right\} \quad (4.1-6)$$

Having described the system model, we now examine at modeling time synchronization error and deriving the ABER. Time synchronization error causes the pulses to overlap at the receiver. This effect can be characterized in the pulse shaped received symbol output as

$$s_{l,m}(t) = \sum_{l=-\infty}^{\infty} b_{l,m} g(t-lT-\tau_{l,m}) \quad (4.1-7)$$

where $\tau_{l,m}$ can be modeled as a random variable uniformly distributed on $U\left[\frac{-\Delta T}{2}, \frac{\Delta T}{2}\right]$ and

$0 \leq \Delta T < 0.5T$. Hence all $g_{l,m}$ in (4.1-6) are also random variables whose outcome depends on $\tau_{l,m}$.

Now assume that $b_{k,1} = -1$ was transmitted. Equation (4.1-6) can now be written as

$$\begin{aligned}
\hat{X}_1 = & -\left(|h_{k,1}|^2 g_{k,1} + |h_{k,2}|^2 g_{k+1,2}\right) \\
& + \Re\left\{\left(h_{k,1}^* h_{k,2} g_{k,2} - h_{k,2} h_{k,1}^* g_{k+1,1}\right) b_{k,2}\right\} \\
& + \Re\left\{h_{k,1}^* \sum_{m=1}^2 \sum_{\substack{l=-\infty \\ l \neq k}}^{\infty} h_{l,m} b_{l,m} g_{k-l,m}\right\} + \Re\left\{h_{k,2} \sum_{m=1}^2 \sum_{\substack{l=-\infty \\ l \neq k+1}}^{\infty} h_{l,m}^* b_{l,m} g_{k-l-1,m}^*\right\} \\
& + \Re\left\{h_{k,2} n_k + h_{k,1}^* n_{k+1}\right\} \\
= & -A + Z_1 + Z_2 + Z_3 + \eta
\end{aligned} \tag{4.1-8}$$

where η is a Gaussian random variable with zero mean and variance given by

$$\sigma_\eta^2 = \frac{\sum_{m=1}^2 |h_{k,m}|^2}{2} \tag{4.1-9}$$

Using (4.1-9), η can now be expressed as function of a zero mean unit variance Gaussian random variable n given by

$$\eta = \sigma_\eta n \tag{4.1-10}$$

The average probability of bit error conditioned on A, Z_1, Z_2 and Z_3 can be written as

$$\begin{aligned}
P_{e|A, Z_1, Z_2, Z_3} &= \Pr(-A + Z_1 + Z_2 + Z_3 + \eta > 0) \\
&= \Pr(\eta > A - Z_1 - Z_2 - Z_3) \\
&= \Pr(n\sigma_\eta > A - Z_1 - Z_2 - Z_3)
\end{aligned} \tag{4.1-11}$$

Here we make the following approximation with respect to the expression for A to make the ABER analytically tractable.

$$\begin{aligned}
A &= |h_{k,1}|^2 g_{k,1} + |h_{k,2}|^2 g_{k+1,2} \\
&\approx \sum_{m=1}^2 |h_{k,m}|^2
\end{aligned} \tag{4.1-12}$$

Although time synchronization error causes a fractional reduction in the sampled values of the pulseshapes $g_{k,1}$ and $g_{k+1,2}$ from their peak resulting in reduced SNR, its effect on ABER with fading is minimal when jitter is limited to $0 \leq \Delta T < 0.5T$ depending on the roll off factor of the pulse shape used.

Substituting (4.1-9) and (4.1-12) in (4.1-11), the conditional probability of error can now be written as

$$\begin{aligned}
P_{\sqrt{\sum_{m=1}^2 |h_{k,m}|^2}, Z_1, Z_2, Z_3} &= \Pr \left(n > \sqrt{2} \left(\sqrt{\sum_{m=1}^2 |h_{k,m}|^2} - \frac{(Z_1 + Z_2 + Z_3)}{\sqrt{\sum_{m=1}^2 |h_{k,m}|^2}} \right) \right) \\
&= Q \left(\sqrt{2} \left(\sqrt{\sum_{m=1}^2 |h_{k,m}|^2} - \frac{(Z_1 + Z_2 + Z_3)}{\sqrt{\sum_{m=1}^2 |h_{k,m}|^2}} \right) \right)
\end{aligned} \tag{4.1-13}$$

where $Q(x)$ is the tail probability of a zero-mean, unit variance Gaussian random variable (GRV) that exceeds x . By invoking Gil-Pelaez inversion theorem and using the CHF of GRV the expression for $Q(x)$ can be written as

$$Q(x) = \frac{1}{2} + \frac{1}{\pi} \int_0^{\infty} \frac{1}{t} e^{-t^2/2} \Im \{ e^{-j\mu t} \} dt \tag{4.1-14}$$

where $\Im \{ \cdot \}$ denotes the imaginary part. Now the average probability of error P_e is given by

$$P_e = \Pr(\hat{X}_1 > 0 | b_{k,1} = -1) \tag{4.1-15}$$

If we let $Z_0 = \sqrt{\sum_{m=1}^2 |h_{k,m}|^2}$, then P_e can now be expressed as

$$P_e = \int_{-\infty}^{\infty} \int_{-\infty}^{\infty} \int_{-\infty}^{\infty} \int_{-\infty}^{\infty} f_{Z_0} Q \left(\sqrt{2} \left(Z_0 - \frac{(Z_1 + Z_2 + Z_3)}{Z_0} \right) \right) dZ_3 dZ_2 dZ_1 dZ_0 \tag{4.1-16}$$

where f_{Z_0} , f_{Z_1} , f_{Z_2} and f_{Z_3} are the probability density functions (PDFs) of the random variables Z_0 , Z_1 , Z_2 and Z_3 . Substituting (4.1-11) in (4.1-13) gives

$$P_e = \frac{1}{2} + \frac{1}{\pi} \int_0^{\infty} \frac{1}{t} e^{-t^2/2} \Im \left(\int_{-\infty}^{\infty} \int_{-\infty}^{\infty} \int_{-\infty}^{\infty} \int_{-\infty}^{\infty} f_{Z_0} e^{-j\mu t Z_0} \phi_{Z_1} \left(\frac{\sqrt{2}}{Z_0} \right) \phi_{Z_2} \left(\frac{\sqrt{2}}{Z_0} \right) \phi_{Z_3} \left(\frac{\sqrt{2}}{Z_0} \right) dZ_3 dZ_2 dZ_1 dZ_0 \right) dt \tag{4.1-17}$$

where $\phi_{Z_i}(t)$ is the CHF of random variable Z_i . The integrals involved in (4.1-17) can be numerically evaluated using the Gauss-Chebyshev method.

Now we examine the evaluation of the PDF of Z_0 and the CHF's of Z_1 , Z_2 and Z_3 . The PDF of Z_0 can be calculated as

$$f_{Z_0}(z) = 2z f_{\sum_{m=1}^2 |h_{k,m}|^2} (z^2) \tag{4.1-18}$$

where $\gamma_m = |h_{k,m}|^2 = \frac{1}{M} \alpha_m^2 \frac{E_b}{N_0}$; $M = 2$. M is the total number of transmit antennas. The PDF $f_{\sum_{m=1}^2 \gamma_m}$ can be easily computed by applying Abate's method for numerical inversion of Laplace transform to the combined CHF of $\sum_{m=1}^2 \gamma_m$. The expression is given by

$$f_{\sum_{m=1}^2 \gamma_m}(z) = LT^{-1} \left\{ \prod_{m=1}^2 \phi_{\gamma_m}(s) \right\} \quad (4.1-19)$$

where LT^{-1} stands for Laplace inversion, $\phi_{\gamma_m}(s)$ corresponds to the CHF of the received SNR for symbol received from m^{th} antenna.

Now we derive the expression for CHF of Z_2 and then show the final expressions for CHFs of Z_3 and Z_1 that can be derived in a similar way. We make use of the following identity:

Let X and Y be independent real random variables with characteristic functions ϕ and ψ respectively. The product XY has a CHF given by

$$E\{e^{j\lambda XY}\} = E_Y\{\phi_X(tY)\} = E_X\{\psi_Y(tX)\} \quad (4.1-20)$$

From (4.1-8) and using (4.1-2) to simplify Z_2 ,

$$\begin{aligned} Z_2 &= \Re \left\{ h_{k,1}^* \sum_{m=1}^2 \sum_{\substack{l=-\infty \\ l \neq k}}^{\infty} h_{l,m} b_{l,m} g_{k-l,m} \right\} \\ &= \sqrt{P_{k,1}} \alpha_{k,1} \sum_{m=1}^2 \sum_{\substack{l=-\infty \\ l \neq k}}^{\infty} \sqrt{P_{l,m}} \alpha_{l,m} \cos(\theta_{l,m}) b_{l,m} g_{k-l,m} \end{aligned} \quad (4.1-21)$$

where $\theta_{l,m} = \theta_{l,m} - \theta_{k,1}$ is the received phase difference which is uniformly distributed between $[0, 2\pi]$. The random variables $\alpha_{k,1}$, $\alpha_{l,m}$, $\theta_{l,m}$, $b_{l,m}$ and $g_{k-l,m}$ are all real and independent. Hence, using (4.1-20) to evaluate the CHF of (4.1-21) gives

$$\phi_{Z_2}(t) = E_{\sqrt{P_{k,1}} \alpha_{k,1}} \left\{ \prod_{m=1}^2 \prod_{\substack{l=-\infty \\ l \neq k}}^{\infty} E_{b_{l,m}} \left\{ E_{\theta_{l,m}} \left\{ E_{\sqrt{P_{l,m}} \alpha_{l,m}} \left(b_{l,m} g_{k-l,m} \cos(\theta_{l,m}) \right) \right\} \right\} \right\} \right\} \quad (4.1-22)$$

Noting that $b_{l,m}$ takes values $(1, -1)$ (4.1-19) can be simplified to

$$\phi_{Z_2}(t) = \int_0^{\infty} f_{\alpha_{k,1}} \left(\prod_{m=1}^2 \prod_{\substack{l=-\infty \\ l \neq k}}^{\infty} \int_{-\pi/2}^{\pi/2} \left(0.5 \int_0^{2\pi} f_{\theta_{l,m}} \phi_{\alpha_{l,m}}(-t g_{k-l,m} \cos(\theta_{l,m})) d\theta_{l,m} \right) \right. \\ \left. + 0.5 \int_0^{2\pi} f_{\theta_{l,m}} \phi_{\alpha_{l,m}}(-t g_{k-l,m} \cos(\theta_{l,m})) d\theta_{l,m} \right) d\tau_{\theta_{l,m}} d\alpha_{k,1} \quad (4.1-23)$$

where $f_{\alpha_{i,j}}$ is the PDF of the fading amplitude process; $f_{\tau_{k,l,m}}$ and $f_{\theta_{i,m}}$ have a uniformly distributed PDF. $\phi_{\alpha_{i,j}}$ are CHF of fading. It is important to note that different distributions and unequal average received SNRs can also be applied in this analysis for MISO system.

Final expressions for CHF of Z_3 and Z_4 are given below and can be evaluated in a similar fashion:

$$\phi_{Z_3}(t) = \int_{\alpha_2}^{\infty} \left(\prod_{\substack{m=1 \\ l \neq k}}^{\infty} \int_{-\Delta T/2}^{\Delta T/2} f_{\tau_{k,l,m}} \left(0.5 \int_0^{2\pi} f_{\theta_{i,m}} \phi_{\alpha_{i,m}} (-t g_{k,l,m} \cos(\theta_{i,m})) d\theta_{i,m} \right) \right. \\ \left. + 0.5 \int_0^{2\pi} f_{\theta_{i,m}} \phi_{\alpha_{i,m}} (-t g_{k,l,m} \cos(\theta_{i,m})) d\theta_{i,m} \right) d\tau_{k,l,m} d\alpha_{k,1} \quad (4.1-24)$$

$$\phi_{Z_4}(t) = 0.5 \left(\int_{\alpha_2}^{\infty} \int_{-\Delta T/2}^{\Delta T/2} f_{\tau_{k+2}} \left(\int_0^{2\pi} f_{\theta_{k+1}} \phi_{\alpha_{k+1}} (t \cos(\theta_{k+2-1}) g_{k,2}) d\theta_{k+2-1} \right) d\alpha_{k,2} \right. \\ - \int_{\alpha_2}^{\infty} \int_{-\Delta T/2}^{\Delta T/2} f_{\tau_{k+3}} \left(\int_0^{2\pi} f_{\theta_{k+1}} \phi_{\alpha_{k+1}} (t \cos(\theta_{k+2-1}) g_{k+1,1}) d\theta_{k+2-1} \right) d\alpha_{k,2} \\ + \int_{\alpha_2}^{\infty} \int_{-\Delta T/2}^{\Delta T/2} f_{\tau_{k+2}} \left(\int_0^{2\pi} f_{\theta_{k+1}} \phi_{\alpha_{k+1}} (-t \cos(\theta_{k+2-1}) g_{k,2}) d\theta_{k+2-1} \right) d\alpha_{k,2} \\ \left. - \int_{\alpha_2}^{\infty} \int_{-\Delta T/2}^{\Delta T/2} f_{\tau_{k+3}} \left(\int_0^{2\pi} f_{\theta_{k+1}} \phi_{\alpha_{k+1}} (-t \cos(\theta_{k+2-1}) g_{k+1,1}) d\theta_{k+2-1} \right) d\alpha_{k,2} \right) \quad (4.1-25)$$

The effect of the CHF computed for Z_4 in (4.1-22) on the ABER is negligible and hence can be ignored for practical purposes.

The analysis for the probability of bit error for a 2x1 distributed OSTBC BPSK system can now be completed by substituting (4.1-18), (4.1-23), (4.1-24) and (4.1-25) into (4.1-17). In the next section, we show numerical results using the above analysis.

Numerical Results

Analysis as well as simulation was performed for a 2x1 distributed OSTBC system with both links under slow flat Rayleigh fading channel. Fig. 4.1-3 plots the results of ABER versus total average received SNR for increasing values of jitter that is uniformly distributed between $\left[-\frac{\Delta T}{2}, \frac{\Delta T}{2}\right]$. The average channel received SNR on each link is balanced; i.e., the total

received average SNR is equally distributed across both links. First, it can be observed that the analysis matches perfectly with simulation results, which validates our approach. Second, it can be observed that as the jitter increases the ABER degrades rapidly. The effect of ISI due to time synchronization error is evident at high SNRs (SNR > 8 dB) where the saturation of the BER curves is evident. However, it should be noted that for jitter corresponding to a maximum of

$\frac{\Delta T}{2} = 0.05T$, the performance with ISI present is acceptable even at high SNR. Fig 4.1-4 shows a similar plot when the two links are unbalanced; specifically, the average channel SNRs are

distributed as 0.75 and 0.25 times the total received SNR at the output of the OSTBC combiner. The trends are similar to these in Fig. 4.1-3 with simulation validating the analysis for unbalanced links. A comparison with BER curves in Fig. 4.1-3 shows that the performance in the case of unbalanced links is slightly worse (about 1 dB) than for the balanced case. This is expected because jitter in links with higher SNR causes more ISI.

Now we examine the effect of having independent but non identical (i.n.d) channels for the two transmit links of distributed OSTBC with unequal average channel SNRs. Fig. 4.1-5 shows the analysis results where the average channel SNR is 0.75 times the total received average SNR for the dominant channel which also has a Nakagami- m distribution with $m = 6$. The other link is Rayleigh distributed where the average channel SNR is 0.25 times the total average received SNR. The degradation in performance due to jitter degrades faster than the previous cases. The performance at higher SNRs is also worse than in Fig. 4.1-4 for the same amount of jitter. The dominant channel with higher m factor and higher average fading gain causes higher ISI.

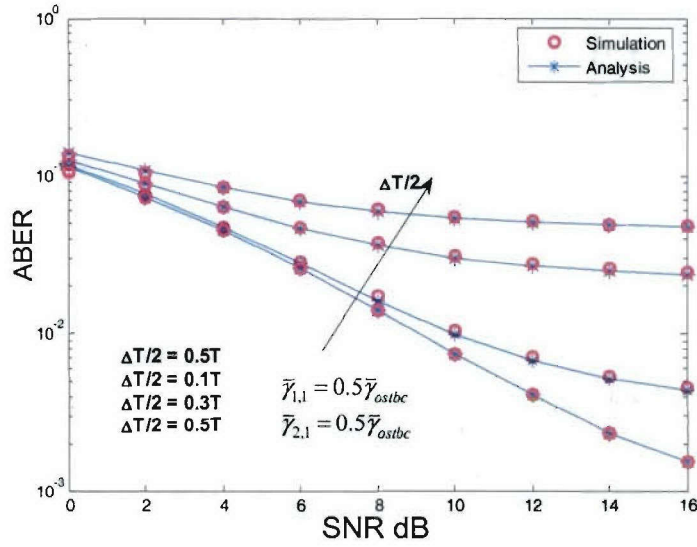


Figure 4.1-3 ABER for 2x1 distributed SSTC scheme for balanced Rayleigh fading channels.

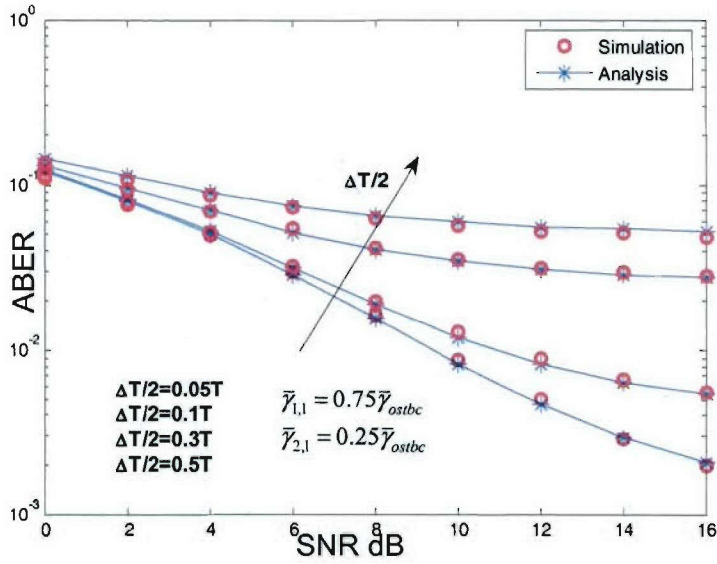


Figure 4.1-4 ABER for 2x1 distributed OSTBC scheme for unbalanced Rayleigh fading channels.

The choice of pulseshapes and their effect on ISI due to time synchronization error is now evaluated. Fig. 4.1-6 shows the plot generated for balanced Rayleigh fading channels using raised cosine pulseshape and better than raised cosine (BTRC) pulseshape. It is observed that for the same amount of jitter BTRC causes less ISI, resulting in better ABER performance.

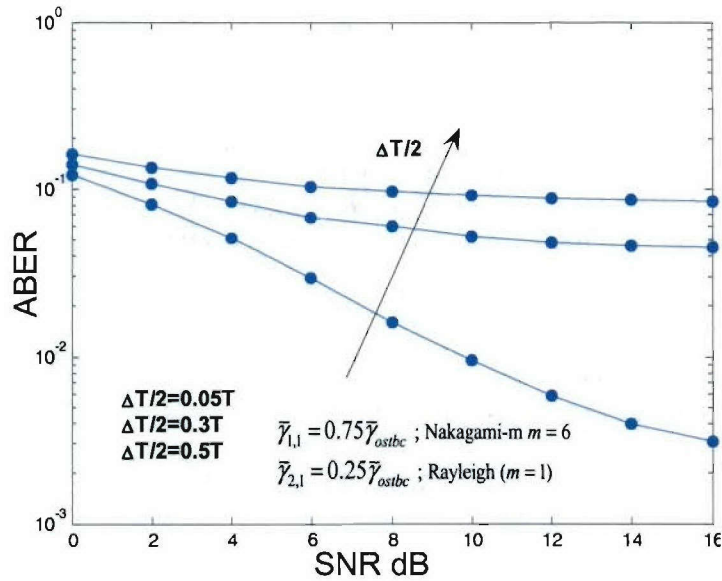


Figure 4.1-5 ABER for 2x1 distributed OSTBC scheme under unbalanced i.i.d fading channels.

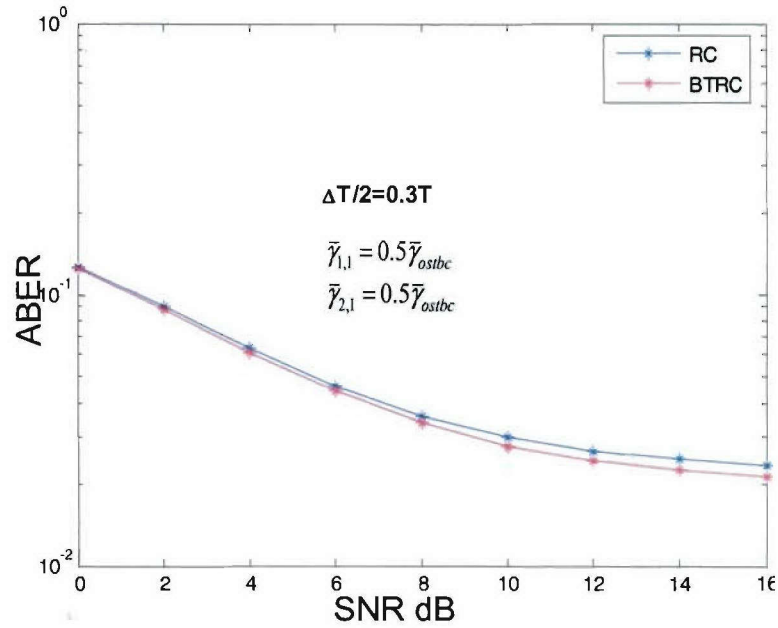


Figure 4.1-6 Comparison of ABER performance of distributed OSTBC with raised cosine and BTRC pulseshapes.

From the analysis and simulation results discussed above it is clear that for a acceptable performance the amount of timing error allowed is $\frac{\Delta T}{2} = 0.05T$. This means that given a symbol rate of 1 Mbps the maximum timing error allowed is about 100 ns. This is acceptable when GPS clocks with frequency accuracies of 10^{-12} are available. However under GPS outages where the clock frequency drift is considerable SSTC may not be suitable with simple phase shifted modulation schemes. Therefore, schemes that are robust against time synchronization errors are more applicable to synthetic MIMO. These schemes include space-time orthogonal frequency division multiplexing (ST-OFDM) and space-frequency orthogonal frequency division multiplexing (SF-OFDM). Hence future work on synthetic MIMO will require investigation of the above schemes for their robustness to timing errors in a distributed set up.

Schedule:

- January-Summer 2005
 - Develop UWB MIMO Algorithms
- Summer-Fall 2005
 - Simulate performance of UWB MIMO Algorithms
- Spring 2006
 - Begin Work on testing algorithms on Advanced SDR Receiver

Personnel:

Ramesh C. Palat

4.2 TIP#2 Close-in UWB wireless application to Sea Basing

Task objective: The objective of this subtask is to develop algorithms that allow UWB technology to provide precision position location, precision ranging, and imaging. With a low duty cycle and wide bandwidth, UWB is naturally suitable to radar and ranging applications. As the time duration of a pulse decreases, it provides finer resolution of reflected signals, such that the system can resolve distances with sub-centimeter accuracy using simple signal processing algorithms.

Accomplishments during reporting period: By the end of the last quarter the preparations for a crane ranging demonstration approached their final stage. All required components and equipment were determined, ordered, received and tested. The remaining tasks are to finish the assembly of some of the parts, configure the system, and optimize performance.

Demonstration Setup Specifications

Crane and Crate

The crane demo will use a scale model of the crane, crate and antenna system. The target scale crane is approximately 5 feet high and works with a crate of dimensions 4" wide x 10" long x 4.25" high as shown in Figure 4.2-1 below.

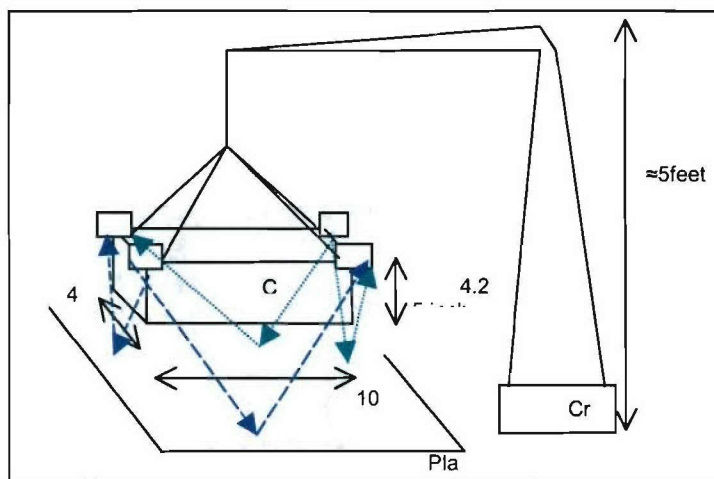


Figure 4.2-1 Demonstration hardware block diagram (not to scale).
pla: platform; cr: crane; c: crate.

Antenna Configuration on the Crate

The crate has four antenna pairs, one pair at each corner. Two pairs are designated transmitting pairs and the other two pairs are designated receiving pairs. The transmit and receive pairs are located on alternate corners as shown in Figure 4.2-1 and Figure 4.2-2. The signals from the receiving antennas on each corner are added via RF combiners and the signals to the transmitting corners antennas are distributed via RF dividers as shown in Figure 4.2-2.

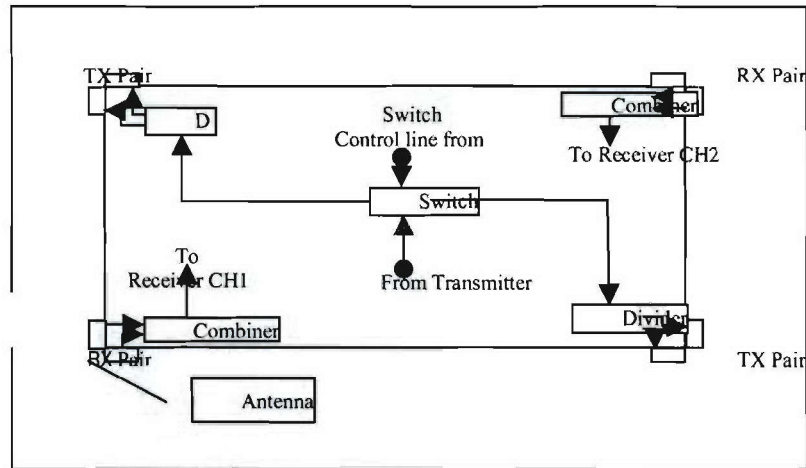


Figure 4.2-2 Antenna configuration on the crate.

Note that the transmitter is a Geozondas 30ps Pulser and the receiver is a Tektronix CSA8000B digital sampling oscilloscope. In order to facilitate communication between the antennas mounted on the crate, and the following transmitter/receiver cables are required:

- a) Three RF cables (1 TX, 2RX)
- b) One three-wire cable for controlling the switch

Because the system is implemented in a 1/24 scale, the electrical signals that make this possible have very high bandwidth requirements (approx. 5 to 20 GHz) and are very sensitive. For this reason, the RF cables must be as short as possible to limit signal loss. Note that in a full-scale implementation, this will not be the case since the frequencies will be much lower. In addition, the RF cables will consist of two sections as shown in Figure 4.2-3:

- a) A flexible section to minimize interference with the crate/crane movement (10ft).
- b) An inflexible section for the rest of the run. This is desired because it has better electrical properties (8ft).

The cable lengths were selected to be 10 ft and 8 ft for the flexible and inflexible sections, respectively. These lengths allow operation of the crane either with the flexible part alone, with some movement limitations, or with both cables for unconstrained motion. The flexible part only case is a backup option in case a satisfactory signal level cannot be achieved with both cables.

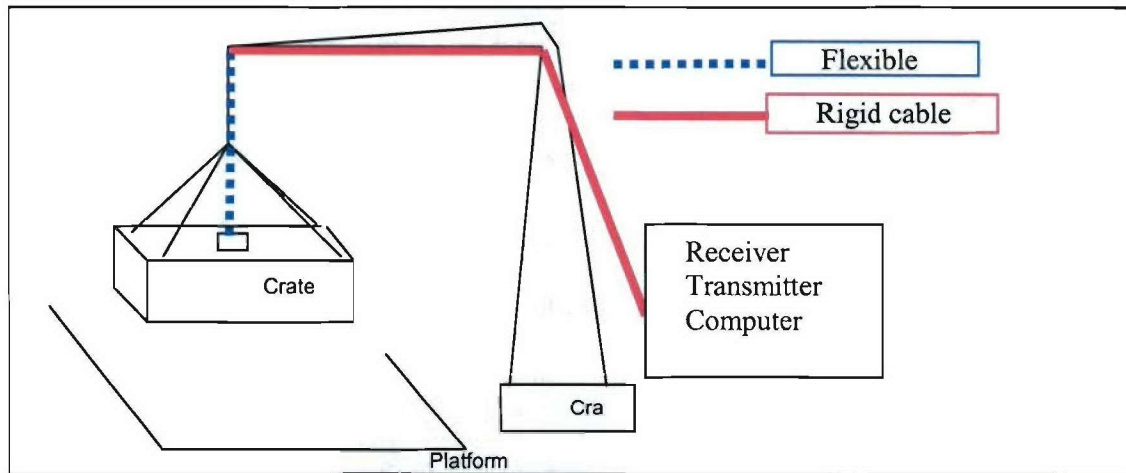


Figure 4.2-3 Cables arrangement.

Antenna Coupling

A potential antenna limitation arises from the fact that the antennas are close to each other and two types of coupling between the antennas are possible. The first is direct coupling between the transmitting and the receiving antennas. A coupled received signal is expected at the beginning of each receiving time window. This signal can be used for calibration of the receiving time window. However, if it is very strong and interferes with the received pulse, it must be mitigated. The easiest way to archive this is to record the coupling during calibration and subtract it from the received pulse. The second coupling expected is between the two nearby transmitting antennas that transmit the same pulse. This effect is expected to be minor because the antennas are separated with sheet metal (the crate) that should act as an isolator. To this point, antenna coupling has been found to have reasonable levels and to be successfully mitigated using signal processing.

Crate Weight

The crate weight should not exceed the weight (about 5 pounds) that the crane can support. The crate, antennas, the dividers/combiner, and the switches are made of light sheet metal and their total weight is not expected to exceed the weight handling of the crane. In the case that the crate is found to be too light, some weight might be added to make the crate movement more stable.

Measurement Procedure

The system design requires ranging from each of the four sides of the crate. For this reason each side has a pair of receiving and transmitting antennas. However, because it is not affordable to have four receivers and four transmitters we perform some multiplexing. First, since we have a receiver with dual channel receive capability, the receive antennas on each corner are grouped together. Second, because we only had one suitable pulser (transmitter) the transmission is alternated between the two transmitting corners (refer to Figure 4.2-1 and Figure 4.2-2). The measurement procedure is as follows:

1. Transmit from corner B; the two adjacent corners (A and D) each receive a pulse.
2. The range for those two sides is calculated.
3. Transmit from the opposite corner (corner C); the two adjacent corners (A and D) each receive a pulse.

4. The range for those two sides is calculated.
5. The crate orientation is estimated.
6. Return to step 1

Another option is to perform step 5 after step 2 (as well as after step 4) to increase the update rate of the system.

Operating Range and Update Rate

The system for this demonstration is planned to be implemented using a 10 ns receiving time window which will allow the system to range up to 5 ft. Actually, the crane control system only needs the exact range when the crate is approaching the ground (about 2 ft). Again, a full-scale system would be capable of ranging at significantly longer distances.

Another consideration is the update rate of the system. The speed of the system is limited by the electro-mechanical switch that is used to switch the transmitting antennas. The switch that was ordered can switch up to 50 times per second which means the system can give a full update 25 times per second. However, it must be noted that the electromechanical switch is guaranteed to work for 1 million cycles; therefore, this switch is only good for the purpose of the demonstration. It also must be noted that the target update rate is 20 updates per second, with a 10 update/second minimum. Current information indicates that 10 updates per second will be adequate for the crane control system, however, the highest possible rate is desired. Furthermore, another important limitation to the update rate is the Digital Signal Oscilloscope's ability to acquire and deliver different waveforms in that high rate. The Digital Signal Oscilloscope is able to deliver a high number of updates of the same waveform as it changes; however, when it is forced to clear all data acquired to acquire a completely new waveform its rate drops significantly. Various methods to optimize its performance are investigated.

Project Status

All the required parts and equipment required were received. Furthermore, all the components are expected to be shortly fully assembled and the main remaining tasks until the demonstration is to optimize the ranging software for best performance and to establish communication with the crane's control system, this also includes some intermediate demos as described in the task schedule.

Schedule:

- January-Summer 2005
 - Begin algorithm development
 - Test algorithms using the simple setups discussed above
- Summer-Fall 2005
 - Integrate ranging system into the crane hardware
 - Evaluate performance of position location algorithms in real-world environments
- January-Summer 2006
 - Finalize 3-D Ranging solution
 - Demonstrate passive and active position location system in laboratory environment.

Personnel:

Haris Volos – Ranging Algorithm Development and implementation

4.3 TIP #3: Secure Ad Hoc Networks

4.3.1 Project Description

The testing and demonstration of secure ad hoc networks involves integration and testing along three related tracks. These tasks, detailed below, will lead to a separate demonstration (or coupled set of demonstrations) using a common hardware and software base, as implemented in our test bed network (see discussion of Task 2.1).

- (a) Activities within Task 2.1 (Ad Hoc Networks) that support core network services will be integrated, tested, and demonstrated. Capabilities to be integrated include policy-based quality of service (QoS), security based on distributed certificate authorities (DCAs) for key management and trust grading, and mobile ad hoc network (MANET) routing support for QoS and security functionality and as a means to demonstrate cross-layer design. Cross-layer design techniques from Task 2.4 will be reviewed and incorporated as appropriate. Capabilities will be shown operating with Internet Protocol version 4 (IPv4) and, where feasible within the level of effort possible, Internet Protocol version 6 (IPv6).
- (b) A cross-layer approach to transporting multiple description (MD) video in ad hoc networks, also a part of Tasks 2.1, will be integrated, tested, and demonstrated. This task will utilize application-level routing to use application-specific optimal routes. It will integrate with the MANET routing effort of Task 2.1, e.g., with Open Shortest Path First-Multiple Connected Dominating Sets (OSPF-MCDS), to utilize the topology information efficiently obtained by the MANET routing protocol.
- (c) We will integrate real-time middleware from Task 2.2 with the combined QoS, security, and routing as discussed above and as investigated in Task 2.3. Specifically, we will investigate and develop methods and mechanisms to integrate policy-based quality of service (QoS) capabilities at the network level, and perhaps at the link layer, with real-time services offered by middleware.

4.3.2 Demonstration Description

Table 4.3-1 lists the themes, components, and leaders for the three demonstrations. Demonstration (a) focuses on core network services. Demonstration (b) involves network support for a video application. Demonstration (c) relates directly to Task 2.3 and involves the integration of network services with an application based on the time-utility function real-time middleware. We will adjust plans based on results from related tasks.

The components of the different demonstrations listed in Table 4.3-1 are currently envisioned to be the same except for the application – or application plus middleware in the case of Demonstration (b) – being supported. The security, QoS, and routing components are discussed further in this report in association with Task 2.1. Note that OSPF-MCDS-MC or, more simply, OMM, is a multi-channel version of the Open Shortest Path First with Minimum Connected Dominating Sets (OSPF-MCDS) MANET routing protocol. OLSR-MC is a multi-channel version of the Optimized Link State Routing (OLSR) MANET routing protocol. The topology viewer (TopoView) and topology emulation tools are carried over from the previous NAVCIITI project but will need to be modified to support new functions in the network and to work in an IPv6 environment. It is envisioned that additional performance monitoring and configuration control tools will be developed as part of Subtask 2.1(e) and used in the demonstrations.

Table 4.3-1 Demonstration Components and Leaders for the Three Demonstrations

Demonstration	Key Components	Leaders
a) Core network services	<ul style="list-style-type: none"> • Security and key management system • Policy-based quality of service • OSPF-MCDS-MC and/or OLSR-MC routing • TopoView network monitoring • Performance monitoring tools • Topology emulation 	<ul style="list-style-type: none"> • Scott Midkiff • Luiz DaSilva
b) Cross-layer approach to MD video routing	<ul style="list-style-type: none"> • OSPF-MCDS and/or OLSR routing • TopoView network monitoring • Performance monitoring tools • Topology emulation 	<ul style="list-style-type: none"> • Tom Hou • Scott Midkiff
c) Real-time middleware in an ad hoc network	<ul style="list-style-type: none"> • Real-time middleware • Security and key management system • Policy-based quality of service • OSPF-MCDS-MC and/or OLSR-MC routing • TopoView network monitoring • Performance monitoring tools • Topology emulation 	<ul style="list-style-type: none"> • Scott Midkiff • Luiz DaSilva • Binoy Ravindran

4.3.3 Cooperative AWINN Elements

This test and demonstration requires the inputs from AWINN tasks as specified in Table 4.3-2.

Table 4.3-2 Inputs from Cooperative AWINN Elements

Task (Subtask)	Inputs
2.1(a)	Prototype implementation of a policy-based QoS scheme
2.1(b)	Prototype implementation of MANET security and key management scheme
2.1(c)	Optimized prototype implementation of a MANET routing, specifically OSPF-MCDS-MC and/or OLSR-MC
2.1(f)	Performance monitoring tools; enhanced TopoView; enhanced topology emulation
2.1(d)	Video sensor application and test bed components
2.2	Real-time middleware
2.4	Cross-layer optimization elements that can be integrated into the test bed for testing and demonstration purposes.

4.3.4 Cooperative Non-AWINN Elements

At this time, no non-AWINN components are required (except for tools and equipment carried over from the NAVCIITI project).

4.3.5 Schedule of Activities

A general schedule listing major milestones is provided in Table 4.3-3. Note that the schedule is divided into four phases. During Phase I, the emphasis is on core network services of Demonstration (a) running with IPv4 and, as much as possible, with IPv6. During Phase II, the emphasis is on core network services of Demonstration (a) running with both IPv4 and IPv6. During Phase III, the emphasis is on integration of the MD video and real-time applications of Demonstrations (b) and (c), respectively. In Phase IV, the emphasis is on final demonstration of the MD video and real-time applications of Demonstrations (b) and (c), respectively.

Table 4.3-3 Schedule of Activities

<i>Activity</i>	<i>Date</i>
Phase I: Demonstrate core services using IPv4	4Q2005
Phase II: Demonstrate core services using IPv6	4Q2005
Phase III (b): Initial MD video integration	1Q2006
Phase III (c): Initial real-time middleware integration	1Q2006
Phase IV (b): Final demonstration of MD video	2Q2006
Phase IV (c): Final demonstration of real-time middleware	2Q2006

4.4 TIP #4: Integration of Close-in UWB wireless with ESM crane for Sea Basing applications

Task Objective: The goal of this task is to demonstrate the usefulness of UWB in close-in communications, ship-to-ship cargo transfer for sea-basing operations, and cargo transfer from ship-to-shore and vice versa.

Organization: This task is managed by Dr. A. H. Nayfeh

Dr. A.H. Nayfeh, Faculty

Dr. E. Abdel-Rahman, Post Doc

N.A.Nayfeh, GRA

Accomplishment during Reporting Period: The team of Task 4.2/ TIP #2 is progressing nicely in developing algorithms that allow the UWB technology to provide precision position location, ranging and imaging. These algorithms will be applicable to TIP #4. The team of TIP#4 is waiting to receive the UWB set-up and install it in the laboratory cranes. The UWB team is concentrating their effort on the interface with the boom crane. We had several coordination meetings to discuss the technical issues of how to interface the UWB hardware and software with the crane's controller. An ongoing investigation is the tradeoff between range, data rate, and power. There are two types of cranes in the ESM laboratories. Our technology transition opportunity is dependent on the available fielded crane. We have made great strides with the container crane. Therefore, our priority is to concentrate on the demonstration of UWB with the container crane.

We worked with the TIP#2 team to determine the range and update rates to be provided by the UWB system for the soft-landing experiment. However, according to the TIP#2 team, due to hardware issues, some range distance has to be sacrificed to achieve the required update rate. Measurements taken by the UWB system will be transferred to the soft-landing system via 8-bit parallel digital I/Os. The UWB will periodically update the outputs and the soft-landing system will acquire system data when it needs it.

First tests of the system will be run in a single-degree-of-freedom experiment with a large amplitude shaker as the target in Burrus 115. This will be done to ensure that both of the UWB sensor and the soft-landing programs and hardware can communicate in a low-risk environment. If the system performs satisfactorily, then it will be migrated over to the 1/24th scale crane in Hancock 105.

Our technology transition opportunity depends on the available fielded crane. We have made great strides with the container crane at the Jeddah Port, Saudi Arabia. And we also have a golden opportunity to demonstrate the VT controller at a full-scale crane at the Aqaba Port, Jordan. Therefore, our priority is to concentrate on the demonstration of the UWB system with the container crane because once the UWB setup for container cranes is ready, we will field it either in Jeddah or Aqaba.

Importance/Relevance

The proposed work has the potential of being very useful to the Navy's Transformational Sea-Basing System. The success of Sea Basing depends on the ability to sustain logistic operations while significantly reducing reliance on land bases. This requires the development of a high capacity, high reliability at-sea capability to transfer fuel, cargo, vehicle, and personnel in rough seas while underway from commercial container ships to large sea basing ships and then to

smaller ships. The wave-induced motion of the crane ship can produce large pendulations of the cargo being hoisted and cause the operations to be suspended

Personnel:

N.Nayfeh, January, 2005-present

5. FINANCIAL REPORT

